EQUATION OF STATE AND ELECTRICAL CONDUCTIVITY OF MATERIALS

By

Vinayak Mishra

Enrolment No: PHYS01200804012

BHABHA ATOMIC RESEARCH CENTRE (BARC)

A thesis submitted to the
Board of Studies in Physical Sciences

In partial fulfillment of requirements
For the Degree of

DOCTOR OF PHILOSOPHY

of

HOMI BHABHA NATIONAL INSTITUTE

August 2014

Homi Bhabha National Institute

Recommendations of the Viva Voce Board

As members of the Viva Voce Board, we certify that we have read the dissertation prepared by **Vinayak Mishra** entitled "Equation of state and electrical conductivity of materials" and recommend that it may be accepted as fulfilling the dissertation requirement for the Degree of Doctor of Philosophy.

-- Date :

Chairman : Prof. S. V. G. Menon

S. Chaturvedi ---------------------------------- Date : 10/7/14

Convener : Prof. Shashank Chaturvedi

Surendra M Sharma ------------------------------ Date :

Member : Prof. S. M. Sharma

-- Date : 10/7/2014

Member : Prof. L. J. Dhareshwar

-- Date : 10/7/2014

External Examiner : Prof. D. G. Kanhere

Final approval and acceptance of this dissertation is contingent upon the candidate's submission of the final copies of the dissertation to HBNI.

I hereby certify that I have read this dissertation prepared under my direction and recommend that it may be accepted as fulfilling the dissertation requirement.

Date: 10/7/14

Place: MUMBAI

Guide: S. Chaturvedi

(Dr. Shashank Chaturvedi)

STATEMENT BY AUTHOR

This dissertation has been submitted in partial fulfillment of requirements for an advanced degree at Homi Bhabha National Institute (HBNI) and is deposited in the Library to be made available to borrowers under rules of the HBNI.

Brief quotations from this dissertation are allowable without special permission, provided that accurate acknowledgement of source is made. Requests for permission for extended quotation from or reproduction of this manuscript in whole or in part may be granted by the Competent Authority of HBNI when in his or her judgment the proposed use of the material is in the interests of scholarship. In all other instances, however, permission must be obtained from the author.

Vinayak Mishra

04/08/2014

Vinayak Mishra

DECLARATION

I, hereby declare that the investigation presented in the thesis has been carried out by me. The work is original and the work has not been submitted earlier as a whole or in part for a degree/diploma at this or any other Institution or University.

04/08/2014
Vinayak Mishra

CERTIFICATION FROM GUIDE

This is to certify that the corrections suggested by the examiners of the thesis have been incorporated in the thesis submitted to HBNI.

Date 4/8/14

Guide......................
(Dr. Shashank Chaturvedi)

List of Publications arising from the thesis

Journals

1. **FP-LAPW Calculations of Equation of State and Elastic Properties of α and β phases of Tungsten Carbide at High Pressures**,
   Vinayak Mishra and Shashank Chaturvedi, *Journal of Physics and Chemistry of Solids* **74** (2013) 509.

2. **Equation of State of Al for Compressed and Expanded States from First-Principles Calculations**,
   Vinayak Mishra and Shashank Chaturvedi, *Physica B: Condensed Matter* **407** (2012) 2533.

3. **A Comparison of Quotidian EOS of Al with Ab Initio Calculations**,
   V. Mishra, Sijoy C.D., P. Pahari and S. Chaturvedi, *Journal of Physics: Conference Series* **377** (2012) 012105 (1-5)

4. **EOS and Conductivity of Expanded States of Aluminium**,
   V. Mishra V. Mehra and S. Chaturvedi, *Journal of Physics: Conference Series*, **377** (2012) 012103 (1-5).

5. **Generation of Electrical Conductivity Data of Al using ab-initio Molecular Dynamics simulations**,
   Vinayak Mishra and S. Chaturvedi *AIP Conf. Proc.*, **1349** (2011) 799.

6. **FCC- HCP Phase Coexistence in Al at High Pressure: Explanation in Terms of Density of States**,
   Vinayak Mishra and Shashank Chaturvedi *Physica B: Condensed Matter*, **403** (2008) 2676.

7. **Theoretical Study of FCC-HCP Phase Coexistence and Phase Stability in Al by FP-LAPW Method with GGA for Exchange and Correlation**,
   Vinayak Mishra and S. Chaturvedi *Physica B: Condensed Matter*, **393** (2007) 278.

   Note: In the following papers [8-10], the EOS data generated in this study, have been used for hydrodynamic simulation. These papers are not the part of this thesis.

8. **Comparisons between Fast Shock Tube Simulations and Tests**, V. Mehra, V. Mishra, C. D. Sijoy and S. Chaturvedi, Journal of Physics: Conf. Ser., **377** (2012) 012101 (1-4).

9. **Tensile instability and artificial stresses in impact problems in SPH**, V. Mehra, C. D. Sijoy V. Mishra and S. Chaturvedi, Journal of Physics: Conf. Ser, **377** (2012) 012102 (1-4).

10. **Burn Phase Calculations and One-Dimensional Optimization Studies for an Inverse Z-pinch Magnetized Target Fusion System** P. V. Subhash, S. Madhavan, N. Sakthivel, V. Mishra, P. Pahari, A. Majalee and S. Chaturvedi, *Plasma Physics and Controlled Fusion* **53** (2011) 085013.

Conference Presentations

1. **First Principles Investigation Of Structural Transformation In Tungsten Carbide**, Vinayak Mishra and Shashank Chaturvedi, presented at *National Conference on Advances in Materials Science and Technologies (AMST - 2012)*, Kakatiya University Warangal, A. P.

2. **First Principles Determination of Al EOS and its Application to 2-D MHD Simulation of Metallic Liner Implosion**, Vinayak Mishra, S. Madhavan, P. Pahari and S. Chaturvedi,presented in *International Conference on High Pressure Science and Technology*, AIRAPT-23, BARC, Mumbai, 25-30 Sept, 2011.

3. **A Comparison of Quotidian EOS of Al with Ab Initio Calculations**, V. Mishra, Sijoy C.D., P. Pahari and S. Chaturvedi, presented in *International Conference on High Pressure Science and Technology*, AIRAPT-23, BARC, Mumbai, 25-30 Sept, 2011.

4. **EOS and Conductivity of Expanded States of Aluminium**, V. Mishra V. Mehra and S. Chaturvedi, presented in *International Conference on High Pressure Science and Technology*, AIRAPT-23, BARC, Mumbai, 25-30 Sept, 2011.

5. **Equation of State of Aluminium in Expanded States**, V. Mishra and S. Chaturvedi, presented and published in the Proc. *54th DAE Solid State Physics Symposium, M. S. University of Baroda, 14-18 Dec. 2009*

6. **Elastic Properties and Equation of State of bcc Bismuth at High Compressions**
   Vinayak Mishra and S. Chaturvedi, presented and published in Proc. *52nd DAE Solid State Physics Symposium*, University of Mysore, 27-31 Dec. 2007.

   Note: In the following papers [7-9], the EOS data generated in this study, have been used for hydrodynamic simulation. These papers are not the part of this thesis.

7. **Computer Modelling of Electric Gun**
   Aaditya V. Majalee, V. R. Ikkurthi, P. Pahari, V. Mishra, S. Chaturvedi, presented in *International Conference on High Pressure Science and Technology, AIRAPT-23*, BARC, Mumbai, 25-30 Sept, 2011.

8. **Exploding foil simulations based on Equation of State data from ab-initio Molecular Dynamics**, A. V. Majalee, V. Mishra, P. Pahari, V. R. Ikkurthi and S. Chatturvedi, presented and published in the Proc. of *Indo - Russian Workshop on High Energy density Physics for Innovative Technologies & Industry Applications*, I2IT Pune , 19-21 Nov 2008.

9. **Production of Megabar Pressure in Metallic Liner: A Computational Study**
   S. Madhavan, V. Mishra, A. Majalee, P. Pahari and S. Chaturvedi, presented and published in the Proc. *52nd DAE Solid State Physics Symposium*, University of Mysore, 27-31 Dec. 2007.

Dedicated to my parents

ACKNOWLEDGEMENTS

It would not have been possible to write this doctoral thesis without the help, support and encouragement of the kind people around me, to only some of whom it is possible to give particular mention here.

My first debt of gratitude must go to my supervisor, Dr. Shashank Chaturvedi. He patiently provided the vision, encouragement and advise necessary for me to proceed through the doctoral program and complete my dissertation. He has been a strong and supportive adviser to me from the beginning of my career.

Special thanks to my committee, Dr. S. V. G. Menon, Dr. S. M. Sharma, and Dr. L. J. Dhareshwar for their support, guidance and helpful suggestions. Their guidance has served me well and I owe them my heartfelt appreciation.

This research work could not have been possible without the super computing facility of CAD, BARC - Vizag. I must thank Dr Shashank Chaturvedi for establishing this facility. Shri N Sakthivel also deserve my sincerest thanks, his help has meant more to me than I could ever express.

I thank my colleagues Dr Vishal Mehra, Sijoy C. D., Gursharn Singh, A. Majalee, Dr Manoj Warrier, Dr V. R. Ikkurthi, S. Madhavan, P. Pahari and Sunil Rawat for the stimulating discussions related to this research work.

Finally I want to thank my family. I owe a lot to my parents, Shri Satya Deo Mishra and Smt. Madhavi Mishra, who encouraged and helped me at every stage of my personal and academic life. Their love provided my inspiration and was my driving force. A special thought is devoted to my wife Richa Mishra for her personal support and great patience at all times. My always positive and joyful daughters Soma and Vani are powerful sources of inspiration and energy. I wish

to thank my brother Vishwambhar Mishra and sisters Sudha Dubey and Medha Tiwari, they have given me their never-ending support throughout, as always, for which my mere expression of thanks likewise does not suffice.

Vinayak Mishra

04/08/2014

SYNOPSIS

Introduction

Equation of State

The equation-of-state (EOS) of a material represents the pressure P and internal energy E as functions of density and temperature of the material [1,2,3,4,5]. P and E can be expressed as the superposition of three terms, viz., (1) The Cold Curve, which refers to Pressure and energy at zero kelvin, (2) "Ion thermal" contribution, representing the contribution from thermal motion of ions, and (3) "Electron thermal" contribution, which is the contribution due to finite electron temperature.

The EOS is an essential input to hydrodynamic simulations of Magnetized Target Fusion systems and pulse power experiments [6,7,8,9]. Two examples will illustrate this point:

1. **Compressed states:**

   Liner acceleration experiments can give rise to large compressions and pressures of upto 50 million atmospheres (megabars). Hence there is a need for EOS calculations upto 100 Megabar and densities upto 6 times normal density.

2. **Rarefied states:**

   In exploding wire and laser irradiation experiments, temperatures of metals such as aluminium can reach upto a few tens of thousands of Kelvin (few eV), while densities can fall to as low as $1/10^{th}$ or $1/100^{th}$ of normal density. This combination lies in the 'dense plasma' state. If the plasma is produced by electrically-driven explosion, modelling requires the EOS as an input. Hence there is a need to generate EOS data over these low density states and temperatures upto 50,000 deg-K.

The EOS and conductivity models used must generate not only accurate but also ‘smooth" data. A large body of literature exists on the calculations of Equations of State. However, these EOS models are applicable in specific density-temperature regimes and their accuracy decreases in other regimes [2-5]. Hydrodynamic simulations for different problems require different kinds of EOS data. For example, simulations for Inertial Fusion Energy (IFE) and pulsed-power systems require wide-ranging data covering orders of magnitude in density and temperature. Simulations for exploding wires require data in rarefied states of metals, but the temperature range only extends upto 5 eV (50,000 K). Simulations for high-velocity impact require data upto only 5-10% compression, but with high accuracy, and must take account of solid-solid phase transformations.

This thesis studies the EOS and conductivity of certain materials over the range of parameters described above. This has, necessarily, involved the development/use of computer codes in a variety of areas.

Electrical conductivity

Electrical conductivity is a property of a material which quantifies how well the material allows flow of an electric current. Fast opening switches based on electrically-exploded metal foils are of interest for pulsed power systems. Such explosions involve states with densities ranging from normal density ρ_0 down to $0.01\rho_0$ and temperatures ranging from room temperature up to a few electron volts. Modelling of electrically exploded fast opening switches requires the electrical conductivity data of the metal in this density-temperature regime, as an input. Hence there is a need to perform first principles study of conductivity of metals over these low density states and temperatures upto 50,000 deg-K.

Scope of the present work

In order to focus the present study, we have performed EOS studies for two materials. The first is the metallic element Aluminium (Al) and the second is a ceramic compound tungsten carbide (WC). Aluminium is of importance for liner acceleration and exploding foil systems. Even though there have been several studies of the EOS of Al, these EOS models are applicable in specific density-temperature regimes and their accuracy decreases in other regimes. In this work we develop an EOS model which gives correct result in the liquid-vapour region along with accurate results for the densities above normal density. Tungsten carbide is important because of its applications in industrial machinery and high pressure systems. Despite the importance of WC in high-pressure studies, the theoretical study of elastic properties at high pressure has not been reported by other workers. In this thesis we present the results of our theoretical studies on EOS and elastic properties of tungsten carbide at high pressure.

For aluminium, we have also computed the electrical conductivity as a function of temperature & density. These studies are described in Sections 1 and 2, respectively.

EOS and electrical conductivity of Aluminium

In this Section, we report on EOS calculations for Al over large ranges of density and temperature. We also compute the electrical conductivity of Al. This work has been done in four parts:

- Full Potential Linearized Augmented Plane Wave (FP-LAPW) calculations for Al.
- Quantum molecular dynamics simulations for Al EOS and conductivity.

- Development of QEOS and its comparison with FP-LAPW and QMD results.
- Improvements in QEOS.

Computational details and important results are summarized below.

FP-LAPW calculations for Al

First principles study of compression of Al ($\rho > \rho_0$) at zero kelvin has been performed using the FP-LAPW method within the framework of density functional theory (DFT) [10, 11]. There are three reasons for performing this study. Firstly, this study yields the EOS at high pressure and zero kelvin ('cold-contribution'). Secondly, in a recent XRD experiment performed by Akahama et. al. [12], it has been found that the FCC-HCP structural transition occurs at 217 ± 10 and that FCC and HCP structures coexist over a large range of pressure. This coexistence can be understood using first principles calculations. Thirdly, in the same experiment, for the first time, high pressure values of lattice parameters of FCC and HCP structures have been reported. In our calculations, we have reported theoretical results of high pressure lattice parameters for the first time.

The cold contribution depends upon the crystal structure of the metal. Crystal structure of a metal can change on applying pressure and if the volume change at the transformation pressure is large then many thermodynamic properties such as Debye temperature, specific heat and melting temperature etc are significantly affected. Therefore, it is very important to study the effect of pressure on crystal structure and lattice parameters. The volume and pressure of structural transformation have been reported in previous studies [13, 14]. However, those studies were performed using different theoretical methods. In this thesis we have reported results of accurate FP-LAPW calculations using GGA exchange-correlation. We have also reported lattice parameters at high pressure. In addition we have discussed the structural transformation in terms of density of states (DOS).

Computational details:

We have used the WIEN2k code [15] to calculate the total energies of FCC, BCC and HCP structures of Al. This code performs electronic structure calculations of solids using the FP-LAPW method. This method is amongst the most accurate methods for performing first principles calculations for crystals and is used widely for the studies of structural properties of crystalline materials. The exchange correlation potential within LDA is calculated using the scheme of Perdwe-Wang [16], while the scheme of Perdew-Burke-Ernzerhof is used within GGA [17]

These calculations have been done using a constant muffin-tin radius R_{mt} of 1.7 a. u. In the WIEN2k code, it is very important to select a good basis set and k mesh size for getting accurate results. We start by taking a low value of $R_{\mathrm{mt}}K_{\mathrm{max}}$. For purposes of determining a suitable k -mesh size, we then calculate the total energy as a function of the size of the k-mesh., increasing the size by 1000 at each step. We find that 10000 k-points are sufficient. Having determined a good k -mesh, we now vary $R_{\mathrm{mt}}K_{\mathrm{max}}$ from 7 to 12, and find that 9.0 is a good choice. L_{max} is taken as 10 throughout the calculations. We have selected an energy cut-off of -6.0 Ry to separate the core from the valence states. The convergence criterion for energy was taken as 10^{-4} Ry.

Important results:

1. **Structural properties at ambient condition**

   To determine which option for the exchange-correlation functional is the most suitable for our purposes, we compared certain zero pressure properties viz., the lattice constants and the bulk modulus calculated by using GGA and LDA with their experimental values. The ground-state properties of the three phases of Al were obtained using the calculations of the total energy (E) as a function of volume (V) at lower pressures. E versus V data was then fitted to the Birch-Murnaghan equation of state [18] to obtain lattice parameters and bulk modulus at zero pressure. Calculated GGA and LDA lattice parameters and bulk modulus were compared to the experimental values and it was found that GGA results are more accurate. Hence in our subsequent calculations, we used GGA E versus V results.

2. **c/a ratio for HCP structure**

   We are interested in structural transformations in FCC, HCP and BCC structures at high pressures. For FCC and BCC, the only adjustable parameter is a. For HCP, however, the ratio c/a must also be specified. Hence it is first necessary to determine the c/a ratio that minimizes system energy at a given volume V/V_0. To this end, we have calculated the total energy for the HCP structure as a function of the c/a ratio for several densities. The c/a ratio was varied from 1.45 to 1.8. The experimental value of c/a ratio at ambient conditions is 1.6139. Hence the c/a ratio was varied from 1.45 to 1.8 for higher densities. This calculation was repeated for several values of V/V_0 spanning our range of interest. We have found that for densities near the normal density, the energy is minimum for a c/a ratio that deviates by 2% from the experimental value. Near the FCC-HCP transition and at higher densities, the energy was minimum for the 1.623 value of the c/a ratio.

3. **Lattice constants at high pressure**

   We have also calculated the lattice constants at higher pressures and compared the results with those obtained in recently reported X-ray powder diffraction experiments [12]. Our calculations show good agreement with the experimental values, the percentage errors lying within 0.5% in the calculated results for ‘a’(FCC and HCP), and within 0.4% for ‘c’ (HCP). Errors do not show any definite trend with the pressure. This is the first theoretical calculation of lattice parameters at high pressures.

4. **Total energy as function of Volume**

   To find the volumes at which structural transformations take place, we have compared the total energy versus volume curves of FCC, HCP and BCC structures. The differences (Δ) between the energies of FCC - HCP, FCC - BCC, and HCP - BCC were calculated and plotted as a function of the volume to determine the transition volume. From this plot we observe that the FCC-HCP transition occurs at $0.53V_0$. Experimentally, however, this transition has been found to lie at $0.509V_0$ [12]. The reason for this difference could be that $\Delta_{FCC-HCP}$ is negligibly small (of the order of 10^{-4} Ry) over the range V/V_0 = 0.51-0.53. It becomes significant 0.9 mRy at V/V_0 = 0.5089 and becomes 1 mRy when V/V_0 reaches 0.50. Such a small difference between the energies of FCC and HCP structures around the phase transition point could be the reason for the co-existence of the FCC and HCP structures over a wide range of densities.

5. **Pressure vs. enthalpy**

   For determining the FCC - HCP and HCP - BCC transition pressures, the differences between the enthalpies of FCC -HCP, FCC - BCC, and HCP - BCC were calculated and plotted as functions of the pressure. We find FCC - HCP transition pressure at 178 GPa whereas the reported experimental value is 217 ± 10 GPa [12]. This difference could be due to two reasons. Firstly, we have not included the energy contribution of zero point vibration. Secondly, there is a negligibly small difference between FCC and HCP enthalpies (1 mRy) in the pressure range of 178 - 217 GPa, hence there is a possibility that in the experiment the structural transformation may not be noticed until the enthalpy difference becomes significant.

6. **Density of states vs. Volume (Pressure)**

> The density of states (DOS) of FCC and HCP structures of Al has been calculated for normal and high pressures. It has been found that the DOS of both structures at normal conditions shows different kind of nature near the Fermi level but become similar over a range of compressed volumes close to the FCC-HCP transition volume ($V/V_0 = 0.53$). At ambient conditions, FCC - DOS at Fermi level lies in a local minima whereas HCP-DOS at Fermi level does not lie in any minima. At high pressures, the DOS of both structures at the Fermi level lies in local minima, implying that both structures are stable. This similarity can be one reason for the reported coexistence of FCC-HCP phases over a wide range of compressions near the FCC-HCP phase transition. Such explanations for the stability of crystal structures have been given for Au [19] and for Ti_2AlC and Ti_2AlN [20] in previous theoretical studies.

Thus from the first principles study of the structural and electronic properties (DOS) of Al we have generated the cold - curve of Al and also understood that FCC-HCP transition does not lead to any sudden change in the properties.

Quantum molecular dynamics simulation for EOS and electrical conductivity of Al

In the previous section, we had studied the cold curve in compressed states using a first principles method. In this section, we focus on studying the EOS and electrical conductivity of Al in the low density regime, $\rho < \rho_0$, where ρ_0 is the normal density at ambient conditions, by using quantum molecular dynamics (QMD) simulations or ab-initio molecular dynamics (AIMD) which is also based on the first principles method.

AIMD is a powerful simulation technique for calculating equation of state and electrical conductivity for low-temperature ($< 4-5$ eV) low density materials [21, 22].

In AIMD simulations, the energetics of the system and the forces on the ions are calculated by the first principle method, within the framework of finite temperature density functional theory (DFT). We have generated EOS and electrical conductivity data of low density Al using AIMD simulations in combination with the Kubo-Greenwood formula [23, 24]. Generating equation of state data on a closely-spaced grid of density and temperature is computationally very costly. Hence, we have generated EOS data using this method for a few density-temperature points on which interpolation is performed.

Computational details:

The exchange correlation interaction of the electrons are treated in the generalized gradient approximation (GGA), using the PBE parametrization [17]. Ion-electron interactions are described by the pseudo-potential generated by Troullier and Martins method. All calculations have been done at the Γ point, i .e., with number of k-points taken as one. In ABINIT, the energy cut off (ecut) is an important parameter which controls the number of plane waves, We performed several calculations at various values of ecut to investigate the convergence needed for reliable results and found that 272 eV is a good value for Al. The convergence criterion for energy was taken as 4.0×10^{-4} eV. Larger value of ecut and a smaller value of convergence criterion for energy do not make any significant change in the results. In the second step, the Kubo-Greenwood formula was used for the calculation of frequency-dependent electrical conductivity of Al. The quantities like Fermi Dirac occupation for each band and each k point, weight of each k point, electronic eigenstates and eigenvalues for each electronic state, and the derivative of the Hamiltonian with respect to the wave vector of the three directions, are required as input for the Kubo-Greenwood formula. These quantities are again calculated by the ABINIT [25]. For selected statistically-independent atomic configurations of 32 atoms, a self-consistent ground state calculation is performed with the ABINIT code to get the detailed electronic structure. For conductivity calculations, we found that four k points are necessary for better convergence. We ensured that there were always some unoccupied levels for better convergence of all runs.

Important results:

The calculated EOS and electrical conductivity is in good agreement with published theoretical and experimental results [21, 26]. From a plot of DC electrical conductivity σ (T) with temperature, we noticed that there is a change of slope at a certain temperature – for example, the slope decreases above 6000 K at a density of 2.35 g/cc. We have explained this using the Drude theory of electrical conductivity. According to this theory, electrical conductivity depends upon the number density of electrons at Fermi level n, and on the relaxation time τ. Hence, at low temperatures, the conductivity decreases rapidly with increasing temperature. This can be explained as follows - the ions vibrate about their equilibrium positions, which leads to thermal vibration of the crystal lattice. The amplitude of the vibrations increases as temperature is increased. The electrons are scattered by collisions with the lattice ions. Consequently, with the increase in the amplitude of vibration, the collision frequency increases. This leads to decrease in the relaxation time τ, and hence to decrease in the electrical conductivity. At high temperatures ($>$ 6000 K), even though the relaxation time is still decreasing with the temperature leading to decrease in the conductivity, the number density of electrons near the Fermi level also starts increasing, causing a net increase in the conductivity. Both these phenomena, viz., the decrease in the relaxation time and the increase in the number density of electrons near Fermi level jointly lead to less decrease in the electrical conductivity above the temperature 6000 K as compared to below this temperature. Hence, we see a break in the slope near 6000 K. This explanation has been given for the first time. However, further studies should be performed to confirm this explanation.

Development of QEOS and its comparison with FP-LAPW and QMD results

In the work reported above, we used first principles methods to calculate the cold contribution to the EOS. We also used first principles method based quantum molecular dynamics (QMD) for calculating the EOS in expanded states. Thus we have FPLAPW results for compressed states and QMD results for expanded states. Now we focus on developing a global equation of state model which can be used for compression as well as expansion and its results should be as accurate as the first principles results. However, before developing a new global EOS, we would like to compare the first principles EOS results with an existing global EOS model for compression as well as for expansion. The most popular global equation of state model is the Quotidian EOS (QEOS) model developed by More et. al [3]. We first develop a QEOS model following the methodology provided in the literature and then compare its results with first-principles results.

In QEOS, cold and electron thermal contributions are calculated by using the Thomas-Fermi (TF) statistical model of the atom and the ion-thermal contribution is calculated by using the Cowan model [3]. According to the TF model, each nucleus is located at the center of a spherical cavity, and electrons are treated as a charged fluid surrounding the nucleus and filled in the cavity to make it electrically neutral. The TF model does not consider the quantum mechanical structure of atoms and hence gives a positive pressure even at zero temperature due to the presence of free electrons inside the cavity. For the case of Al, it is approximately 1.0 million atmospheres (Megabar) at standard condition, whereas the actual pressure should be zero. Following More's methodology in QEOS, an empirical bonding correction is applied to the TF model to remove this inaccuracy.

The correction is applied in such a way that the pressure and bulk modulus are made to match the experimental value at normal conditions. This correction term has a progressively weaker effect as we move away from standard conditions. After implementing this correction, it was confirmed that 1. pressure becomes zero at standard condition. 2. the energy versus density curve exhibits a minimum at standard conditions and 3. bulk modulus is equal to its experimental value.

Important results:

The cold curve of QEOS was compared with the cold curve obtained from FP-LAPW and with the reported experimental cold curve generated by using powder X-ray method [12]. Good agreement was found.

We next compared our QEOS results with the EOS generated by using quantum molecular dynamics simulations in expanded states. Here, the agreement between the results *was not good* and hence an improvement of the QEOS is required for expanded states. There are three reasons for this disagreement. Firstly, in More's QEOS method, the cold curve is corrected by applying an empirical term which is a crude way of calculating the cold curve. Though it corrects the cold curve in the compression region, it does not account for the rarefaction region. Secondly, the formula used for calculating the Gruneisen parameter in the Cowan model is not suitable for expanded states as the calculated Gruneisen parameter diverges as density tends to zero. Thirdly, the thermodynamic properties at the critical point in the liquid-vapour region cannot be calculated accurately by using QEOS, since it is grossly inaccurate in that region.

These limitations are addressed in the next section of the thesis.

Improvement in QEOS

We have developed a new three-term EOS model in to address the limitations of More's QEOS model. In this model, we make improvements in the cold-curve and the ion-thermal term. The cold curve is calculated by three different methods in three different regions - 1. FP-LAPW method for densities ranging from standard conditions to the density corresponding to the compression at 1000 GPa. 2. Above this density we extrapolate the cold-curve using an analytical Thomas-Fermi-Dirac (TFD) extrapolation formula [5]. 3. For densities below normal, we calculate the cold-curve using a soft-sphere function [5].

For generating cold - curve using the FP-LAPW method, we have assumed Al to exist in the FCC structure at all pressures. In reality, pressure induced FCC - HCP and HCP - BCC structural transformations occur at high pressures, but differences in the energies of FCC and HCP structures and HCP and BCC structures are so small that these structures coexist over a wide range of pressures. This has been confirmed by experiments as well as by our previous theoretical studies. Hence we have calculated the cold - curve ignoring the FCC- HCP structural transition. Our cold - curve is in good agreement with XRD and shockwave measurements [12, 27, 28]. The constants of the extrapolated soft sphere function are calculated by applying the condition that 1. calculated energy and pressure using this function should match the energy and pressure calculated by FP-LAPW method at standard conditions and 2. the binding energy should be predicted correctly.

For the ion-thermal contribution, we have used the Cowan model which is used in More's QEOS model. However, we now calculate the Gruneisen parameter by imposing a condition that the calculated Pressure versus temperature isotherm matches reasonably with the isotherms generated by using QMD method. Other known conditions on Gruneisen parameter have also been imposed - that it should be close to its experimental value at ambient condition and should approach 2/3 at very high density.

Finally, the electron-thermal contribution is calculated using the TF model, i.e $E_{el} = E_{TF}(T) - E_{TF}(100K)$.

Important results:

This global EOS model is validated in compressed states by deriving $P - \rho$ and $U_s - U_p$ hugoniots and comparing them with available experimental results [29, 30]. Good agreement was found. In expanded states, this EOS model is validated by comparing isochores with the reported experimental isochores and thermodynamic properties at critical point with their reported values in the literature. The variation of pressure as a function of internal energy along the isochores shows good agreement with reported experimental results and the estimated critical temperature shows good agreement with reported results [31, 32]. Thus our EOS model is valid over large ranges of density and temperature.

EOS and Elastic Properties of Tungsten Carbide at high pressures

Introduction

Tungsten carbide is a promising material for applications in industrial machinery, cutting tools, and other instruments. In addition, because of its hardness it is also used as anvil in multi-anvil high pressure systems and as seats in diamond anvil cells [33-37]. Hence knowledge of equation of state and elastic properties of tungsten carbide is necessary.

The EOS and elastic properties of solids are closely related to many solid state properties such as specific heat, thermal expansion, Gruneisen parameter, Debye temperature, melting temperature and many others. At a more fundamental level the study of material behaviour at high compressions provides a better understanding of the interplay between the structural stability and electronic properties. Important information about the binding characteristics between adjacent atomic planes, the anisotropic character of the bonding and the structural stability etc can be deduced from the elastic properties.

In ambient conditions, the crystalline form of WC is a hexagonal structure known as α WC. This is a unique behaviour of WC among transition metal carbides as other carbides are stable in rock-salt structure. The structure of α WC can be viewed as alternating simple hexagonal layers of W and C. In addition to this α phase, WC can also exist in FCC structure at high temperatures, this phase is known as β WC.

Experimental investigation of EOS and elastic properties of WC at ambient and high pressures has been a subject of interest for more than two decades. Day and Ruoff [33] investigated pressure dependence of elastic moduli of WC with 3% Co binder up to 0.2 GPa, Gerlich and Kennedy [34] extended this investigation up to 1 GPa. Lee et. al. [35] determined the elastic constants of single crystal tungsten carbide at ambient conditions using high frequency ultrasonic pulse-echo measurements. Recently, Amulele et al [36] and Litasov et. al. [37] performed synchrotron X-ray diffraction measurements on polycrystalline powder samples loaded in a diamond anvil cell. Ultrasonic measurements on hot-pressed ceramics compressed in a multi-anvil high-pressure apparatus, have also been done in this paper [36]. In these measurements, pressure versus volume relations and elastic properties of WC have been determined.

On the theoretical side, several first principles calculation results have been reported among them the recent ones are [38, 39]. However the focus of these theoretical investigations has been on the physical, elastic and electronic properties at ambient conditions. Despite being a promising material for applications in high pressure apparatuses, the elastic properties of tungsten carbide at high pressure have not been reported by any author in a theoretical investigation.

In this work we present elastic properties of α and β WC up to a pressure of 120 GPa. We also perform comparison of enthalpies of α and β WC to investigate the competition between the structures of these phases in WC at high pressure. We discuss the outcomes of this competition in terms of density of states. We also discuss the stability, ductility/brittility and anisotropic behaviour of these phases at ambient and high pressures. Computational details and important results of the thesis are summarized below. The calculations have been performed using FPLAPW method as implemented in WIEN2K code.

Important results

Structural properties P-V isotherm and Gruneisen parameter

Calculated volume dependent total energy data of Îś and Îš tungsten carbide have been fitted to the Birch-Murnaghan EOS to obtain molecular volume (V_0), bulk modulus (B) and its pressure derivative (B_P). The obtained values of these properties are in good agreement with reported XRD and ultrasonic experimental values. The calculated $P - V$ isotherm at zero pressure is also in good agreement with reported experimental isotherms. As α tungsten carbide is hexagonal, its c/a value has been optimized at each volume, as was done in the case of Al. The c/a ratio of α - WC increases on increasing pressure. The calculated lattice parameters at high pressures have been compared with experimental values and reasonably good agreement has been found. The density dependent Gruneisen parameter has been deduced from the $P-V$ isotherm using Slater's formula.

Investigation of structural transformation

To investigate the structural transformations in tungsten carbide, the total energies versus volume ($E-V$) and Gibbs free energy (or enthalpy) versus pressure curves of α and β phases have been compared up to 350 GPa. It has been found that over the whole range of compression, the α phase remains stable and no α to β structural transformation takes place. To understand this in physical terms, the density of states (DOS) of α and β phases have been calculated at 0, 100 and 200 Gpa. It has been observed that DOS of the β phase lies in a local maximum at all pressures whereas the DOS of α phase at Fermi level lies in a local minimum at all pressures, making it thermodynamically stable. Moreover, the available states of α phase at Fermi level keep decreasing and the width of the minima keeps increasing on increasing pressure, providing more stability to the β phase at high pressures.

Elastic properties

Elastic properties such as bulk, shear and Young's modulus have been calculated upto a pressure of 120 GPa. The reported experimental data is available up to 14 GPa only. Our results are in good agreement with reported experimental data. We have found that the ratio of shear to bulk modulus (G/B) of both phases of WC are smaller than 1.0. This means that resistance to bond-length change exceeds the resistance to bond angle change in WC. G/B value of a material is also associated with the brittle or ductile character of the material. Low value is associated with ductility, the materials having G/B value smaller than 0.57 are ductile and materials with G/B value larger than 0.57 are brittle. At zero pressure, the G/B value of α and β WC are 0.86 and 0.61 respectively, implying that WC is a brittle material in both phases. Between both phases, β WC is less brittle and becomes ductile at 46 GPa. but α phase remains brittle up to 120 GPa. On increasing pressure, the G/B value of the α phase also goes down but it remains above the critical value of 0.57, implying that WC shows a tendency towards ductility on increasing the pressure but remains brittle up to 120 GPa. The brittle character of WC is also confirmed by its low value of Poisson ratio. It is believed that the materials with low Poisson's ratio are brittle [40] for example brittle metals with BCC structure have low value of Poisson's ratio whereas ductile FCC metals have high Poisson's ratio. The critical value of Poisson's ratio for separating brittle materials from ductile materials is 1/3, the brittle materials have Poisson's ratio smaller than this value.

The pressure dependent sound velocities (shear and longitudinal) have been calculated from the elastic properties have been calculated up to 120 GPa. These velocities show good agreement with the available experimental data. Pressure-dependent Debye and melting temperatures have been also deduced from the calculated sound velocities up to 120 GPa.

1. S. K. Sikka, B. K. Godwal and R. Chidambaram, *Equation of State at high pressure Shock Compression of Solids III.* Springer New York (1997) 1-35.

2. S. Eliezer, A. Ghatak and H. Hora, *An Introduction to Equations of State: Theory and Applications* Cambridge University Press (1986)

3. R. M. More, K H. Warren, D. A. Young, and G. B. Zimmerman, *Phys. of Fluids* **31** (1988) 3059.

4. David A. Young and Ellen M. Corey, *J. Appl. Phys.* **78** (1995) 3748.

5. G. I. Kerley, *Sandia National Laboratories Report* **No. SAND88-229175** (1991)

6. J. H. Degnan et. al. *Phys. Rev. Lett.* **74** (1995) 98.

7. P. V. Subhash, S. Madhavan, N. Sakthivel, P. Pahari, V. Mishra, A. Majalee and S. Chaturvedi, *Plasma Physics and Controlled Fusion* **53** (2011) 085013.

8. A. V. Majalee, V. Mishra, P.Pahari, V. R. Ikkurthi and S. Chaturvedi, *Proceedings of Indo-Russian Workshop on High Energy Density Physics for Innovative Technologies and Industry Applications*, I2IT, Pune, 19-21 Nov. 2008.

9. A. K. Saxena, T. C. Kaushik and Satish C. Gupta, *Rev. Sci. Instr.* **81** (2010) 033508 $(1-9)$.

10. W. Kohn and L. J. Sham, *Phys. Rev.* **140**, (1965) A1133.

11. L. J. Sham and W. Kohn, *Phys. Rev.* **145** (1966) 561.

12. Y. Akahama, M. Nishimura, K. Kinoshita and H. Kawamura, *Phys. Rev. Lett.* **96** (2006) 045505.

13. J.A. Moriarty, A.K. McMahan, *Phys. Rev. Lett.* **48** (1981) 809.

14. J.C. Boettger, S.B. Trickey, *Phys. Rev. B* **51** (1995) 15623.

15. P. Blaha, K. Schwarz, G.K.H. Madsen, D. Kvasnika, J. Luitz, *WIEN 2k, An Augmented Plane Wave Plus Local Orbital Program for Calculating Crystal Properties, Karlheinz Schwarz,Technical University, Wien, Austria* ISBN 3-9501031-1-2 (2001).

16. J.P. Perdew, Y. Wang, *Phys. Rev. B* **45** (1992) 13244.

17. J.P. Perdew, S. Burke, M. Ernzerhof, *Phys. Rev. Lett.* **77** (1996) 3865.

18. F.D. Murnaghan, *Proc. Natl. Acad. Sci. USA* **30** (1944) 244.
19. Rajeev Ahuja, Sandeep Rekhi, Borje Johansson, *Phys. Rev. B* **63** (2001) 212101.
20. Gilles Hug and Evelyne Fries, *Phys. Rev. B* **65** (2001) 113104.
21. M P Desjarlais, J D Kress and L A Collins 2002 *Phys. Rev. E* **66** 025401
22. P. R. Levashov, G. V. Sin'ko, N. A. Smirnov, D. V. Minakov, O. P. Shemyakin and K. V. Khihchenko, *J. Phys.: Condens. Matter* **22** (2010) 505501.
23. R. Kubo, *J. Phys. Soc. Jpn.* **12** (1957) 570.
24. D. A. Greenwood, *Proc. Phys. Soc. London* **71** 1958 585.
25. X Gonze et. al. *Comput. Mat. Sci.* **25** (2002) 478.
26. V. N. Korobenko and A. D. Rakhel, *Phys. Rev. B* **75** (2007).
27. A. D. Chijioke, W. J. Nellis, and I. F. Silvera, *J. Appl. Phy.* **98** (2006) 07526-1-7.
28. W. J. Nellis, J. A. Moriarty, A. C. Mitchel, M.Ross, R. G. Dandrea, N. W. Ashcroft, N. C. Holmes and G. R. Gathers, *Phys. Rev. Lett.* **60** (1988) 1414-1417.
29. I. V. Lomonosov, *Laser and Particle beams* **25** (2007) 567.
30. Michel Pénicaud, J. Phys. C: Cond. Matter **21** (2009) 095409.
31. A A Likalter 1996 *Phys. Rev. B* **53** 4386
32. H Hess and Z Metallkd 1998 as given in the review paper V Morel, A Bultel and B G Cheron 2009 *Int. J. Thermophy* **30** 1853
33. J. Paul Day and Arthur L. Ruoff, *Appl. Phys. Lett.* **44** (1973) 2447.

34. D. Gerlich and George C. Kennedy, *Appl. Phys. Lett.* **50** (1979) 2447.

35. M. Lee, R. S. Gilmore, *J. Mat. Sci.* **17** (1982) 2657.

36. George Amulele, Murli H Manghnani, Sekar Marriappan, Xinguo Hong and Fengug Li. *J. Appl. Phys.* **103** (2008) 113522.

37. Konstantin D. Litasov, Anton Shatskiy, Yingwei Fei, Akio Suzuki, Eiji Ohtani et. al. *J. Appl. Phys.* **108** (2010) 053513.

38. K. Gschneidner et al., *Nat. Mater.* **2** (2003) 587.

39. D. V. Suetin, I. R. Shein and A. L. Ivanovskii *J. Phys. Chem. Solids* **70** (2009) 64.

40. J. Schroers and W. L. Johnson, *Phys. Rev. Lett.* **93** (2004) 255506.

Contents

SYNOPSIS 1

List of Figures 25

List of Tables 29

1 Introduction 31

1.1 Equation of State 33

1.2 Application of Density Functional Theory in EOS 36

1.2.1 $T = 0$ contribution to EOS 37

1.2.2 Phase transitions under pressure 38

1.2.3 Quantum molecular dynamics 39

1.2.4 Elastic properties 40

1.3 Electrical conductivity 40

1.4 Motivation 41

1.5 Roadmap 43

2 Computational Methodology 45

2.1 Density functional theory 45

2.1.1 Adiabatic approximation 46

2.1.2 Variational Principle 48

2.1.3 The theorems of Hohenberg and Kohn 48

2.1.4 Kohn-Sham equations 50

2.1.5 Exchange - Correlation Potential 52

2.1.6 Solving Kohn-Sham Equations 54

2.2 Quantum Molecular Dynamics 58

2.2.1 Verlet Algorithm 59

2.2.2 Velocity Verlet Algorithm 60

2.2.3 Ensembles 60

2.2.4 Boundary Conditions 61

2.2.5 Thermostat 62

3 First principles study of structural phase transformations in Al 65

3.1 Introduction 66

3.2 Computational Details 69

3.3 Results and discussion 70

3.3.1 Total energy as a function of volume 70

3.3.2 Lattice constants and bulk modulus at normal pressure . . . 71

3.3.3 c/a ratio optimization for HCP structure 73

3.3.4 Lattice constants at higher pressure 75

3.3.5 Phase transformations under high pressure 75

3.3.6 FCC-HCP phase co-existence in terms of density of states . 79

3.4 Conclusion 81

4 Ab-initio calculations of EOS and conductivity of Al in expanded states, and comparison with Quotidian EOS results 83

4.1 Introduction 84

4.2 Computational Details 85

4.2.1 QEOS code using More's methodology 85

4.2.2 Full Potential Linearized Plane Wave (FPLAPW) Calculations 87

4.2.3 Ab-Initio Molecular Dynamics (AIMD) Simulations 87

4.3 Results and Discussion 88

4.3.1 QEOS-Results 88

4.3.2 Comparison of QEOS results with ab-initio calculations . . . 89
4.3.3 Electrical conductivity results 91
4.4 Conclusion 94

5 Improvements in QEOS model and determination of Al EOS for Compressed and Expanded States 97

5.1 Introduction 98
5.2 Computational Details 99
5.2.1 Cold-curve calculations 99
5.2.2 Ion-Thermal contributions 100
5.2.3 Electron-Thermal contributions 100
5.3 Results and Discussion 101
5.3.1 Cold-curve 101
5.3.2 Comparison of derived $P-\rho$ and $U_\mathrm{s}-U_\mathrm{p}$ Hugoniots with experimental Hugoniots for compressed Al 103
5.3.3 Expanded States 103
5.3.4 Estimation of Critical temperature 105
5.4 Conclusion 109

6 FP-LAPW Calculation of Equation of State and Elastic Properties of Tungsten Carbide at High Pressures 110

6.1 Introduction 111
6.2 Computational Details 113
6.2.1 Total energy calculation using FPLAPW method 113
6.2.2 Independent elastic constants of α and β WC. 113
6.2.3 Bulk and Shear Moduli 116
6.3 Results and Discussion 117

6.3.1 Molecular volume of α and β WC at ambient pressure . . . 117
6.3.2 Lattice parameters of α and β WC at high pressures. 118
6.3.3 Zero temperature $P-V$ isotherm of α WC. 120
6.3.4 Investigation of structural transformation 121
6.3.5 Interpretation of stability of α phase in terms of density of states 122
6.3.6 Qualitative discussion on the electrical conductivity of WC . 123
6.3.7 Grüneisen Coefficient of α and β WC 124
6.3.8 Bulk modulus, Shear Modulus and Young's modulus 128
6.3.9 Debye Temperature 132
6.4 Conclusion 135

7 Conclusions 137
7.1 Structural phase transformations in Al 138
7.2 Ab-initio calculations of EOS and conductivity of Al in expanded states 141
7.3 Improvement in QEOS model and determination of Al EOS for compressed and expanded states 142
7.4 Ab-initio calculation of EOS and elastic properties of WC at high pressures 143

Bibliography 146

List of Figures

2.1 An illustration of the full wavefunction for $3s$ and $3p$ orbitals of Al are plotted against distance, r, from the atomic nucleus. The corresponding pseudo wavefunction is also plotted. Outside a given radius, the full and pseudo values are identical. 56

2.2 Division of space into muffin-tin and interstitial regions. 57

2.3 Illustration of periodic boundary condition (PBC). When using periodic boundary conditions, a particle which exits the system on the right, will reappear on the left. 63

3.1 Energy as a function of c/a ratio for HCP structure at three densities; curves p, q and r correspond to V/V_0 0.71, 0.53 and 0.48, respectively. To allow plotting in the same figure, curve p has been shifted up by 0.14 Ry and curve r down by 0.09 Ry. 74

3.2 The pressure dependence of the lattice constants a_{HCP}, a_{FCC} and c_{HCP}. The solid line shows our calculations while points show experimental values from [62]. 75

3.3 The difference in energy between two structures of Al, as a function of normalized volume: $p = E_{\mathrm{HCP}} - E_{\mathrm{HCP}}$, $q = E_{\mathrm{FCC}} - E_{\mathrm{BCC}}$, $r = E_{\mathrm{HCP}} - E_{\mathrm{BCC}}$. 77

3.4 The difference in Gibbs free energy between two structures of Al, as a function of normalized volume: $p = G_{\mathrm{HCP}} - G_{\mathrm{FCC}}$, $q = G_{\mathrm{BCC}} - E_{\mathrm{FCC}}$, $r = E_{\mathrm{BCC}} - E_{\mathrm{HCP}}$. $p^{'}$ and $q^{'}$ represent the corresponding values from [51]. 78

3.5 Density of states (states/eV/atom) for aluminum at normal volume V_0. The solid and dotted lines represent FCC and HCP. The Fermi level is set at 0.0 eV. 80

3.6 Density of states (states/eV/atom) for aluminum at volume $0.53V_0$. The solid and dotted lines represent FCC and HCP. The Fermi level is set at 0.0 eV. 81

4.1 TF and QEOS cold pressures as functions of density at T=200 K. . 89

4.2 TF and QEOS cold energies as functions of density. 90

4.3 $U_s - U_p$ hugoniot. Solid line represents QEOS results and points represent experimental results [41,102]. 91

4.4 P-ρ hugoniot. Solid line represents QEOS results and points represent experimental results [30,102] 92

4.5 Cold curve generated by QEOS and FP-LAPW calculations and their comparison with experimental results [62,75,77] 93

4.6 Isotherm (10000 K) generated by QEOS and AIMD simulations . . 94

4.7 Optical conductivity of liquid aluminium at T = 12000 K and density = 2.35 g/cc. Points are showing the computed conductivities by Kubo-Greenwood formula and line shows the Drude fit. 95

4.8 DC conductivity as a function of temperature for liquid aluminium at density 2.35 g/cc. Filled squares represent results from [53], circles show results from the present work. 96

5.1 Comparison of theoretically calculated Cold-curve (zero-temperature isotherm) of Al with experimental 300 K isotherm. 101

5.2 Energy as a function of density; for $\rho/\rho_0 > 1$, it is calculated using FPLAPW method and for $\rho/\rho_0 < 1$, it is calculated using a soft sphere function. 102

5.3 $U_\mathrm{s} - U_\mathrm{p}$ Hugoniot. Solid line represents our results and points represent experimental results [41, 102] 104

5.4 P-ρ Hugoniot. Solid line represents our results and points represent experimental results [30, 102] 105

5.5 Isotherms for temperatures 10000 K and 15000 K. Points represent QMD results and line represents three term EOS fitted to QMD results. 106

5.6 Pressure versus internal energy along five isochores ($V/V_0 = 1.93, 2.7, 4.0, 5.4, 9.0$). Symbols represent experimental data taken from [58] and lines represent our calculation. 107

5.7 Isotherms for temperatures 7459 K, 7923 K 8387 K and 8859 K calculated by three term EOS model which is fitted to QMD simulation results. Straight lines $b-f$ and $b1-f1$ are the Maxwell constructions. 108

6.1 Variation of lattice parameters of α and β WC with pressure. . . . 119

6.2 Zero temperature isotherm of α WC 120

6.3 Variation of enthalpies of α and β WC with pressure. 121

6.4 Density of states curves of α (HCP) and β (FCC) WC at zero, 100 and 200 GPa 123

6.5 Variation of Grüneisen parameter of α and β phases of WC with the variation of the volume. 125

6.6 Bulk modulus and Shear modulus of WC. To allow plotting in the same figure curve of bulk modulus has been shifted up by 300 GPa. The experimental values have been extrapolated using the linear fits given in [35]. 131
6.7 Variation of ratio of shear to bulk modulus (G/B) of α and β WC with pressure (P). 132
6.8 Variation of longitudinal and shear velocities with the variation of pressure for α WC. The experimental values have been extrapolated using the linear fits given in the [35] 134

List of Tables

3.1 Atomic volume ($bohr^3$) and calculated total energies E (Ry/atom) for the FCC, HCP and BCC structures of Al 71

3.2 Calculated zero-pressure equilibrium lattice constants, bulk modulus and pressure derivative of bulk modulus, for the FCC, HCP and BCC phases of Al 72

3.3 The lattice constant a_0 (Bohr) and bulk modulus B_0 (GPa) for the FCC structure of Al 72

5.1 The coefficients of eq. 5.1, in Megabar 102

5.2 Values of b_1, b_2 and Grüneisen parameter 104

5.3 Critical density, temperature and pressure obtained in this work and reported results 107

6.1 Equilibrium volume, bulk modulus and pressure derivative of bulk modulus of tungsten carbide 118

6.2 The calculated elastic constants of α and β WC; P and C_{ij} are in GPa. 126

6.3 The calculated pressure dependent anisotropy constants of tungsten carbide 128

6.4 The calculated elastic moduli and Poisson's ratio of α and β WC; P, B, G, and E are in GPa. 129

6.5 Calculated Debye temperature and Melting temperature of α and β WC 134

1

Introduction

The study of matter at high pressure is of considerable current interest, particularly in the case of metals and compounds [1–3]. The knowledge of material equation of state and elastic properties at high pressure is important for a variety of scientific and engineering applications. In addition, equation of state and elastic properties of solids are closely related to many solid state properties such as specific heat, thermal expansion, Grüneisen parameter, Debye temperature, melting temperature and many others. At a more fundamental level the study of material behaviour at high pressure provides a better understanding of the interplay between the structural stability and the electronic properties. Important information about the binding characteristics between adjacent atomic planes, the anisotropic character of the bonding and the structural stability etc can be deduced from the elastic properties [4–7].

The equation-of-state (EOS) of a material represents the pressure P and internal energy E as functions of density and temperature of the material [8–11]. P and E can be expressed as the superposition of three terms, viz., (1) The Cold Curve, which refers to Pressure and energy at zero kelvin, (2) “Ion thermal” contribution, representing the contribution from thermal motion of ions, and (3) "Electron thermal" contribution, which is the contribution due to finite electron temperature.

The EOS is an essential input to hydrodynamic simulations of Magnetized Target Fusion systems and pulse power experiments [12–15]. Two examples will illustrate this point:

1. **Compressed states:**

   Electromagnetically-accelerated Liner experiments can give rise to large compressions and pressures of upto 50 million atmospheres (megabars). Hence there is a need for EOS calculations upto 100 Megabar and densities upto 6 times normal density.

2. **Rarefied states:**

   In exploding wire and laser irradiation experiments, temperatures of metals such as aluminium can reach upto a few tens of thousands of Kelvin (few eV), while densities can fall to as low as $1/10^{th}$ or $1/100^{th}$ of normal density. This combination lies in the 'dense plasma' state. If the plasma is produced by electrically-driven explosion, there is a need to generate EOS data over these low density states and temperatures upto 50,000 deg-K.

The EOS and conductivity models used must generate not only accurate but also "smooth" data. A large body of literature exists on the calculations of Equations of State. However, these EOS models are applicable in specific density-temperature regimes and their accuracy decreases in other regimes [8–11]. Hydrodynamic simulations for different problems require different kinds of EOS data. For example, simulations for Inertial Fusion Energy (IFE) and pulsed-power systems require wide-ranging data covering orders of magnitude in density and temperature. Simulations for exploding wires require data in rarefied states of metals, but the temperature range only extends upto 5 eV (50,000 K). Simulations for high-velocity impact require data upto only 5-10% compression, but with high accuracy, and must take account of solid-solid phase transformations.

This thesis studies the EOS and conductivity of certain materials over the range of parameters described above. This has, necessarily, involved the development/use of computer codes in a variety of areas.

Electrical conductivity is a property of a material which quantifies how well the material allows flow of an electric current. Fast opening switches based on electrically-exploded metal foils are of interest for pulsed power systems. Such explosions involve states with densities ranging from normal density ρ_0 down to $0.01\rho_0$ and temperatures ranging from room temperature up to a few electron volts. Modelling of electrically exploded fast opening switches requires the electrical conductivity data of the metal in this density-temperature regime, as an input. Hence there is a need to perform first principles study of conductivity of metals over these low density states and temperatures upto 50,000 deg-K.

1.1 Equation of State

The equation of state is described by a functional relationship between thermodynamic variables defined for a system in equilibrium. If one neglects electron-phonon interactions, the thermodynamic functions can be expressed as a superposition of three terms. In particular, one can write the energy E and pressure P in the following form [9]

$$E(V,T) = E_C(V) + E_{IT}(V,T) + E_{ET}(V,T) \tag{1.1}$$

$$P(V,T) = P_C(V) + P_{IT}(V,T) + P_{ET}(V,T) \tag{1.2}$$

where E_C and P_C are the energy and the pressure at zero temperature ($T = 0$ K), E_{IT} and P_{IT} are the contributions of ionic motions to the energy and pressure, while E_{TE} and P_{TE} are the electron thermal contributions. Here, the specific internal energy E has units of Joules/kg.

The first contribution to EOS is known as the 'cold' contribution. This comes from the kinetic energy of electrons, and Coulomb interaction between electron and nuclei, between electrons and other electrons and between nuclei and other nuclei. The cold curve (zero kelvin isotherm) can be constructed by a variety of empirical models such as Lennard-Jones(LJ) formula, EXP-N formula, and universal metal EOS formula [11] and semi-empirical models such as the Thomas Fermi model with bonding correction. Experimentally, it can be measured using a diamond anvil cell and can also be deduced from the experimental shock-hugoniot. The experimental data can be be fitted to a theoretical analytical form such as the Murnaghan equation of state [16] or an expression given by Sikka and Godwal [17]. The most accurate methods for calculating cold contribution are those derived from density-functional based electron band structure methods. Only atomic number and crystal structure is required as input in these methods.

Theoretical models have been described in the literature for calculating the ion-thermal contribution. The models given below cover different ranges of ρ and T:

1. If the material is in the solid state, energy and pressure can be calculated using the Debye model [19]

$$E_{IT} = \frac{3k_BT}{AM_p} D\left(\frac{\theta_D}{T}\right) \qquad P_{IT} = \gamma_s\left(\rho\right)\rho E_{IT} \tag{1.3}$$

A is the atomic mass and M_p is the mass or proton. ρ is the density,

$\gamma_s(\rho)$ is the density-dependent Gruneisen parameter of solids and D(x) is the Debye integral [18]. This equation applies for temperatures upto the Debye temperature θ_D.

2. The Dulong-Petit law applies to solids over the temperature range $\theta_D < T < T_m$. Energy is calculated using the following formula [18]

$$E_{IT} = 3\frac{k_B T}{AM_p} \tag{1.4}$$

and the pressure is still given by Equation 1.3.

3. The ideal gas law applies at either very high temperatures or very low densities:

$$E_{IT} = \frac{3}{2}\frac{k_B T}{AM_p} \qquad P_{IT} = \frac{\rho k_B T}{AM_p} \tag{1.5}$$

4. For temperatures above the melting point, a correction must be applied to the ideal gas expression to account for non-ideal dense fluids. The correction scales with the ratio $T_m(\rho)/T$, as explained in [20–22]:

$$E_{IT} = \frac{3}{2}\frac{kT}{AM_p}\left[1 + f\left(\frac{T_m}{T}\right)\right] \qquad P_{IT} = \frac{\rho k_B T}{AM_p}\left[1 + \gamma_F(\rho) f\left(\frac{T_m}{T}\right)\right] \tag{1.6}$$

where γ_F is fluid Gruneisen parameter, which is related to γ_s by:

$$1 + \gamma_F = 3\gamma_s \tag{1.7}$$

5. The density-dependent melting temperature $T_m(\rho)$ can be related to the Debye temperature $\theta_D(\rho)$ by Lindemann's melting law [23]

$$T_m(\rho)/\theta_D^2(\rho) = \alpha/\rho^{2/3} \tag{1.8}$$

In the present work, we have used the Cowan model [10] which is based upon the above laws. Details are given in chapter 4.

At low temperatures (<3-4 eV), the electron thermal contribution P_{TE} can be calculated using an expression similar to the Gruneisen equation of state, viz.

$$P_{IT} = \gamma_E \rho E_{IT} \tag{1.9}$$

while the energy due to thermal excitation of electrons can be calculated using a relation derived from the free electron model

$$E_{IT} = \frac{1}{2AM_p} \beta T^2 \tag{1.10}$$

Here, β is given by:

$$\beta = \beta_0 \left(\frac{V}{V_0} \right)^{1/2} \tag{1.11}$$

and γ_E is the electronic Gruneisen parameter. β_0 is a material dependent parameter related to electronic specific heat and can be measured experimentally. $\beta_0 = 500 \; erg \; g^{-1} \; deg^{-2}$ for Al [9]. At very high temperatures, the energy and pressure due electron thermal contribution can be calculated using the Thomas-Fermi model [24].

1.2 Application of Density Functional Theory in EOS

Density functional theory (DFT) is a quantum mechanical modelling method used in physics and chemistry to investigate the electronic structure of many-body systems, in particular atoms, molecules, and the condensed phases. The name density functional theory comes from the use of functionals of the electron density [25–28]. DFT is among the most popular and versatile methods available in condensed-matter physics, computational physics, and computational chemistry. This theory is now being increasingly employed for EOS work [29, 30].

The following studies, using density functional theory, are necessary for theoretically constructing accurate EOS tables.

1.2.1 $T = 0$ contribution to EOS

The specific internal energy E and pressure P, as functions of specific volume V at $T = 0$, can be obtained by electronic structure calculations if the stable crystal structure is known. From the calculated *E(V)* data, the pressure P and the bulk modulus B can be derived using the following equations:

$$P = -\frac{\mathrm{d}E}{\mathrm{d}V} \tag{1.12}$$

$$B = -V\frac{\mathrm{d}P}{\mathrm{d}V} = V\frac{\mathrm{d}^2E}{\mathrm{d}V^2} \tag{1.13}$$

The accuracy of these DFT calculations is limited by approximations made in treating electron-electron interactions, for which different models are available. Hence a direct comparison with experimental data is necessary, at least for some combinations of ρ-T. The first test is to determine the theoretical value of equilibrium volume V_0, where E is a minimum and P $=$ 0, and the bulk modulus B for the known zero-pressure crystal structure. Since V_0 and B can be measured with great accuracy, this is a rigorous test for the theory. In this procedure, energy E is calculated for several values of volume V, and is fitted to an analytical form, e.g., the Murnaghan equation of state [16]. The minimum gives the predicted volume V_0 and total energy, and the second derivative is the bulk modulus B.

1.2.2 Phase transitions under pressure

During computations, different pressures can be produced simply by adjusting the volume of a unit cell in a crystal. On reducing the volume, the distances between atoms is decreased and the materials sometimes exhibit a tendency to change the crystal structure. An in-depth study can sometimes reveal the physical reason for the change in structure.

In this thesis we have performed such studies for aluminium and tungsten carbide and have discussed the reasons for structural transformations and stability on the basis of their free energies, density of states and elastic properties. Our predictions regarding phase transformations have been compared with published experimental data to determine their accuracy.

The basic quantities involved in testing the stability of a structure are the Helmholtz free energy $F(V,T) = E(V,T) - TS(V,T)$, where the volume V and the temperature T are the independent variables, or the Gibbs free energy $G(P,T) = H(P,T) - TS(P,T)$, where the pressure P and T are the independent variables. The enthalpy H is given by

$$H = E + PV \tag{1.14}$$

At temperature T = 0, the condition for a stable structure at constant pressure P is that enthalpy be a minimum. One can also determine transition pressures by calculating E(V) and using the Gibbs construction of a tangent line between the E(V) curves of two phases, the slope of which is the pressure for the transition between phases.

1.2.3 Quantum molecular dynamics

In Quantum Molecular Dynamics (QMD), forces on the nuclei are calculated using electronic structure theory. Atomic movement (dynamics) is performed in the same way as in classical molecular dynamics. In QMD, the problem of electronic structure and motion of nuclei are treated together. Although some approximations are used, these have some theoretical basis instead of being based on empirical fitting [25]. In addition to evolving atomic coordinates and velocities, QMD also produces detailed information about the time-evolution of electron density distribution and other electronic properties, which provides insight into the underlying physics.

Among the foremost challenges in EOS calculations is to understand the behaviour of metals in the liquid-vapour region. Also, as mentioned earlier, MHD modelling of exploding conductors requires accurate EOS data for densities ranging from normal density to a fraction of normal density and for temperatures up to a few thousand kelvin. This is a regime where first principles QMD can provide crucial information, complementing experiments that are very difficult at these temperatures and densities. In this thesis, we have studied thermal properties of aluminium in the liquid-vapour region using QMD results. We have used this method only for expanded states because the QMD method is based on pseudopotentials which would be most accurate for densities below normal density and may not be accurate in compression. In any case, for compressed states, it would be more accurate to calculate the cold contribution using a full potential based DFT method and then combine it with thermal models to get the full EOS.

1.2.4 Elastic properties

Elastic properties of a solid are important because they are linked thermodynamically to the Debye temperature, melting temperature, Gruneisen parameter, specific heat and thermal expansion. They also relate to various fundamental solid-state properties such as equation of state, inter-atomic potentials and phonon spectra. For the calculation of elastic constants, we have to distort the crystal by bending and perform a calculation of total energy. The total energy of a distorted crystal includes energy due to change of volume and elastic energy (due to shape change) in addition to the cold energy. The elastic energy depends on the elastic constants.

A cubic crystal has three independent elastic constants. Hence, in order to determine these by total energy calculation using DFT, three types of distortions of the crystal are required to set up three equations. Similarly, a hexagonal crystal has five independent elastic constants; hence five types of distortions would be required to form five equations in terms of five unknown independent elastic constants. In this thesis, we have studied elastic properties of tungsten carbide at normal and high pressures.

1.3 Electrical conductivity

In laser heated and electrically-exploded wire/foil experiments, matter can reach a regime where density is below normal and temperature goes up to 40,000-50,000 K. Hydrodynamic and MHD simulations of such systems require electrical conductivity data along with EOS data. Hence electrical conductivity data as well as proper understanding of the conducting nature of the material in this regime is necessary. For this purpose, we have also studied the behaviour of electrical conductivity in this regime for aluminium.

In this regime, aluminium does not exist in a crystalline state. Hence atomic configurations have to be determined using QMD runs keeping system volume and temperature constant. Starting with an arbitrary initial configuration, the atomic configuration is evolved using QMD until the pressure and energy start oscillating about a mean. This can be called the ‘equilibrated portion’ of the run. From this portion, we can select atomic configurations and use them for the calculation of electrical conductivity using the Kubo-Greenwood formula [31–33]. This formula is a general expression for the conductivity and includes electron-electron and electron-ion interactions. It calculates the conductivity directly from the electronic wavefunction.

1.4 Motivation

High-pressure studies of practical importance can involve elements as well as compounds. As discussed earlier, pulsed-power experiments such as electromagnetically-accelerated liners and exploding foils make use of Aluminium. Hence there is a pressing need for studying the EOS and other properties of Al in detail. Some other high-pressure applications and studies require the use of ceramics. Tungsten carbide (WC) is used as an anvil in multi-anvil high pressure systems and as seats in diamond anvil cells [34]. It is also a promising material for applications in industrial machinery, cutting tools, and other instruments due to its hardness [35]. Hence, in this thesis, we first perform a study of the EOS and electrical conductivity of Al in detail, and then extend the EOS study to WC.

Due to its importance as discussed above, theoretical and experimental investigation of EOS of metals, particularly of aluminum, is of great interest for many years.

On the theoretical side, several thermodynamic theoretical models [8–11, 36–41] are available in literature. The thermodynamic properties of Al in different density - temperature regimes including liquid - vapor regimes have been studied using such theoretical models in [10, 42, 43]. Electronic structure calculations have been performed for studying zero temperature isotherms and pressure induced structural transformations [44–51]. Quantum molecular dynamics simulations have been performed for the calculation of EOS and electrical conductivity in the rarefied region [52–59]. The results of these theoretical EOS are tested by comparing them with the experimental EOS. In the literature there are several approaches to determine experimental EOS at high pressures. Absolute isothermal pressure-volume measurements can be done using diamond anvil cells [60–62]. Shock-wave compression techniques can be used to obtain EOS data at high pressures and temperatures [63–68]. High power lasers and pulse power discharges are important tools for EOS experiments [69–74]. Room temperature isotherms can be deduced from the shock wave EOS data using modest state-of-the-art corrections [75–77]. Thus a large body of experimental and theoretical EOS data are available in the literature. However, there are three major shortcomings in the foregoing electronic structure studies. Firstly, none of the studies have calculated lattice parameters of Al at higher pressures theoretically and secondly, there is a lack of theoretical understanding for the coexistence of FCC and HCP phases over a wide range of pressures. Thirdly none of the electronic structures calculations have been performed using FPLAPW method with GGA as exchange and correlation. Hence, its necessary to perform more accurate DFT calculations using the full-potential (FP) linearized augmented plane wave (LAPW) method, using GGA. This forms the subject of the present investigation. Moreover, thermodynamic properties of Al in the liquid-vapour regime are not well known. These properties are predicted inaccurately by More's QEOS model [10]. Attempts have been made to make the improvements in QEOS [42, 43]. However, these attempts are based on empirical theoretical models. In order to improve QEOS by incorporating ab-initio (AIMD) results, it is necessary to make a comparison of QEOS and ab-initio calculations. In this thesis we have first made such comparison to identify the descrepancies of QEOS. We next improved QEOS by incorporating ab-initio results to remove the descrepancies.

Similarly, for tungsten carbide, several first principles calculation results have been reported [78–83]. However, the focus of these theoretical investigations has been on the zero pressure physical, elastic and electronic properties. Despite being a promising material for applications in high pressure devices, elastic properties of tungsten carbide at high pressure have not been reported by any author in any theoretical investigation. Elastic properties are colsely related to EOS and its constituent properties such as Debye temperature, melting temperature etc. Hence it is necessary to perform FPLAPW calculations of EOS, elastic properties and other constituent properties of WC at high pressure.

1.5 Roadmap

This thesis is organized as follows. In Chapter 2, we have explained the basics of our computational techniques. Density functional theory is described in detail. We further discuss the Kohn-Sham equations and techniques, viz., pseudopotential method and full potential linearized augmented plane wave (FP-LAPW) method, to find the solutions of the Kohn-Sham equations. We have also described the exchange correlation potentials. In addition, we also explain the basic technique used in quantum molecular dynamics.

In Chapter 3, we have described the study of crystal structure transformation in aluminium on applying high pressure, using ab-initio method. We have performed a comparative study of the effects of Local Density Approximation (LDA) and Generalized Gradient Approximation (GGA) on properties like equilibrium volume, lattice parameter, bulk modulus etc. We have also calculated lattice parameters at high pressures.

In Chapter 4, we report on ab-initio and quotidian equation of state (QEOS) results for Al, followed by a comparative study of ab-initio and QEOS methods to identify the limitations of QEOS. We also present and discuss Quantum Molecular Dynamics results for the electrical conductivity of aluminium.

In chapter 5, we describe the development and evaluation of an improved QEOS model. Using the improved QEOS algorithm, we estimate important thermodynamic properties such as critical temperature, pressure and volume in the liquid-vapour region.

In chapter 6, we have described results of FP-LAPW calculations for tungsten carbide, including EOS and structural phase transformations. We have also studied the stability and ductile/brittle nature of different phases of WC.

2

Computational Methodology

2.1 Density functional theory

The microscopic description of the physical and chemical properties of matter is a complex problem. In general, we deal with a collection of interacting atoms, which may also be affected by an external field. If we have N atoms with atomic number Z, we must deal with a problem of N+ZN electromagnetically interacting particles. This amounts to a quantum many-body problem. The Hamiltonian of such a system can be written as [25, 27]:

$$\begin{aligned}\hat{H} = &-\frac{\hbar^2}{2}\sum_{I=1}^{N}\frac{\nabla^2{}_{\mathbf{R_I}}}{M_I} - \frac{\hbar^2}{2}\sum_{i=1}^{n}\frac{\nabla^2{}_{\mathbf{r_i}}}{m_e} - \frac{1}{4\pi\epsilon_0}\sum_{I=1}^{N}\sum_{j=1}^{n}\frac{e^2 Z_i}{|\mathbf{R_I}-\mathbf{r_j}|} \\ &+\frac{1}{8\pi\epsilon_0}\sum_{i=1}^{n}\sum_{j\neq i}^{n}\frac{e^2}{|\mathbf{r_i}-\mathbf{r_j}|} + \frac{1}{8\pi\epsilon_0}\sum_{I=1}^{N}\sum_{J\neq I}^{N}\frac{e^2 Z_I Z_J}{|\mathbf{R_I}-\mathbf{R_J}|}\end{aligned} \tag{2.1}$$

M_I and m_e are the nuclear and electron masses, and $\mathbf{R_I}$ (I = 1, ...N) and $\mathbf{r_i}$ (i = 1 ......n) are their respective positions. The first and second terms are kinetic energy operators of nuclei and electrons respectively. The last three terms describe the Coulomb interaction between electrons and nuclei, between electrons and other electrons, and between nuclei and other nuclei.

This Hamiltonian can be used in the many-body Schrodinger equation to derive all properties.

$$\hat{H}\Psi_i\left(\mathbf{r_1},\mathbf{r_2},...,\mathbf{r_n},\mathbf{R_1},\mathbf{R_2},...,\mathbf{R_N}\right) = E_i\Psi_i\left(\mathbf{r_1},\mathbf{r_2},...,\mathbf{r_n},\mathbf{R_1},\mathbf{R_2},...,\mathbf{R_N}\right) \tag{2.2}$$

This problem is almost impossible to treat in a full quantum-mechanical framework. A complete analytic solution is possible only in a few simple cases and numerical solutions are also limited to a very small number of particles.

There are several features that contribute to this difficulty [25]. First, this is a multicomponent many-body system, where each component (each nuclear species and the electrons) obeys a particular statistics. Second, the complete wave function cannot be easily factorized because of coulombic correlations. In other words, the full Schrodinger equation cannot be easily decoupled into a set of independent equations so that, in general, we have to deal with (3N + 3n) coupled degrees of freedom. The dynamics is an even more difficult problem, and very few and limited numerical techniques have been devised to solve it. The usual choice is to resort to some sensible approximations. In order to find acceptable approximate solutions, we need to make approximations at three different levels, which are described in Sections 2.1.1, 2.1.4 and 2.1.5.

2.1.1 Adiabatic approximation

The nuclei are much heavier and therefore much slower than electrons. The timescale associated with the motion of nuclei is usually much longer than that associated with electrons. In fact, the small mass of electrons as compared with that of protons means that electrons have much higher velocities. We can hence freeze nuclei at fixed positions and assume the electronic wave function to be in instantaneous equilibrium with them. The nuclei are reduced to a given source of positive charge, external to the electron cloud. After having applied this approximation, we are left with a collection of NZ interacting negative particles, moving in the potential of the nuclei [26].

The adiabatic approximation thus means that the nuclei do not move any more, their kinetic energy is zero and the first term of Eq. 2.1 disappears. The last term of this equation reduces to a constant. Three terms describing the kinetic energy of the electron gas, the potential energy due to electron-electron interaction and the potential energy of the electrons in the external potential of the nuclei are left in equation 2.1. These terms can be rewritten as:

$$\hat{H} = \hat{H}_{el} = \hat{T} + \hat{V}_{ee} + \hat{V}_{ext} \tag{2.3}$$

The solution of the Schrødinger equation with $\hat{H}_{el}$ is the electronic wave function Ψ_{el} and the electronic energy E_{el}. The total energy E_{tot} is then the sum of E_{el} and the constant nuclear repulsion term E_{nuc}.

$$\hat{H}_{el}\Psi_{el} = E_{el}\Psi_{el} \tag{2.4}$$

$$E_{tot} = E_{el} + E_{nuc} \quad \text{where} \quad E_{nuc} = \sum_{A=1}^{N}\sum_{B>A}^{N}\frac{Z_A Z_B}{R_{AB}} \tag{2.5}$$

Several methods exist to solve equation 2.4, such as the Hartree-Fock (HF) method and density functional theory (DFT). Both methods use a variational principle for solving the equation.

2.1.2 Variational Principle

When a system is in the state Ψ, the expectation value of the energy is given by

$$E\left[\Psi\right]=\frac{\langle\Psi|\hat{H}|\Psi\rangle}{\langle\Psi|\Psi\rangle} \quad \text{where} \quad \langle\Psi|\hat{H}|\Psi\rangle=\int\Psi^{*}\hat{H}\Psi d\mathbf{r} \tag{2.6}$$

The variational principle states that the energy computed from a guessed Ψ is an upper bound to the true ground-state energy E_0. Full minimization of the functional $E\left[\Psi\right]$ with respect to all allowed n-electron wave functions will give the true ground state Ψ_0 and energy $E\left[\Psi_0\right]=E_0$.

For a system of n electrons and given nuclear potential V_{ext}, the variational principle defines a procedure to determine the ground-state wave function Ψ_0, the ground-state energy $E_0\left[N,V_{ext}\right]$, and other properties of interest. The ground state energy is then a functional of the number of electrons n and the nuclear potential V_{ext}:

$$E_0=E\left[N,V_{ext}\right] \tag{2.7}$$

2.1.3 The theorems of Hohenberg and Kohn

DFT was formally established in 1964 by two theorems due to Hohenberg and Kohn [84,85].

First Theorem: For any system of interacting particles in an external potential $V_{ext}\left(\mathbf{r}\right)$, the potential $V_{ext}\left(\mathbf{r}\right)$ is determined uniquely, except for a constant, by the ground state electron density $\rho\left(\mathbf{r}\right)$.

An immediate consequence is that the ground state expectation value of any observable $\hat{O}$ is a unique functional of the exact ground state electron density:

$$\langle\Psi|\hat{O}|\Psi\rangle = O\left[\rho\right] \tag{2.8}$$

For $\hat{O}$ being the Hamiltonian $\hat{H}$, the ground-state total energy functional is of the form

$$E\left[\rho\right] = \langle\Psi|\hat{T}+\hat{V}|\Psi\rangle + \langle\Psi|\hat{V}_{ext}|\Psi\rangle = F_{HK}\left[\rho\right] + \int \rho\left(\mathbf{r}\right) V_{ext}\left(\mathbf{r}\right) d\mathbf{r} \tag{2.9}$$

where $F_{HK}\left[\rho\right]$ is Hohenberg-Kohn energy functional.

Second Theorem: The second H-K theorem states that $F_{HK}\left[\rho\right]$, the functional that corresponds to the ground state energy of the system, yields the lowest energy if and only if the input density is the true ground state density. This is nothing but the variational principle:

$$E_0 \leq E\left[\rho^{'}\right] = F_{HK}\left[\rho^{'}\right] + \int \rho^{'}\left(\mathbf{r}\right) V_{ext}\left(\mathbf{r}\right) d\mathbf{r} \tag{2.10}$$

This means that for any trial density $\rho^{'}\left(\mathbf{r}\right)$, which satisfies the necessary boundary conditions such as $\rho^{'}\left(\mathbf{r}\right) \geq 0$, $\int \rho^{'}\left(\mathbf{r}\right) d\mathbf{r} = n$ and which is associated with some external potential $V_{ext}\left(\mathbf{r}\right)$, the energy obtained from the solving the Schrodinger equation represents an upper bound to the true ground state energy E_0. Energy E_0 results if and only if the exact ground state density is inserted in the Schrodinger equation.

2.1.4 Kohn-Sham equations

The universal functional $F_{HK}[\rho]$ contains exact kinetic energy $T[\rho]$ and electron-electron potential energy $V[\rho]$ functionals of the interacting many electron system. Using Schrodinger equation at this stage would lead to difficult system of coupled differential equations, because of the electron - electron interaction. To overcome this difficulty Kohn-Sham suggested to replace the Hamiltonian of interacting electrons with the Hamiltonian of non-interacting electrons plus an exchange correlation term. This is done in the following way. Let us suppose that $T_0[\rho]$ and $V_H[\rho]$ be the kinetic and potential energy functionals of non - interacting many electron system. Then we can write the following:

$$\begin{aligned} F_H K &= T + V \\ &= T + V + T_0 - T_0 + V_H - V_H \\ &= T_0 + V_H + (T - T_0) + (V - V_H) \\ = T_0 + V_H + V_C + V_X \quad & V_X : \text{Exchange term}, \quad V_C : \text{Correlation term} \\ &= T_0 + V_H + V_{XC} \end{aligned} \tag{2.11}$$

where V_{XC} is the exchange-correlation energy functional. This functional is not known exactly, since it contains the difficult exchange and correlation contributions. If we assume for a while that we do know V_{XC}, we can write explicitly the energy functional:

$$E[\rho] = T_0[\rho] + V_H[\rho] + V_{XC}[\rho] + V_{ext}[\rho] \tag{2.12}$$

The corresponding Hamiltonian is

$$\begin{aligned} \hat{H_{KS}} &= \hat{T}_0 + \hat{V}_H + \hat{V}_{XC} + \hat{V}_{ext} \\ &= -\frac{\hbar^2}{2m_e}\nabla^2 + \frac{e^2}{4\pi\epsilon_0}\int \frac{\rho\left(\mathbf{r}'\right)}{\left|\mathbf{r}-\mathbf{r}'\right|}d\mathbf{r}' + V_{XC} + V_{ext} \end{aligned} \tag{2.13}$$

Using this Kohn-Sham Hamiltonian we can find the single particle wave function by solving the following Kohn-Sham equation for the n lowest energy solutions

$$\hat{H}_{KS}\psi_i = \epsilon_i\psi_i \tag{2.14}$$

Using these single particle wave functions we can find the exact ground state electron density

$$\rho\left(\mathbf{r}\right) = \sum_{i=1}^{n} \psi_i\left(\mathbf{r}\right)^{*}\psi_i\left(\mathbf{r}\right) \tag{2.15}$$

The exchange correlation operator and the Hartree operator depend on the electron density $\rho\left(\mathbf{r}\right)$. The electron density $\rho\left(\mathbf{r}\right)$ depends on the ψ_i which are being searched. The solutions ψ_i determine the $\hat{H}_{KS}$ (V_{XC} and V_H of Hamiltonian) and the equation cannot be constructed and solved until its solution is known. This is a self-consistency problem, which can be solved using an iterative procedure. An initial guess of the electron density ρ_0 is made and with this density the exchange correlation operator and the Hartree operator are calculated and the Hamiltonian is constructed. Then the Kohn-Sham equations are solved to obtain single particle wave function ψ_i. From these wavefunctions, the electron density ρ_1 is calculated. Then ρ_0 is compared with ρ_1. If these are different then the same procedure is repeated until we converge to a stage where input and output electron densities are almost the same.

2.1.5 Exchange - Correlation Potential

The important achievement of the Kohn-Sham equations is the separating out of the independent-particle kinetic energy and the long range Hartree terms. The remaining exchange-correlation functional can be reasonably approximated as a local or nearly local functional of the density. Even though the exact functional must be very complex, great progress has been made with remarkably simple approximations. A few of them are described in this section [25–27].

Local density approximation (LDA):

The local density approximation (LDA) is the basis of all approximate exchange-correlation functionals. This model starts with the idea of a uniform electron gas. This is a system in which electrons move on a positive background charge distribution such that the total ensemble is neutral. The central idea of LDA is the assumption that we can write E_{XC} in the following form

$$E_{XC}^{LDA} = \int \rho\left(\mathbf{r}\right) \epsilon_{xc}\left(\rho\left(\mathbf{r}\right)\right) d^3\mathbf{r} \tag{2.16}$$

where, $\epsilon_{xc}\left(\rho\left(\mathbf{r}\right)\right)$ is the exchange-correlation energy per particle of a homogeneous electron gas (HEG) of density $\rho\left(\mathbf{r}\right)$. This energy per particle is weighted with the probability $\rho\left(\mathbf{r}\right)$ that there is an electron at this position. The quantity $\epsilon_{xc}\left(\rho\left(\mathbf{r}\right)\right)$ can be further split into exchange and correlation contributions,

$$\epsilon_{xc}\left(\rho\left(\mathbf{r}\right)\right) = \epsilon_{x}\left(\rho\left(\mathbf{r}\right)\right) + \epsilon_{c}\left(\rho\left(\mathbf{r}\right)\right) \tag{2.17}$$

The exchange part, ϵ_x, which represents the exchange energy of an electron in a uniform electron gas of a particular density, was originally derived by Bloch and

Dirac in the late 1920's

$$\epsilon_x = -\frac{3}{4}\left(\frac{3}{\pi}\right)^{1/3}\int \rho\left(\mathbf{r}\right)d^3\mathbf{r} \tag{2.18}$$

No such explicit analytical expression is known for the correlation part, ϵ_c, except in the high- and low-density limits corresponding to infinitely-weak and infinitely-strong correlation. These are calculated in terms of Wigner-Seitz radius, which is related to the density as

$$\frac{4}{3}\pi {r_s}^3 = \frac{1}{\rho} \tag{2.19}$$

Gellmann and Breuckner [86] proposed the following infinite series for the high-density limit of the correlation energy

$$\epsilon_c\left(r_s\right) = A\,\ln\left(r_s\right) + B + r_s\left(C\,\ln\left(r_s\right) + D\right) \ldots\ldots \tag{2.20}$$

where the *ln* terms are the signature of non-analyticity that causes so much difficulty. At low density the system can be considered a Wigner crystal with zero point motion leading to

$$\epsilon_c\left(r_s\right) = \frac{a_1}{r_s} + \frac{a_2}{{r_s}^{3/2}} + \frac{a_3}{{r_s}^2} \ldots\ldots\ldots \tag{2.21}$$

Accurate quantum Monte Carlo simulations for the energy of the HEG have been performed for several intermediate values of the density, in turn providing accurate values of the correlation energy density. One very important result is that for materials at typical solid densities ($r_s \approx 2-6$), the correlation is much smaller than the exchange energy; however at very low densities (large r_s) correlation becomes more important and dominates in the regime of the Wigner crystal

$(r_s >\approx 80)$

Generalised gradient approximation (GGA):

The first logical step to go beyond LDA is to combine information about the density $\rho(\mathbf{r})$, at a particular point $\mathbf{r}$, but to supplement the density with information about the gradient of the charge density, $\nabla\rho(\mathbf{r})$, in order to account for the non-homogeneity of the true electron density. Several parameterizations of LDA and GGA exist in literature [87–91]

2.1.6 Solving Kohn-Sham Equations

After separating out kinetic energy and Hartree terms we end up with the following Kohn-Sham equation for non-interacting electrons

$$\left(-\frac{\hbar^2}{2m_e}\nabla^2 + \frac{e^2}{4\pi\epsilon_0}\int\frac{\rho(\mathbf{r}')}{|\mathbf{r}-\mathbf{r}'|}d\mathbf{r}' + V_{XC} + V_{ext}\right)\psi_m(\mathbf{r}) = \epsilon_m\psi_m(\mathbf{r}) \tag{2.22}$$

where $\psi_m(\mathbf{r})$ are single particle wavefunction. Solving means finding the coefficients c_p^m, required to expand $\psi_m(\mathbf{r})$, in terms of a given basis set ϕ_p

$$\phi_m = \sum_{p=1}^{P} c_p^m \phi_p \tag{2.23}$$

In principle, P should be infinite to exactly represent ϕ_m, but, in practice, we can not work with infinite coefficients therefore we limit the number of P in such a way that it represents a function which is close to ϕ_m.

It can be shown that any eigenfunction $\psi_{\mathbf{k}}^n$ of a periodic Hamiltonian can be expressed in terms of a plane wave basis set $\phi_{\mathbf{K}}^{\mathbf{k}}(\mathbf{r}) = e^{i(\mathbf{k}+\mathbf{K}).\mathbf{r}}$ with infinite number of coefficients

$$\psi_{\mathbf{k}}^{n}(\mathbf{r}) = \sum_{\mathbf{K}} c_{\mathbf{K}}^{n,\mathbf{k}} e^{i(\mathbf{k}+\mathbf{K}).\mathbf{r}} \tag{2.24}$$

where $\mathbf{k}$ is a vector in the first Brillouin zone and $\mathbf{K}$ is a reciprocal lattice vector. n is the number of Brillouin zone where $(\mathbf{k}+\mathbf{K})$ is in.If we compare this with equation 2.23, we can see that m stands for $(n, \mathbf{k})$ and p stands for $\mathbf{k}+\mathbf{K}$.

Since we cannot work with an infinite set of coefficients we will have to limit it to some finite number in such a way that the summation still gives an eigenfunction which is close to the true eigenfunction. This is done by limiting the plane wave basis set to all $\mathbf{K}$ with $\mathbf{K} \leq \mathbf{K_{max}}$. Often, the free electron energy corresponding to $\mathbf{K_{max}}$ is specified instead of $\mathbf{K_{max}}$ itself. This energy is called cut-off energy E_{cut}.

$$E_{cut} = \frac{\hbar^2 {K_{max}}^2}{2m_e} \tag{2.25}$$

The number of plane waves is determined by the smallest length scales that are to be taken into account in real space. As shown in figure 2.1, near the nucleus the wave functions show steep and oscillatory behaviour. In order to describe this part of the wave function, a very large number of plane waves will be needed that would require diagonalization of a very large matrix and would make the calculations almost impossible. This problem is solved by using different methods such as pseudopotential and linearized augmented plane wave (LAPW) methods.

Pseudopotential Method

In an atom, the part of the wave function of an electron which reaches close to the nucleus exhibits the most oscillatory behaviour. However, in a solid, interaction with neigbouring atoms occurs due to wave functions which are in the outer region of the atom (away from the nucleus). Hence the inner oscillating regions are shielded, to a great extent, by the outer region. The pseudopotential method assumes that there is no need to perform calculations for these inner regions. We can therefore replace the potential of the nucleus by a pseudopotential in such a way that the wavefunction in this inner region is very smooth, so that few plane waves would be needed to describe this part of the wavefunction. Towards the outer region of the atom, the pseudopotential continuously evolves into the true potential.

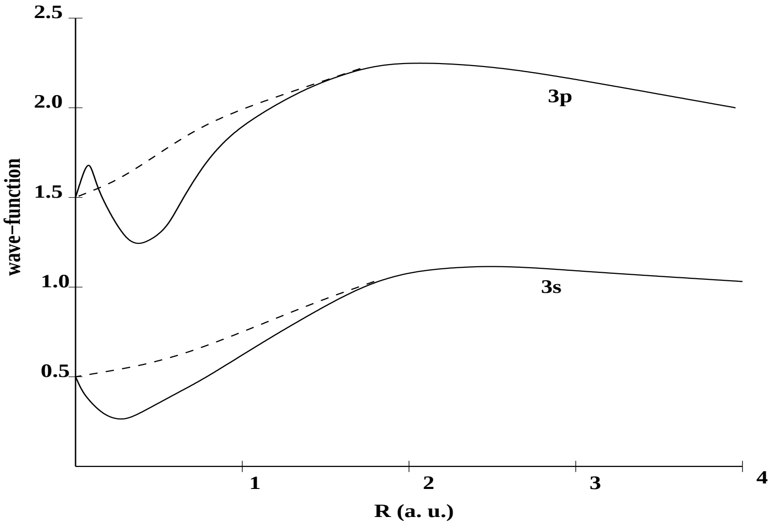

Figure 2.1: An illustration of the full wavefunction for $3s$ and $3p$ orbitals of Al are plotted against distance, r, from the atomic nucleus. The corresponding pseudo wavefunction is also plotted. Outside a given radius, the full and pseudo values are identical.

There is no unique way to construct a pseudopotential for a particular element. Several choices are possible. A pseudopotential is judged on the basis of its softness and transferability. It is called soft when few plane waves are needed. If the number of plane waves is very small, it is called an ultrasoft pseudopotential. A soft pseudopotential gets tailored for an element in a specific environment. A pseudopotential which can be used in any environment (solid, surface, cluster, etc), is called transferable. A good pseudopotential is that which is both ultrasoft and transferable.

The FP-LAPW Method

In this method, the wavefunction is described by plane waves for regions located some distance from the nucleus, as done in the pseudopotential method. The rapidly-varying function close to the nucleus is described by atomic-like functions. Thus space is divided in two regions, the muffin-tin and the interstitial region, as shown in figure 2.2. The Muffin-tin region belongs to a sphere of radius s around each nucleus, while the Interstitial region is the remaining space outside the sphere.

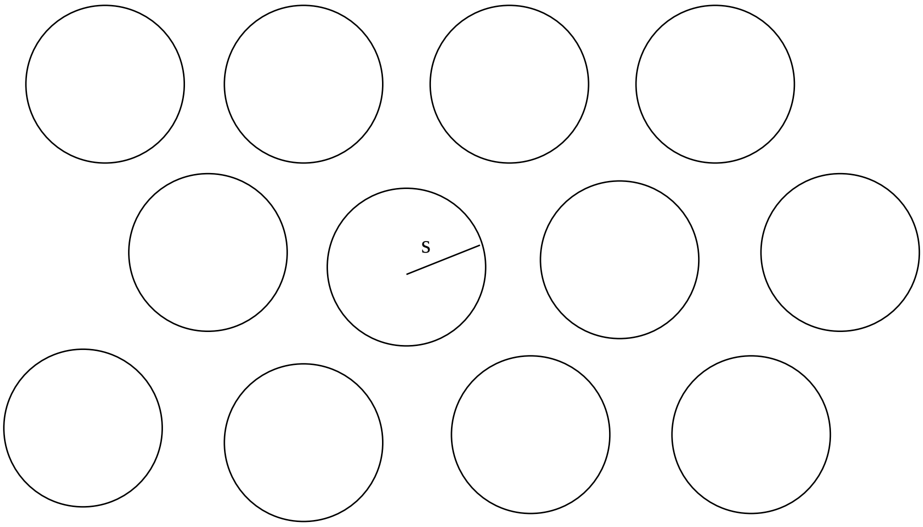

Figure 2.2: Division of space into muffin-tin and interstitial regions.

Hence, the augmented plane-wave basis function can be written as follows:

$$\phi_{\mathbf{K}}^{\mathbf{k}}\left(\mathbf{r}\right)=\frac{1}{\sqrt{V}}e^{i(\mathbf{k}+\mathbf{K}).\mathbf{r}} \qquad r>s \qquad (2.26)$$

$$\phi_{\mathbf{K}}^{\mathbf{k}}\left(\mathbf{r}\right)=\sum_{l,m}\left(A_{lm}^{\mathbf{k+K}}u_{l}\left(\mathbf{r},E_{0}\right)+B_{lm}^{\mathbf{k+K}}\dot{u}_{l}\left(\mathbf{r},E_{0}\right)\right)Y_{m}^{l}\left(\mathbf{r}\right)\qquad r<s \tag{2.27}$$

The coefficients $A_{lm}^{\mathbf{k+K}}$ and $B_{lm}^{\mathbf{k+K}}$ are obtained using the condition that the function and its slope in the muffin tin sphere matches with the plane wave of interstitial region at the sphere boundary surface. E_0 is the linearization energy. The $u_l\left(\mathbf{r},E_0\right)$ are solutions to the radial part of the Schrodinger equation if the atom is free (instead of being part of the solid. $Y_m^l\left(\mathbf{r}\right)$ are spherical harmonics.

2.2 Quantum Molecular Dynamics

Molecular dynamics (MD) simulation is a technique by which one generates the atomic trajectories of a system of N particles by numerical integration of Newton's equation of motion, for a specific inter-atomic potential, with certain initial condition (IC) and boundary condition (BC). Newton's equations of motion for a set of nuclei positioned at $\mathbf{R_I}$ are

$$M_I\ddot{\mathbf{R}}_I=\mathbf{F_I}\left(\mathbf{R}_I\right) \tag{2.28}$$

The forces on the nuclei have two contributions- direct forces between the nuclei and the force due to electrons. In classical molecular dynamics, this has been done by effective empirical potentials such as Lennard-Jones potential.

In quantum molecular dynamics the forces on the nuclei are directly derived from the electrons using electronic structure calculations [25]. No empirical parameters are required in QMD. In density functional theory the total energy of the system of electrons $E_{el}\left[\psi\right]$ is determined by solving the Kohn-Sham equation. The total energy of the system of ions and electrons can be given by

$$E\left[\psi,\mathbf{R}_I\right]=E_{el}\left[\psi\right]+E_{II}\left[\mathbf{R}_I\right] \tag{2.29}$$

Here, $E_{II}\left[\mathbf{R}_I\right]$ is the ion-ion interaction. Forces can be calculated by using Hellmann-Feynman theorem

$$\mathbf{F}_I=-\frac{\partial E}{\partial\mathbf{R}_I}=-\langle\psi|\frac{\partial\hat{H}}{\partial\mathbf{R}_I}|\psi\rangle-\langle\frac{\partial\psi}{\partial\mathbf{R}_I}|\hat{H}|\psi\rangle-|\psi|\hat{H}|\frac{\partial\psi}{\partial\mathbf{R}_I}-\frac{\partial E_{II}}{\partial\mathbf{R}_I} \tag{2.30}$$

2.2.1 Verlet Algorithm

Eq 2.28 is solved by numerical methods using discrete time steps based upon discrete equations such as the Verlet algorithm. This algorithm is a combination of two Taylor expansions, combined as follows. First Taylor series for position from time t forward to $t+\Delta t$

$$x\left(t+\Delta t\right)=x(t)+\frac{dx(t)}{dt}\Delta t+\frac{1}{2}\frac{d^2x(t)}{dt^2}\Delta t^2+\frac{1}{3!}\frac{d^3x(t)}{dt^3}\Delta t^3+O(\Delta t^4) \tag{2.31}$$

Second Taylor series for position from time t backward to time $t-\Delta t$

$$x\left(t+\Delta t\right)=x(t)-\frac{dx(t)}{dt}\Delta t+\frac{1}{2}\frac{d^2x(t)}{dt^2}\Delta t^2-\frac{1}{3!}\frac{d^3x(t)}{dt^3}\Delta t^3+O(\Delta t^4) \tag{2.32}$$

adding these two expansions eliminates all odd-order terms,leaving

$$x(t+\Delta t)=2x(t)-x(t-\Delta t)+\frac{d^2x}{dt^2}\Delta t^2+O(\Delta t^4) \tag{2.33}$$

This is Verlet's algorithm for positions. It has a truncation error which varies as $(\Delta t)^4$ hence it is of third order even though it does not contain third order derivatives. Position 2.33 does not involve any function of the velocities. To estimate velocities, various schemes are used, one being an estimate for the velocity at the half-step:

$$v(t+\frac{1}{2}\Delta t)=\frac{x(t+\Delta t)-x(t)}{\Delta t} \tag{2.34}$$

other scheme is the first-order central difference estimator

$$v(t)=\frac{x(t+\Delta t)-x(t-\Delta t)}{2\Delta t} \tag{2.35}$$

Verlet's algorithm is a two step method because it estimates $x(t+\Delta t)$ from the current position $x(t)$ and the previous position $x(t-\Delta t)$.

2.2.2 Velocity Verlet Algorithm

In this algorithm following equations are used for position

$$x\left(t+\Delta t\right)=x(t)+v(t)\Delta t+\frac{1}{2}a\Delta t^2+\text{.........} \tag{2.36}$$

acceleration a is calculated from the force and is used in velocity calculation

$$v\left(t+\Delta t\right)=v(t)+\frac{1}{2}[a(t)+a(t+\Delta t)]\Delta t \tag{2.37}$$

Since we can have $x\left(t+\Delta t\right)$ and $v\left(t+\Delta t\right)$ simultaneously, it is popular.

2.2.3 Ensembles

An ensemble is a collection of all possible systems which have different microscopic states but have an identical macroscopic or thermodynamic state. There exist different ensembles with different characteristics

1. **Microcanonical ensemble (NVE)** In the microcanonical, or NVE ensemble, the system is isolated from changes in moles (N), volume (V) and energy (E). It corresponds to an adiabatic process with no heat exchange. A microcanonical molecular dynamics trajectory may be seen as an exchange of potential and kinetic energy, with total energy being conserved.

2. **Canonical ensemble (NVT)**: In the canonical ensemble, moles (N), volume (V) and temperature (T) are conserved. It is also sometimes called constant temperature molecular dynamics (CTMD). In NVT, the energy of endothermic and exothermic processes is exchanged with a thermostat.

   A variety of thermostat methods is available to add and remove energy from the boundaries of an MD system in a more or less realistic way, approximating the canonical ensemble. Popular techniques to control temperature include velocity rescaling, the Nosé-Hoover thermostat and the Berendsen thermostat.

3. **Isothermal-isobaric (NPT) ensemble** : In the isothermal isobaric ensemble, moles (N), pressure (P) and temperature (T) are conserved. In addition to a thermostat, a barostat is needed. It corresponds most closely to laboratory conditions with a flask open to ambient temperature and pressure.

2.2.4 Boundary Conditions

There are two major types of boundary conditions: isolated boundary condition (IBC) and periodic boundary condition (PBC). IBC is ideally suited for studying clusters and molecules, while PBC is suited for studying bulk liquids and solids. There could also be mixed boundary conditions. such as slab or wire configurations for which the system is assumed to be periodic in some directions but not in the others.

In IBC, the N-particle system is surrounded by vacuum; these particles interact among themselves, but are presumed to be so far away from everything else in the universe that no interactions with the outside occur except perhaps responding to some well-defined external forces. In PBC, one explicitly keeps track of the motion of N particles in the so-called supercell, but the supercell is surrounded by infinitely replicated, periodic images of itself. Therefore a particle may interact not only with particles in the same supercell but also with particles in adjacent image supercells 2.3. It is not necessary to store the coordinates of all images in a simulation (this would be an infinite number), just those of the particles in the central box. When a particle leaves the box by crossing a boundary, attention may be switched to the identical particle just entering from the opposite side.

2.2.5 Thermostat

In molecular dynamics, The instantaneous value of the temperature is related to the kinetic energy via the particles momenta as follows:

$$\sum_{i=1}^{N} \frac{|p_i|^2}{2m_i} = \frac{k_B T}{2} (3N - N_c) \tag{2.38}$$

where N_c is the number of constraints and so $3N - N_c = N_{df}$ is the total number of degrees of freedom. The average temperature $\langle T \rangle$ is identical to the macroscopic Temperature. The standard MD is performed in the microcanonical (NVE) ensemble. Unfortunately, the microcanonical ensemble does not correspond to the conditions under which most experiments are carried out. If one is interested in the behavior of the system at a specific temperature, a NVT simulation using a thermostat is required.

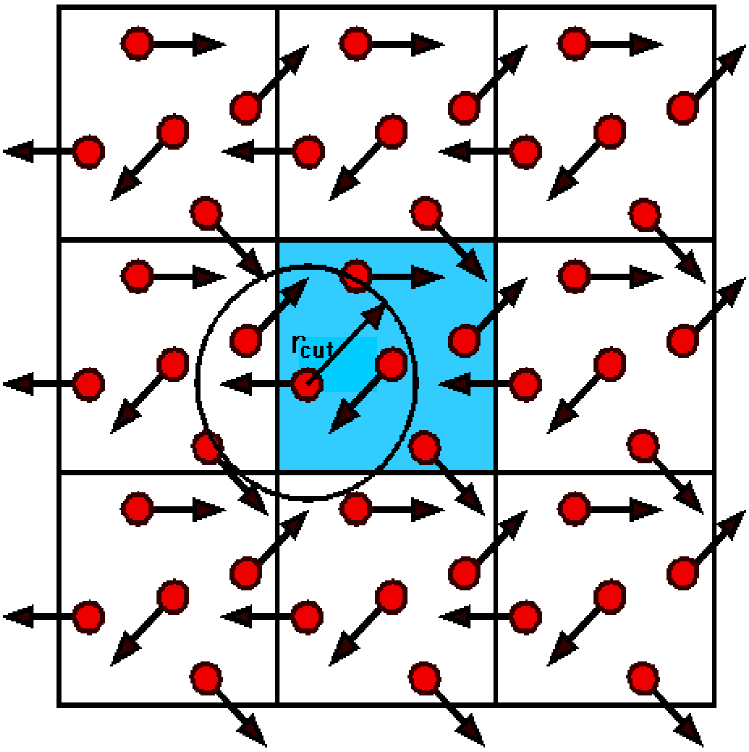

Figure 2.3: Illustration of periodic boundary condition (PBC). When using periodic boundary conditions, a particle which exits the system on the right, will reappear on the left.

An obvious way to alter the temperature of the system is velocity scaling. If the temperature at time t is $T(t)$ and the velocities are multiplied by a factor λ, then the associated temperature change can be calculated as

$$\Delta T = \frac{1}{2}\sum_{i=1}^{N} 2\frac{m_i\left(\lambda v_i\right)^2}{N_{df}k_B} - \frac{1}{2}\sum_{i=1}^{N} 2\frac{m_1 v_i^2}{N_{df}k_B} \tag{2.39}$$

$$\Delta T = \left(\lambda^2 - 1\right) T\left(t\right) \tag{2.40}$$

$$\lambda = \sqrt{T_0/T(t)} \tag{2.41}$$

The simplest way to control the temperature is thus to multiply the velocities at each time step by the factor $\lambda\sqrt{T_0/T(t)}$, where $T(t)$ is the current temperature as calculated from the kinetic energy and T_0 is the desired temperature. One problem with this approach is, that it does not allow fluctuations in temperature which are present in the canonical ensemble. To overcome this problem other thermostats such as Berendsen temperature coupling and Nose-Hoover temperature coupling thermostats can be used.

In this thesis, we have used the FP-LAPW method for our static calculations, and the pseudopotential method in the QMD calculations. The FP-LAPW calculations have been done using the Wien2K package [92] and QMD calculations have been performed using both ABINIT [93–95] and VASP [96, 97] codes.

3

First principles study of structural phase transformations in Al

Abstract: In this chapter we report results of ab-initio calculations for the zero-temperature isotherm for Al in compressed states. Zero-pressure properties, phase stability and phase coexistence have been studied for Al. Possible high pressure phases of Al are examined by comparing the total internal energies and enthalpies for three structures, viz., FCC, BCC and HCP. The energies are calculated using the density function formalism and the FP-LAPW method. Perdew-Burke-Ernzerhof 96 parametrization of the Generalized Gradient Approximation (GGA) is used for exchange and correlation. Zero pressure lattice constants and the bulk modulus have been calculated for three phases of Al, and show good agreement with published experimental results. Our results for the minimum energy c/a ratio for hcp match well with the experimental value. Coexistence of FCC & HCP phases for a wide range of pressures near phase transformation is indicated by volume-energy curves, in agreement with a recently reported powder X-ray diffraction experiment. The calculated lattice parameters at high pressures show good

agreement with reported experimental values. The computed transition pressure and volume for FCC-HCP phase transition is also in reasonable agreement with published experimental data. Finally, we have also calculated the FCC-BCC and BCC-HCP transition pressures and compared our results with reported theoretical results. These results show that the Perdew-Burke-Ernzerhof GGA, along with FP-LAPW, gives reasonably accurate results for aluminium over a large range of pressures.

3.1 Introduction

The behaviour of metals under high pressure at zero kelvin is very important for the determination of the equation of state. Such a study can be performed using accurate first principles calculations. Experimental data is also available up to some extent for the validation of the calculated results [61, 62, 67, 68, 75, 76, 102]. Such calculations can also predict pressure-induced phase transitions. Theoretical studies of such phase transitions in metals have been of special interest over the last three decades [44–51].

Of the simple metals, Aluminium is one of the simplest in many ways, being cubic closed packed in normal conditions and possessing ion cores occupied by electrons in the *s* and *p* orbitals. Al has thus been the subject of numerous experimental and theoretical studies. Ultra-high pressures of a few terapascals (TPa) have been achieved in experiments involving Al [67, 75]. Experiments have also been performed to investigate structural phase transitions in Al [61, 62].

The first theoretical study of phase transitions in Al was done by Friedli et. al [44] using a local pseudo-potential method. They showed by a series of arguments that the common face centered cubic (FCC) phase of Al appears to remain the stable phase even for pressures exceeding 3 Mbar (megabar). Moriarty and McMahan [46] studied phase stability in Al by two method - Generalized Pseudo-potential Technique (GPT) and the all-electron linear muffin-tin-orbital method (LMTO). Both methods predicted the same phase sequence for Al, viz., FCC-HCP-BCC, but the transition pressures were different. GPT predicted the FCC-HCP phase transition at 360 GPa and the HCP-BCC phase transition at 560 GPa, while LMTO predicted the transition pressures at 120 and 200 GPa respectively. GPT and LMTO predictions of the FCC-HCP transition pressure are much higher and lower, respectively, than the transition pressure recently obtained experimentally by Akahama [62] using the powder X-ray diffraction method.

Lam and Cohen [47] calculated total energies for three structures, viz., FCC, BCC and HCP, by using the density functional formalism and the ab initio self consistent pseudo-potential approach. They also found the same phase sequence. They predicted transition pressures of 200 and 400 GPa, respectively. However, since these calculations were based on calculated total energies for only four volumes, viz., 1.0 V_0, 0.8 V_0, 0.6 V_0 and 0.4 V_0, their precision is open to question. Here, V_0 is he atomic volume under standard conditions. Boettger and Trickey [48] calculated the energies and enthalpies of the FCC and BCC structures by using the linear combination of Gaussian type orbitals (LCGTO) technique. They compared energies and enthalpies of both structures and predicted that the FCC phase should be more stable for pressures below 3.28 ± 09 Mbar, while the BCC structure is more stable at higher pressures. In this calculation, they did not consider the HCP structure of Al.

Greene et al. [61] performed an experiment using a diamond-anvil-cell (DAC) to show that the FCC structure remains stable up to 219 GPa. In 1994, Boettger and

Trickey [49,50] performed high-precision, all-electron full potential calculations using the linear combination of Gaussian-type orbitals-fitting function (LCGTO-FF) technique, combined with a rough estimate for the impact of zero-point motion on the transition. They predicted that FCC-HCP-BCC transitions would occur at 205±20 and 565±60 GPa, respectively. They used the local density approximation (LDA) for exchange and correlation. Their results indicate that the DAC experiment [61] probably came very close to achieving the FCC-HCP phase transition. Very recently, the structural phase transition of Al was again investigated by a powder X-ray diffraction experiment [62]. This investigation was done up to 333 GPa and the FCC-HCP phase transition was observed at a reduced volume V/V_0 of 0.509, corresponding to a pressure of 217 GPa. This experiment also reported evidence of the coexistence of FCC and HCP phases over a wide range of pressures.

All the calculations reported so far have been done using either pseudo-potential methods or by using LDA in fullpotential methods. For a given electronic density distribution, the LDA replaces the true exchange-correlation at each point in space by the exchange-correlation energy of a homogeneous electronic gas of the same density [84]. In principle, the LDA is only valid for an electron gas of slowly varying density in space [103]. LDA has several limitations in calculating properties of bulk solids, where it tends to overestimate the magnitude of the total energy and bulk moduli and underestimate equilibrium lattice constants [87,104,105]. To improve on these limitations, attempts have been made to focus on generalized gradient approximations (GGA), in which the exchange-correlation functional incorporates terms containing density gradients [88–90]. Lattice constants, bulk moduli and energies of bulk solids are found to improve when GGA is used [103]. Recent calculations [104] indicate that the GGA functional proposed by Perdew-Burke-

Ernzerhof [88] is promising.

The only investigation using GGA, so far, was done by G V Sinko and N A Smirnov [51]. This investigation was done by FP-LMTO method. They have taken zero point vibration effect also into account to predict the FCC-HCP phase transition. They report FCC-HCP transition at 170 GPa for rigid lattice and 220 GPa after including the effect of the zero point vibrations. In the present work we have also used GGA [88], with a different technique for energy calculation, FP-LAPW method. There are two major shortcomings in the foregoing studies. Firstly, none of the studies have calculated lattice parameters at higher pressures theoretically and secondly, there is a lack of theoretical understanding for the coexistence of FCC and HCP phases over a wide range of pressures. Hence there is a need for performing more accurate DFT calculations using the full-potential (FP) linearized augmented plane wave (LAPW) method, using GGA. This forms the subject of the present investigation.

3.2 Computational Details

We have used the WIEN2k code [26, 92] to calculate the total energies of the FCC, BCC and HCP structures of Al. This code performs electronic structure calculations of solids using the FP-LAPW method. This method is amongst the most accurate methods for performing first principles calculations for crystals and is used widely for the studies of structural properties of crystalline materials [104, 106–110]. The exchange correlation potential within LDA is calculated using the scheme of Perdew-Wang [91], while the scheme of Perdew-Burke-Ernzerhof [88] is used within GGA.

Details of the LAPW method are given elsewhere [26, 92]; here we focus on the aspects relevant to the present calculations. These calculations have been done using a constant muffin-tin radius R_{mt} of 1.7 a.u. In the WIEN2k code, it is very important to select a good basis set and kmesh size for getting accurate results. We start by taking a low value of $R_{mt}K_{max} = 7.0$. For purposes of determining a suitable k-mesh size, we then calculate the total energy as a function of the size of the k-mesh., increasing the size by 1000 at each step. We find that 10000 k-points are sufficient. Having determined a good k-mesh, we now vary $R_{mt}K_{max}$ from 7 to 12, and find that 9.0 is a good choice. Lmax is taken as 10 throughout the calculations. We have selected an energy cut-off of 6.0 Ry to separate the core from the valence states. The convergence criterion for energy was taken as 10^{-4} Ry.

3.3 Results and discussion

3.3.1 Total energy as a function of volume

Total energies were calculated for FCC, HCP and BCC phases of Al as a function of volume. In the case of HCP, the calculation has been repeated for different values of the c/a ratio. The volume was varied by using the volume optimization module of WIEN2k. It was found that a c/a ratio of 1.614 yields the lowest energy value for HCP Al. The data obtained by the above calculations were used in obtaining zero-pressure properties of Al, as well as its crystallographic phase stability at high pressures. Sample data points from the above calculation, using GGA, are given in table 3.1.

Table 3.1: Atomic volume ($bohr^3$) and calculated total energies E (Ry/atom) for the FCC, HCP and BCC structures of Al

Volume	E_{FCC}	E_{HCP}	E_{BCC}
119.53	0.6437	0.6418	0.6376
115.02	-0.6449	-0.6425	-0.6381
110.51	-0.6452	-0.6426	-0.6379
106.0	-0.6445	-0.6416	-0.6366
101.49	-0.6426	-0.6396	-0.6341
95.85	-0.6379	-0.6347	-0.6288
90.21	-0.6299	-0.6266	-0.6204
78.93	-0.5994	-0.5963	-0.5898
67.66	-0.5368	-0.5350	-0.5291
56.38	-0.4140	-0.4151	-0.4113
50.74	-0.3132	-0.3165	-0.3148
45.10	-0.1690	-0.1757	-0.1771
42.29	-0.0740	-0.0830	-0.0864
39.47	0.0416	0.0299	0.0238
36.65	0.1836	0.1684	0.1590
33.83	0.3595	0.3402	0.3265

3.3.2 Lattice constants and bulk modulus at normal pressure

It is first necessary to determine which option for the exchange-correlation functional is the most suitable for our purposes. This can be done by a comparison of certain zero-pressure properties, viz., the lattice constants and the bulk modulus. The ground-state properties of the three phases of Al were obtained using the calculations of the total energy (E) as a function of volume (V) at lower pressures. A total of nine equally spaced data points were generated over the volume range from 101.49 to 119.53 $bohr^3$, and the data were fitted to the Murnaghan equation of state [16].

$$E_V = E_0 - \frac{B_0 V_0}{B' - 1} + \frac{B_0 V}{B'} \left[\frac{(V_0/V)^{B'}}{B' - 1} + 1 \right] \tag{3.1}$$

This fit then yielded the zero-pressure equilibrium lattice constants *(a, b, c)*, the bulk modulus (B_0) and the pressure derivative of the bulk modulus (B_0). These results are given in table 3.2 for the FCC, HCP and BCC structures of Al. Results are shown using both LDA and GGA.

Table 3.2: Calculated zero-pressure equilibrium lattice constants, bulk modulus and pressure derivative of bulk modulus, for the FCC, HCP and BCC phases of Al

	GGA			LDA		
	FCC	HCP	BCC	FCC	HCP	BCC
a_0	7.63	5.43	6.10	7.52	5.35	6.02
B_0	78.36	75.02	69.05	84.02	80.13	74.39
$B^{'}$	4.48	4.08	4.33	4.98	4.49	4.07

Table 3.3: The lattice constant a_0 (Bohr) and bulk modulus B_0 (GPa) for the FCC structure of Al

Reference	Potential	a_0	B_0	
Experiment (Ref. [17])			7.62	77
Present GGA	PBE96	7.63	78.3	
Present LDA	PW92	7.52	84.0	
Reported using LDA:				
Ref. [12]	HL	7.60	79.7	
Ref. [33]	HL	7.60	80	
Ref. [34]	W	7.58	71.5	
Ref. [10]	KSG	7.65	96.8	
Ref. [35]	PZ	7.43	87.6	
Ref. [36]	HL	7.54	82.2	
Ref. [37]	HL	7.54	84	
Ref. [17]	PZ	7.52	83.9	
Ref. [38]	PZ	7.48	87	
Reported using GGA:				
Ref. [35]	PW91	8.03	61.1	
Ref. [39]	PW91	7.62	79.3	
Ref. [37]	PW91	7.65	74	
Ref. [17]	PW91	7.74	72.6	
Ref. [38]	PW 86	7.63	79	
Ref. [37]	EV	7.91	55	
Ref. [38]	BP	7.64	79	

Table 3.3 compares the zero-pressure static-lattice properties obtained here,

for the FCC structure of Al, with results from a wide variety of calculations using various approximations for exchange and correlation. Table 3.3 also gives the experimental values of lattice constant and bulk modulus taken from [103]. Comparison of LDA and GGA results with the experimental values of bulk modulus and lattice constant reveals that LDA generally underestimates the lattice constant and overestimates the bulk modulus. PW91 parametrized GGA gives good results in the calculations of [116], but gives inaccurate results in other calculations showing inconsistency. Similarly, Becke-Perdew functional (BP) was used to compute the lattice constant, bulk modulus, and cohesive energy for various metals in [113] and no consistent improvement over the predictions of local density approximation was found. In our calculation, we have used PBE-GGA, which incorporates several improvements over PW91. These include an accurate description of the linear response of the uniform electron gas, correct behavior under uniform scaling, and a smoother potential [88].

Table 3.3 shows that this version of GGA gives results that are in better agreement with experimental values, with only 0.13 % error in the lattice constant and 1.7 % error in the bulk modulus. Given the higher accuracy yielded by PBE-GGA, all subsequent calculations have been performed with this GGA.

3.3.3 c/a ratio optimization for HCP structure

We are interested in the FCC-HCP transition and the HCP-BCC transition at high pressures. For FCC and BCC, the only adjustable parameter is a. For HCP, however, the ratio c/a must also be specified. Hence it is first necessary to determine the c/a ratio that minimizes system energy at a given volume V/V_0.

To this end, we have calculated the total energy for HCP as a function of the c/a ratio for several densities. The c/a ratio was varied by $\pm 10\%$, in steps of 2%,

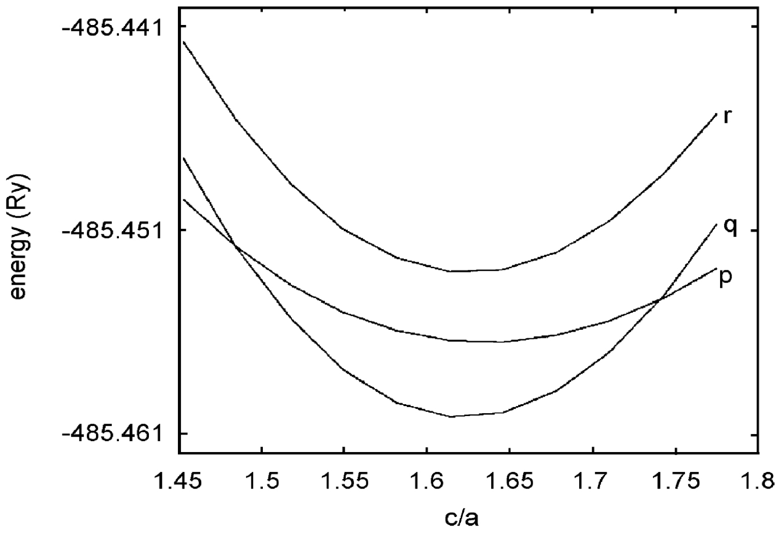

Figure 3.1: Energy as a function of c/a ratio for HCP structure at three densities; curves p, q and r correspond to V/V_0 0.71, 0.53 and 0.48, respectively. To allow plotting in the same figure, curve p has been shifted up by 0.14 Ry and curve r down by 0.09 Ry.

around the experimental value of 1.6139 [62]. This calculation was repeated for several values of V/V_0 spanning our range of interest. We have found that for the densities near to normal density the energy is minimum for the c/a ratio, deviated by 2% of the assumed value. And near the FCC-HCP transition and at higher densities the energy was minimum for the assumed value of c/a ratio. The results for three representative values of V/V_0 are shown in Fig. 3.1, where curves p q and r correspond to energy variation with respect to c/a ratio at volume ratios 0.71, 0.53 and 0.48, respectively. Curve p shows minimum at the c/a ratio deviated by 2% from c/a 1.6139, while q and r show minimum at c/a 1.6139.

All subsequent calculations have used this value of the c/a ratio.

3.3.4 Lattice constants at higher pressure

In order to estimate the accuracy of our calculations at high pressures, we have also calculated the lattice constants at higher pressures and compared the results with those obtained in X-ray powder diffraction experiments [62] recently. Fig. 3.2 shows the lattice constants for FCC and HCP structures as a function of pressure. Results of our calculations show a good agreement with experimental values [62]. The percentage errors are up to .5%, in the calculated results for a_{FCC} and a_{HCP}, and up to .4% in the calculated results for c_{HCP}. Errors do not show any definite trend with the pressure.

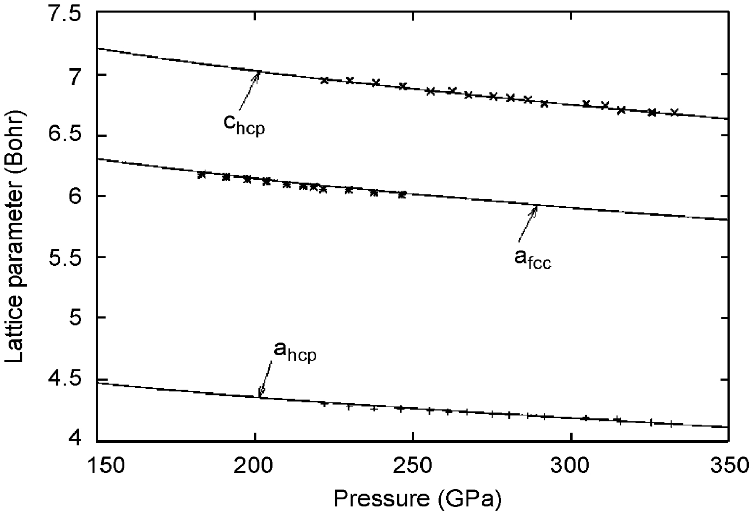

Figure 3.2: The pressure dependence of the lattice constants a_{HCP}, a_{FCC} and c_{HCP}. The solid line shows our calculations while points show experimental values from [62].

3.3.5 Phase transformations under high pressure

We have compared the total energies and enthalpies of three structures of Al to determine the phase stability at higher pressures. Now, there are two commonly used methods for estimating phase stability. The first method compares the E values, at a given specific volume, for different phases, the phase with the lowest energy being regarded as the most stable. The second method compares the Gibbs free energy, G, as a function of pressure. Now, the Gibbs free energy becomes identical with the enthalpy at zero temperature. Hence we need only compare $E+PV$ as a function of pressure, the pressure being computed numerically from the $E(V)$ data. The results, using the two techniques mentioned above, are discussed in Sections 3.3.5 and 3.3.5.

Volume vs. total energy

The conventional method for obtaining the quantities such as energy and pressure at any volume, from the computed E(V) data, is to use a best-fit function, such as the Murnaghan equation of state [16]. However, we have found that this does not work well at high compressions. We have found it better to fit E(V) data over the range $V/V_0 = 0.3$-0.7, by best-fit cubic splines [118]. Forty data points were fitted over this range. The pressure was then calculated from the negative of the gradient of the energy-volume curve. The differences (Δ) between the energies of FCC & HCP, FCC & BCC, and HCP & BCC were calculated and plotted as a function of the volume to determine the transition volume. Note that this difference was calculated using the best-fit splines.

Fig. 3.3 shows variations of $\Delta_{\mathrm{FCC-HCP}}$, $\Delta_{\mathrm{FCC-BCC}}$ and $\Delta_{\mathrm{HCP-BCC}}$ with V/V_0 as curves p, q and r respectively. Curve p crosses $\Delta = 0$ at $V/V_0 = 0.53$, indicating an FCC-HCP phase transition at this point. Experimentally, however, this transition has been found to lie at 0.509 by Akahama et. al [62]. The reason for this difference could be that $\Delta_{\mathrm{FCC-HCP}}$ is negligibly small (of the order of 10^{-4} Ry over the range $V/V_0 = 0.51 - 0.53$). It becomes significant ~ 0.9 mRy at $V/V_0 = 0.5089$ and becomes 1 mRy when V/V_0 reaches 0.50. Such a small difference between the

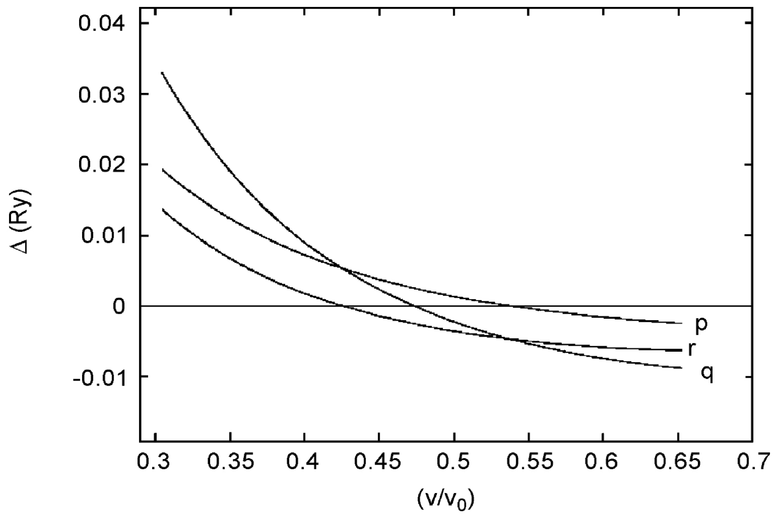

Figure 3.3: The difference in energy between two structures of Al, as a function of normalized volume: $p = E_{\mathrm{HCP}} - E_{\mathrm{HCP}}$, $q = E_{\mathrm{FCC}} - E_{\mathrm{BCC}}$, $r = E_{\mathrm{HCP}} - E_{\mathrm{BCC}}$.

energies of FCC and HCP structures around the phase transition point could be the reason why this phase transition could not be detected in the DAC experiment [61]. Note that we have ignored the effect of zero point vibrations [51], this may also be a reason for the difference in our results and the experimental results.

Let us now consider the HCP to BCC phase transition. The difference in energies between these two structures, shown as curve r ($\Delta_{\mathrm{HCP-BCC}}$) crosses $\Delta = 0$ at $V/V_0 = 0.426$ but the difference becomes significant ($\sim$ 1.0 mRy) at $V/V_0 = 0.408$. Hence we expect that this transition should be experimentally observed only around $V/V_0 = 0.41$.

In the same way, curve q shows that the FCC-BCC transition is expected to occur over the V/V_0 range 0.47-0.46.

Pressure vs. enthalpy

For determining the most stable structure at finite pressure we have also compared the Gibbs free energies of the three structure; the structure with the lowest Gibbs free energy is the most stable. Fig. 3.4 shows differences between the Gibbs free energies for different phases as functions of pressure (P). The pressure was calculated from the negative of the gradient of the energy-volume curve. Also shown are the results from Ref. [51].

The line p, representing the difference between the free energies of FCC and HCP structures, crosses zero at 178 GPa, showing FCC-HCP transition occurring here. However, the reported experimental value is 217 ± 10 GPa. We have not included the zero point vibrations effect in our calculations. This could be a reason for the difference between the calculated transition pressure and the reported experimental transition pressure [51]. Also, our calculations have been done for zero Kelvin while the experiment [62] was performed at 297 K, However thermal contribution of pressure is very small at room temperature [50] and therefore it will not make any considerable difference in predicting the phase stability.

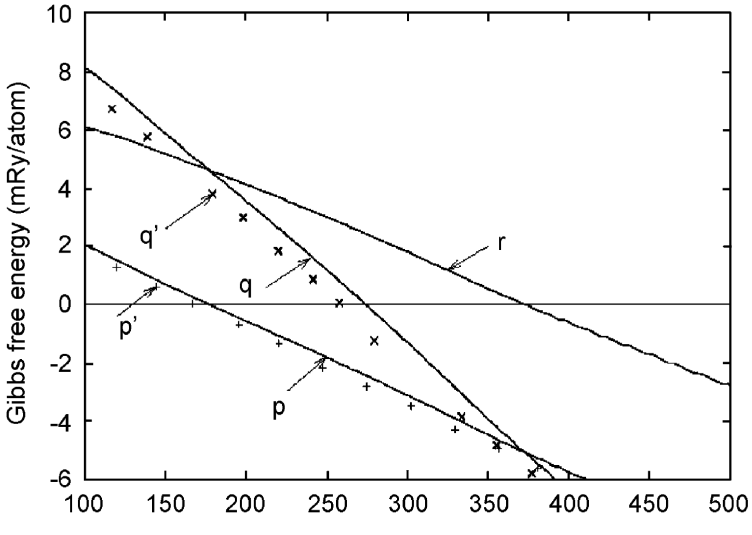

Figure 3.4: The difference in Gibbs free energy between two structures of Al, as a function of normalized volume: $p = G_{\mathrm{HCP}} - G_{\mathrm{FCC}}$, $q = G_{\mathrm{BCC}} - E_{\mathrm{FCC}}$, $r = E_{\mathrm{BCC}} - E_{\mathrm{HCP}}$. p' and q' represent the corresponding values from [51].

Akahama has also reported the coexistence of HCP and FCC phases, the transition starting at a pressure of 217 ± 10 GPa, with the two phases coexisting up to a pressure of 265 GPa. This can be understood in the light of our calculations, which indicate only small differences between the energies of FCC and HCP structures over this pressure range (~ 2.0 mRy at 265 GPa).

Let us now consider the HCP to BCC phase transition. The difference in free energies between these two structures, shown as curve r, crosses zero at 376 GPa, Experimental data for this transition is not available in literature, hence our results can only be compared with other computations. Our value matches reasonably well with the 400 GPa value reported in [47]. However, it does not match with the calculations of [46], where the GPT and LMTO calculations predict 560 and 200 GPa, respectively, nor the value of 565 ± 60 GPa predicted by [49, 50] using a LCGTO-FF calculation.

Again as in FCC-HCP case, the free energy difference is very small over a large range of pressure, ~ 1.0 mRy only up to the pressure of 425 GPa. So we expect that experimentally HCP-BCC transition would be observed over the pressure range 376-425 GPa and both phases would coexist in this pressure range.

The line q in Fig. 3.4 indicates FCC-BCC transition at 275 GPa, this is in reasonable agreement with the value of 300 GPa calculated by [47] and 340 ± 15 GPa from Refs. [49, 50].

3.3.6 FCC-HCP phase co-existence in terms of density of states

Structural phase transition up to 333 GPa in Al has been investigated by a powder X-ray diffraction experiment [62]. FCC - HCP phase transition was observed at a reduced volume V/V_0 of 0.509. In this work, the FCC-HCP transition pressure was reported to be 217 ± 10 GPa. This experiment also reported evidence of the coexistence of FCC and HCP phases over a wide range of pressures near the transition. Before this experiment, Greene et al. [61] had performed an experiment using a diamond-anvil-cell to show that the FCC structure remains stable up to 219 GPa and they did not find any structural transformation up to this pressure. This could be because of the coexistence of the fcc and hcp structures over a wide range of the pressures near transition, as reported in Ref. [62]. In this section, we attempt to understand phase coexistence of fcc and hcp phases in Al in terms of the density of states (DOS).

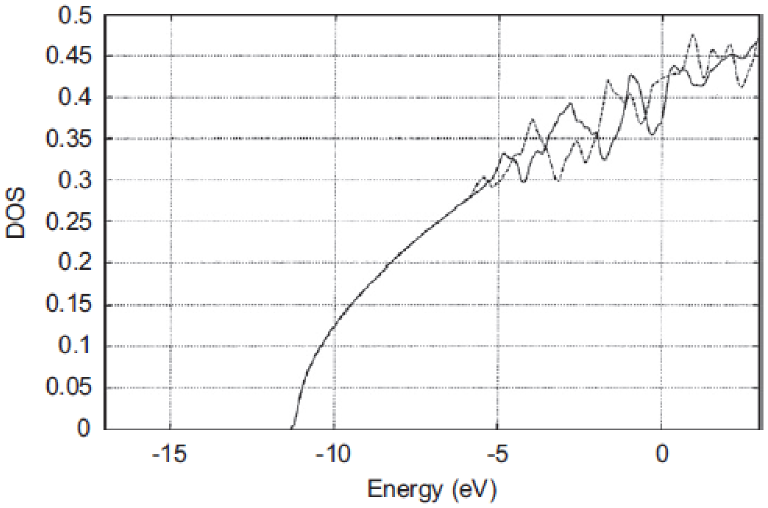

Figure 3.5: Density of states (states/eV/atom) for aluminum at normal volume V_0. The solid and dotted lines represent FCC and HCP. The Fermi level is set at 0.0 eV.

Fig. 3.5 shows the DOS of fcc and hcp phases at the normal volume V_0. We see that the total DOS for the FCC and HCP phases at the Fermi energy is 0.37 and 0.42 states/eV/atom Hence the difference in DOS at this volume is 0.05 eV^{-1} per atom, indicating that the fcc phase is more stable; similar arguments are given for

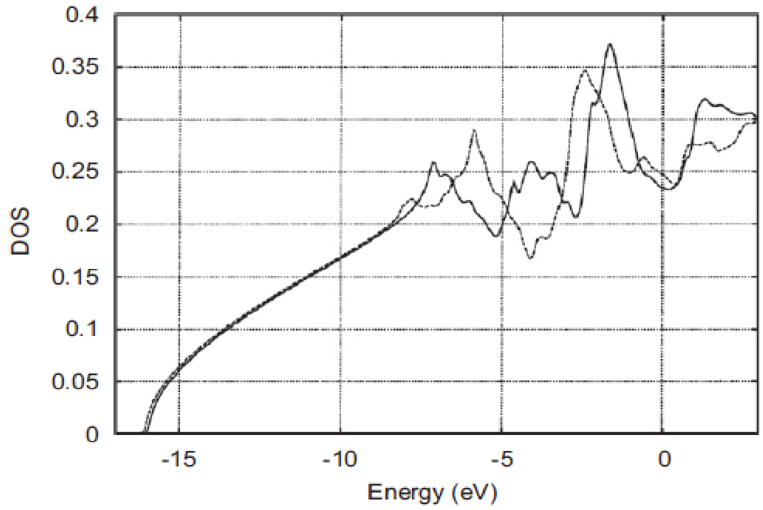

Figure 3.6: Density of states (states/eV/atom) for aluminum at volume $0.53V_0$. The solid and dotted lines represent FCC and HCP. The Fermi level is set at 0.0 eV.

the stability of FCC structure in gold at normal pressure and of hcp structure at high pressures for gold [98]. Fig. 3.6 shows the same plots at a relative volume of 0.53. Here, the difference in DOS comes down to 0.01 eV^{-1} per atom, indicating that the phases are closer in terms of stability. Furthermore, at normal volume V_0, the FCC DOS shows a dip near the Fermi level, while the HCP DOS does not exhibit this feature. This further reinforces the claim that the FCC phase is more stable at V_0 [98]. At $0.53V_0$, however, both structures exhibit this dip, as shown in Fig. 3.6, indicating that the two phases are likely to coexist at this volume.

3.4 Conclusion

We have performed first-principles calculations with the Wien2k code, using the FP-LAPW method with the PBE96 GGA. We have obtained zero pressure lattice constants and bulk modulus that match well with experimental values. Our results for the minimum energy c/a ratio for HCP also match well with the experimental value. From our volume vs. energy curve, it is clear that FCC and HCP phases coexist over a wide range of pressures. This is also in agreement with a recent powder X-ray diffraction experiment. The calculated lattice parameters at high pressures also match with reported experimental values. The computed transition pressure and volume for FCC-HCP phase transition is also in reasonable agreement with experiment. Finally, our calculations indicate that FCC-BCC and HCP-BCC phase transitions should occur over pressure ranges of 386-437 and 279-301 GPa, respectively. The density of states (DOS) of FCC and HCP structures of Al has been calculated for normal and high pressures. It has been found that the DOS of both structures, near the Fermi level, is similar over a range of compressed volumes close to the FCC-HCP transition volume ($V/V_0 \sim 0.53$). This similarity is the reason for the reported coexistence of FCC-HCP phases over a wide range of pressures near the FCC-HCP phase transition.

4

Ab-initio calculations of EOS and conductivity of Al in expanded states, and comparison with Quotidian EOS results

Abstract: In the last chapter, we determined the zero temperature isotherm of Al in compressed states using the FP-LAPW method. In this chapter, we perform ab-initio molecular dynamics (AIMD) simulations to calculate the EOS of Al in the rarefied region, i.e., for densities below normal. These results are compared with those from the Quotidian equation of state (QEOS) model, which is used for generating EOS tables over large ranges of density and temperature.

The EOS data obtained by QEOS has been used to calculate $U_s - U_p$ and $P - V$ hugoniots. The calculated hugoniots show good agreement with published experimental results. The cold curve generated by the QEOS model has been compared with FP-LAPW results for compressed states and good agreement has been found. The QEOS data has also been compared with AIMD simulation results for

expanded states – agreement is not good. These comparisons confirm that QEOS results are accurate for compressed states and less accurate for expanded states of Al for T≃10,000-20000 K. AIMD-based calculations of the electrical conductivity of Al in rarefied states are also presented.

4.1 Introduction

In Chapter 1, we introduced the three-term EOS:

$$E_{TOT}\left(\eta,T\right)=E_{C}\left(\eta\right)+E_{IT}\left(\eta,T\right)+E_{ET}\left(\eta,T\right) \tag{4.1}$$

$$P_{TOT}\left(\eta,T\right)=P_{C}\left(\eta\right)+P_{IT}\left(\eta,T\right)+P_{ET}\left(\eta,T\right) \qquad \eta=\rho/\rho_0 \tag{4.2}$$

In the Quotidian EOS (QEOS) algorithm, the Thomas-Fermi (TF) model is used for computing both contributions of electrons, viz., the cold as well as electron thermal contributions [10]. The Cowan model is used for the ion thermal contribution [10, 42]. The TF model does not consider bound states of electrons, nor does it include an accurate quantum-mechanical model of solids. Hence it predicts a few megabar pressure for a cold solid where the actual pressure should be zero.

In order to obtain an approximately correct EOS in this region, an empirical bonding correction must be applied. This correction is applied in such a way that pressure and bulk modulus are made to match experimental values under normal conditions. At the same time, it is ensured that the correction term has little effect at densities far from normal. Hence, in the QEOS model, the total energy and pressure are given by the following equations [10, 42]:

$$E_{TOT}(\eta, T) = E_B(\eta) + E_{IT}(\eta, T) + E_E(\eta, T) \tag{4.3}$$

$$P_{TOT}(\eta, T) = P_B(\eta) + P_{IT}(\eta, T) + P_E(\eta, T) \tag{4.4}$$

where E_B is the bonding correction term and E_E is the electron contribution to EOS which is calculated by using the Thomas-Fermi model.

4.2 Computational Details

We have used More's methodology for performing QEOS calculations to generate EOS data of Al. For comparing QEOS data at T=0 and compressed states, we have performed first principles calculations using the FP-LAPW method [92]. For comparison with QEOS data in expanded states (densities below normal), we have performed Ab-Initio Molecular Dynamics (AIMD) simulations. The details of QEOS, FP-LAPW and AIMD calculations are given below.

4.2.1 QEOS code using More's methodology

We have developed a quotidian equation of state (QEOS) code, based on the methodology of More, for generating EOS tables, specific heat and sound speed over a wide range of temperatures and densities, including compressed as well as expanded states. This yields the pressure, energy, entropy and free energy, taking into account density-dependent melting temperature, Debye temperature and Gruneisen parameter for any material. In this model cold contribution is calculated by adding bonding correction to the TF contribution at zero temperature. In fact TF model does not assume shell structure of electrons and assumes them as a gas of free electrons. This assumption is correct at very high temperature but gives a few megabar pressure at standard conditions which is not correct since the pressure should be zero at standard condition due to chemical bonding. Hence to get a correct zero temperature isotherm a bonding correction term is added in the TF contribution which is of the form [120]

$$E_b = E_0 \left[1 - exp\ b \left\{ 1 - \left(\frac{\rho_0}{\rho} \right)^{1/3} \right\} \right] \tag{4.5}$$

The bonding correction to the pressure will be

$$p_b = \rho^2 (\partial E_b / \partial \rho) \tag{4.6}$$

hence, total pressure cold pressure will be $p_{TOT} = p_{TF} + p_b$. Bulk modulud can be calculated by

$$B = \rho \left(\frac{\partial p_{TOT}}{\partial \rho} \right)_{\rho_0} \tag{4.7}$$

In order to determone E_0 and b, the requirements that the bulk modulus should be equal to the experimental bulk modulus and the total pressure should be zero at normal density are used.

The ion-thermal term is calculated using the Cowan model as described in [10].

Following Cowan model [10], energy and pressure of the ions in fluid phase can be expressed as

$$E_{\mathrm{IT}} (\rho,\ T) = \frac{3kT}{2AM_{\mathrm{P}}} \left(1 + w^{\frac{1}{3}} \right) \tag{4.8}$$

$$P_{\mathrm{IT}} (\rho,\ T) = \frac{\rho kT}{AM_{\mathrm{P}}} \left(1 + \gamma_{\mathrm{F}} w^{\frac{1}{3}} \right) \tag{4.9}$$

$w = T_{\mathrm{m}} (\rho) / T$, T_{m} is the melting temperature, γ_{F} is the fluid Grüneisen parameter. These equations reduce to ideal gas equation in the limit $(w \to 0)$, and reduce to solid phase forms at $w = 1$ if

$$\gamma_{\mathrm{F}} = 3\gamma_{\mathrm{s}} - 1 \tag{4.10}$$

where γ_{s} is the solid phase Grüneisen parameter, this parameter can be calculated using the formulas given in [42].

4.2.2 Full Potential Linearized Plane Wave (FPLAPW) Calculations

FP-LAPW results for the zero-temperature isotherm of Al have been taken from chapter 1. The cold-curve calculated for FCC structure has been used.

4.2.3 Ab-Initio Molecular Dynamics (AIMD) Simulations

We used the ABINIT code [93, 94] for performing AIMD simulations, in isokinetic ensemble. The simulations are first run until equilibration is achieved, i.e., until the variations in pressure stabilize to an oscillatory pattern, without any long-term trend. Following equilibration, the pressure and energy are calculated by averaging over the next 500-1000 time steps of 1 femtosecond (fs) each. The exchange correlation interactions of electrons are treated in generalized gradient approximation (GGA), using PBE parametrization [88]. Ion-electron interactions are described by the pseudo-potential generated by Troullier and Martins method [99]. All calculations have been done at the Γ point, i.e., with number of k-points taken as one.

The atomic configurations, generated by the AIMD simulation in the calculation of EOS, are used for calculating frequency-dependent electrical conductivity $\sigma(\omega)$ of Al. This is done using the Kubo-Greenwood formula as implemented in the ABINIT code. Quantities like Fermi Dirac occupation for each band and each k point, weight of each k point, electronic eigenstates and eigenvalues for each electronic state, and the derivative of the Hamiltonian with respect to the wave vector of the three directions, are required as input for the Kubo-Greenwood formula. These quantities are also calculated by the ABINIT code. For selected statistically-independent atomic configurations of 32 atoms, a self-consistent ground state calculation is performed with the ABINIT code to get the detailed electronic structure. For conductivity calculations, we found that four k points are necessary for better convergence. We ensured that there were always some unoccupied levels for better convergence of all runs.

4.3 Results and Discussion

4.3.1 QEOS-Results

In figure 4.1, we have shown the TF as well as QEOS pressures as functions of density at T=200 K. The TF pressure is approximately 1 megabar at normal density. The binding correction term makes pressure zero at normal density. The binding correction has little effect at higher densities, hence QEOS and TF models give similar representation of electron contribution at very high density. TF model is accurate in high density limit. In order to get zero pressure at standard conditions, the cold energy should have a minimum at normal density. However, as shown in figure 4.2, the TF cold energy does not exhibit a minimum at normal conditions. The binding correction removes this discrepancy.

The EOS generated using the QEOS model is combined with the three hugoniot equations viz., $\rho_0 U_s = \rho_1 (U_s - U_p)$, $P_1 - P_0 = \rho_0 U_s U_p$ and $E_1 - E_0 = \frac{1}{2}(P_1 + P_0)(V_0 - V_1)$ to get the $P - V$ and $U_s - U_p$ hugoniots [9]. In these equations, ρ, E, P and V have the same meaning as in Equations 4.1 and 4.2 and U_s

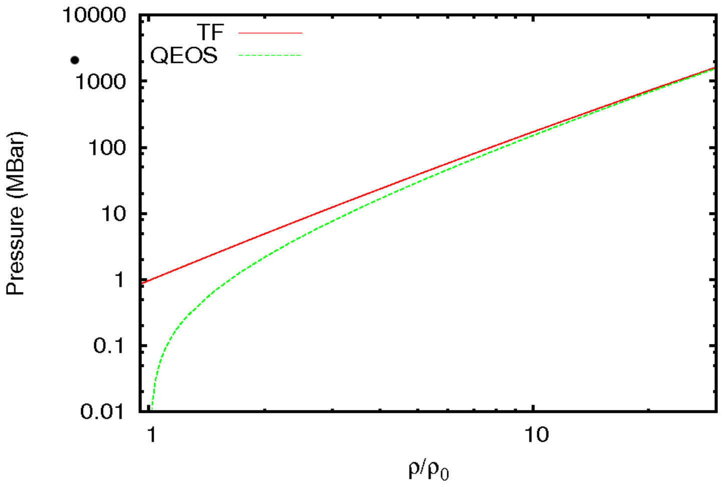

Figure 4.1: TF and QEOS cold pressures as functions of density at T=200 K.

and U_p are shock and particle velocities respectively. The suffixes 1 and 0 represent the quantities in the shocked and unshocked regions. The calculated $U_s - U_p$ and $P - V$ hugoniots are plotted in figures 4.3 and 4.4, respectively. For comparison, experimental shock compression data [30,41,102] are also shown. Good agreement with the experimental hugoniot can be seen.

4.3.2 Comparison of QEOS results with ab-initio calculations

We next compare the cold curve generated by QEOS by first-principles calculations using the FP-LAPW method within the framework of density functional theory. For generating the cold curve using FP-LAPW method we have assumed Al to exist in the FCC structure at all pressures. In figure 4.5, we can see that there is a very good agreement between first principles results and QEOS results. QEOS calculates the cold curve by adding a semi-empirical bonding correction term to the zero-temperature cold curve obtained by the TF model. Although it is a crude

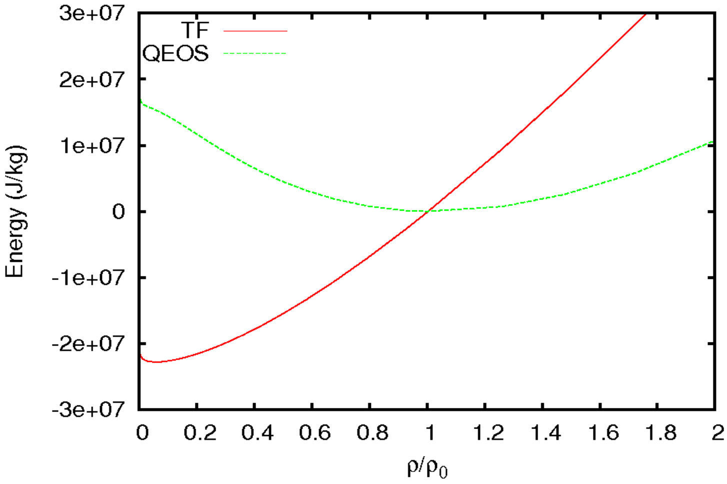

Figure 4.2: TF and QEOS cold energies as functions of density.

way of calculating the cold curve, it gives results as accurate as FPLAPW results, in which no experimental data is used as input and calculations are done purely using a quantum mechanical method.

These theoretical results match well with reported experimental data obtained by powder x-ray diffraction experiments [62]. The QEOS cold curve also agrees well with the cold-curve deduced from shock wave experiments [75, 77].

In figure 4.6, we have shown a comparison of QEOS results with AIMD simulation results for temperature = 10,000 K and expanded states. AIMD simulations are known to yield an accurate EOS in this regime, especially for $(T < 5eV)$ [53,56]. It can be seen that QEOS results do not show good agreement with the results of AIMD simulations. Hence, QEOS results are less accurate for expanded metals at low temperatures.

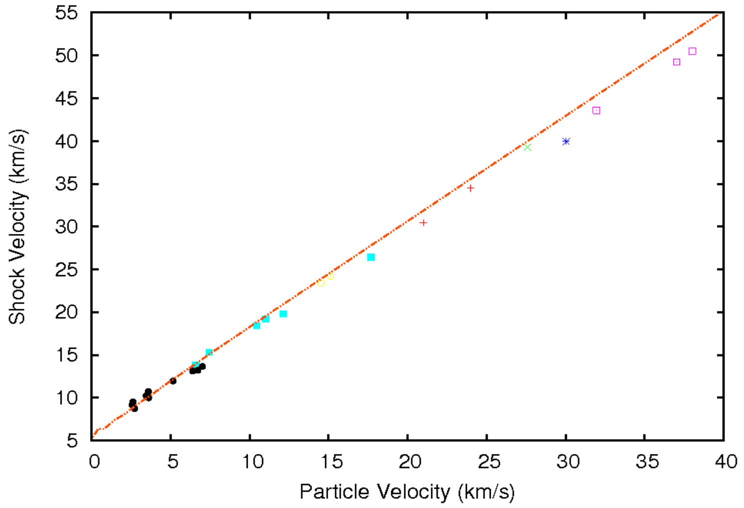

Figure 4.3: $U_s - U_p$ hugoniot. Solid line represents QEOS results and points represent experimental results [41, 102].

4.3.3 Electrical conductivity results

The frequency dependent electrical conductivity or optical conductivity $\sigma(\omega)$ is calculated using the Kubo Greenwood (KG) formula for an ionic configuration at a single time step within a molecular dynamics trajectory. Because of the numerical limitation of the Kubo-Greenwood formula,$\sigma(\omega)$ may artificially fall to zero for very small values of ω. Therefore it is difficult to calculate DC conductivity by using the KG formula, It is more convenient to estimate $\sigma(0)$ by using a given functional form for $\sigma(\omega)$. We fitted the computed conductivities $\sigma(\omega)$ to a Drude function

$$\sigma(\omega) = \frac{\sigma_{DC}}{1 + \omega^2\tau^2} \tag{4.11}$$

σ_{DC} is the DC conductivity and τ is the relaxation time. The conductivities computed by the KG formula for an ionic configuration at a single time step (time step number 400) within an AIMD trajectory of temperature 12000 K and density 2.35 g/cc, and its fitting by Drude formula are shown in figure 4.7. The fitted

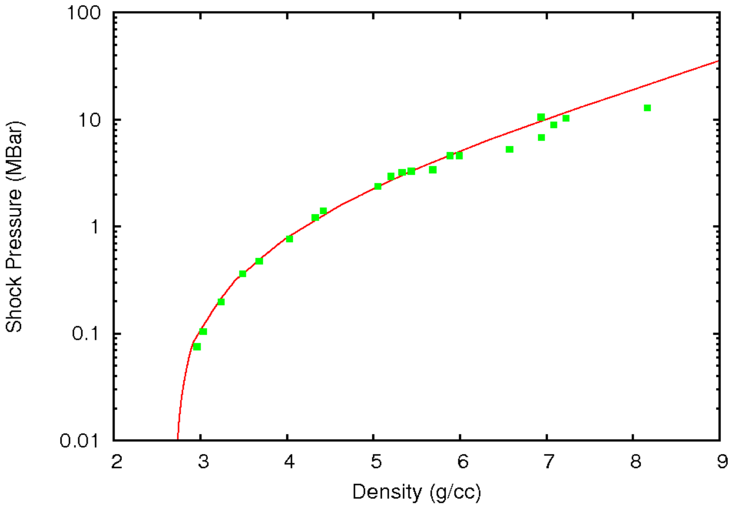

Figure 4.4: P-ρ hugoniot. Solid line represents QEOS results and points represent experimental results [30, 102]

values of σ_{DC} and τ are $21.1 \times 10^3\,(\Omega - cm)^{-1}$ and $4.8 \times 10^{-16} s$ respectively for this example.

The DC electrical conductivity σ for one density and temperature point is calculated by averaging over DC conductivities from 10 randomly selected ionic configurations of the AIMD trajectory for that density and temperature. We have shown our results for density = 2.35 g/cc and temperatures ranging from 2,000K to 12,000K in figure 4.8. We have also shown theoretical results of Recoules et. al. from [2] for comparison. Reasonably good agreement can be seen.

We can notice that the electrical conductivity as a function of temperature shows a break (change of slope) near 6000 K. The cause for this can be explained using Drude theory. Following the Drude theory, the electrical conductivity can be expressed as

$$\sigma = \frac{ne^2\tau}{m} \tag{4.12}$$

Here, n is the number density of electrons near Fermi surface, e is the electronic

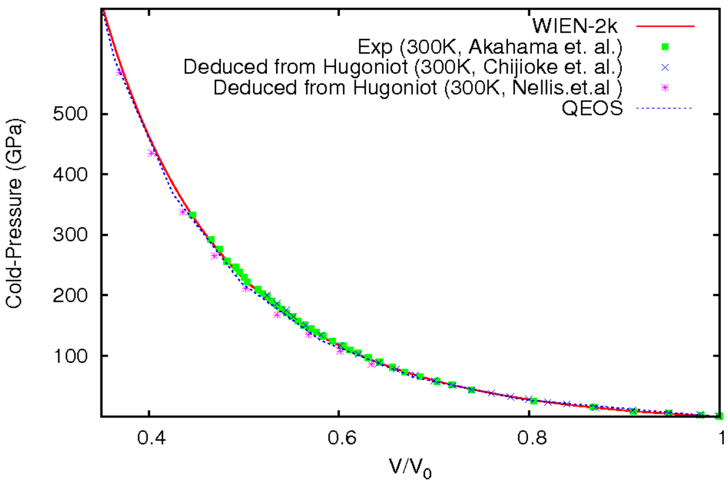

Figure 4.5: Cold curve generated by QEOS and FP-LAPW calculations and their comparison with experimental results [62, 75, 77]

charge, τ is the relaxation time and m is the mass of electron. Initially conductivity decreases very fast with temperature (up to 6000 K) as shown in figure 4.8. This can be understood in a simple manner. The ions vibrate about their equilibrium positions which leads to the thermal vibration of the crystal lattice. The amplitude of the vibration increases with the temperature. The electrons are scattered by collisions with the lattice ions. Consequently with the increase in the amplitude of vibration, the collision frequency increases. This leads to a decrease in the relaxation time τ and hence to a decrease in the conductivity. At very high temperature (above 6000 K), though the relaxation time τ is still decreasing with the temperature leading to decrease in the conductivity, but at the same time the number density of electrons near Fermi surface also starts increasing causing increase in the conductivity. These both phenomenas viz. the decrease in the relaxation time τ and the increase in the number density of electrons near Fermi surface jointly lead to less decrease in the electrical conductivity above the temperature 6000 K as compared to below this temperature. Hence, we see a break in the slope near

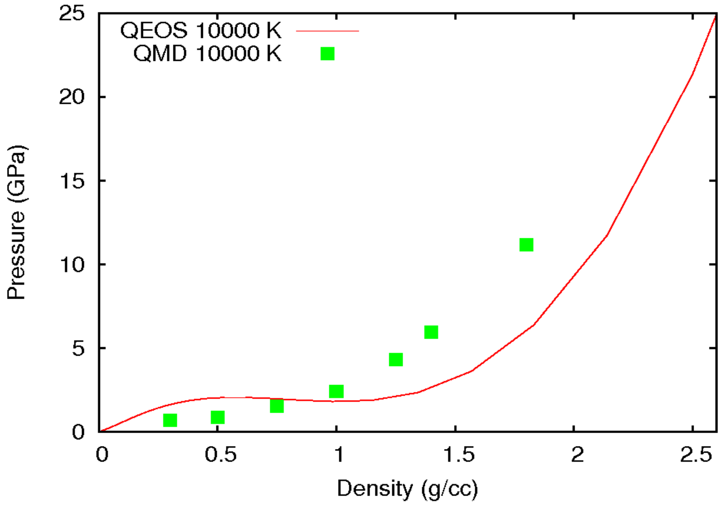

Figure 4.6: Isotherm (10000 K) generated by QEOS and AIMD simulations

6000 K.

4.4 Conclusion

We have presented equation of state results of Al using a Quotidian equation of state model and from first principles calculations. QEOS calculations have been performed using More's methodology. Full potential linearized augmented plane wave (FPLAPW) calculations have been performed within the framework of density functional theory for accurate calculations of cold curve. Ab-initio molecular dynamics simulations have been performed for calculating EOS for expanded metals. FPLAPW and AIMD simulation results have been compared with the QEOS results. The cold curves generated by using QEOS and FPLAPW methods for compressed states show good agreement, implying that QEOS results are accurate for compressed Al. However, in QEOS cold - curve (zero temperature isotherm) is calculated by applying semi-empirical bonding correction in zero temperature TF model, it requires experimental information such as normal density and bulk

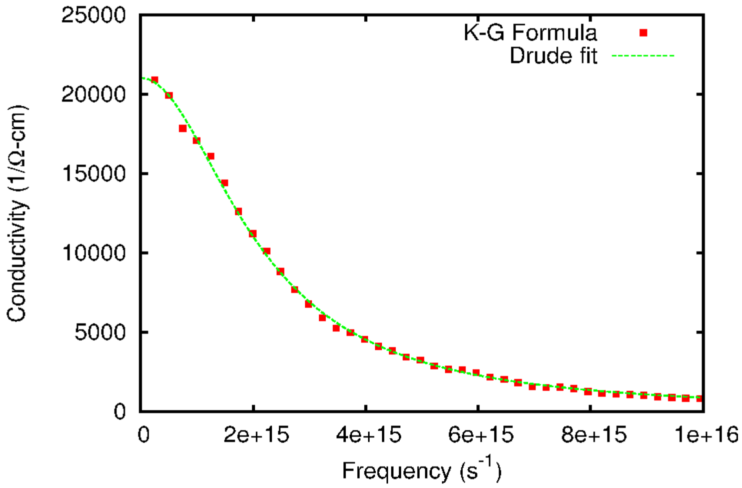

Figure 4.7: Optical conductivity of liquid aluminium at T = 12000 K and density = 2.35 g/cc. Points are showing the computed conductivities by Kubo-Greenwood formula and line shows the Drude fit.

modulus as input whereas FPLAPW is based on quantum mechanical method and does not require any experimental input.

QEOS results do not show good agreement with the AIMD simulations for expanded states, indicating that QEOS method gives less accurate results for the expanded states and low temperatures.

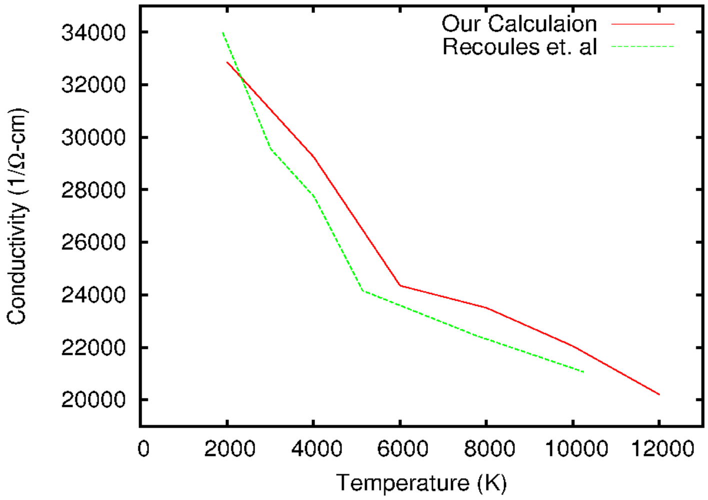

Figure 4.8: DC conductivity as a function of temperature for liquid aluminium at density 2.35 g/cc. Filled squares represent results from [53], circles show results from the present work.

5

Improvements in QEOS model and determination of Al EOS for Compressed and Expanded States

Abstract: In the last chapter we found that QEOS results agree well with ab-initio results for compressed states of Al, but do not agree with AIMD results for rarefied states. In this chapter we have developed an improved version of QEOS by incorporating ab-initio results to improve the accuracy of QEOS, for both rarefied and compressed states. In this model, instead of using the TF model for calculating the cold as well as electron thermal contributions, it is only used for the electron-thermal term by taking the difference of TF values at T=0 and finite temperatures. The Ion-thermal term is calculated using a modified version of the Cowan model where, in rarefied states, the adjustable parameters are tuned using quantum molecular dynamics (QMD) results. In compressed states, $P-\rho$ and $U_\mathrm{s}-U_\mathrm{p}$ Hugoniots derived using our results show good agreement with the

reported experimental results. In expanded states, the estimated critical temperature shows good agreement with the reported results and pressure versus internal energy along isochores show reasonably good agreement with published experimental results. This is a major improvement over the standard QEOS model, which yields unphysical critical temperatures.

5.1 Introduction

In the last chapter, we had observed that the QEOS model does not work well in rarefied states, i.e., for densities below normal. In this chapter, we describe the development of an improved version of the QEOS model that remove these limitations.

In this model, the cold-curve is calculated by different methods in three different density regions. It is calculated by a function fitted to FP-LPAW results near normal conditions (atmospheric pressure to 1000 GPa), since FP-LAPW is the most accurate theoretical method for calculating the cold curve in this region, Smooth extrapolation to merge with Thomas-Fermi-Dirac results is performed above 1000 GPa [11]. Below normal density we use a soft sphere function to extrapolate the cold-curve [11, 42].

For calculating the electron thermal contribution, we use the equations [9]:

$$E_{et} \;=\; E_{tf}(T,\rho) - E_{tf}(0,\rho) P_{et} \;=\; P_{tf}(T,\rho) - P_{tf}(0,\rho)$$

For the calculation of the thermal ionic contribution, we have used a modified Cowan model [42]. We have tuned the adjustable parameters of this model such that the EOS matches reasonably with the quantum molecular dynamics (QMD) results in expanded states. This is because QMD is regarded as the most accurate theoretical method for generating EOS data in low temperature expanded state of metals [53–55, 57–59].

The remainder of the chapter is organized as follows. The computational details are described in section 5.2 and results for the cold-curve and its comparison with experimental data are described in section 5.3.1. Comparisons of derived $P-\rho$ and $U_\mathrm{s}-U_\mathrm{p}$ Hugoniots are done with reported experimental Hugoniots in section 5.3.2. Isotherms and isochores of expanded states are given in section 5.3.3. Results for stable, unstable and metastable phases and critical point are discussed in section 5.3.4. Concluding remarks are presented in section 5.4.

5.2 Computational Details

5.2.1 Cold-curve calculations

The ab-initio cold contribution is taken from FPLAPW calculations. The density vs pressure data generated in Chapter 3 for FCC Al is fitted to a function :

$$P_\mathrm{C}\left(\rho, T=0\right) = \sum_{\mathrm{i}=1}^{6} a_\mathrm{i} \eta^{\left(\frac{\mathrm{i}}{3}+1\right)} \tag{5.1}$$

$$E_\mathrm{C}\left(\rho, T=0\right) = \int_{\rho_0}^{\rho} P_\mathrm{C}\left(\rho, T=0\right) \tag{5.2}$$

Here, $\eta = \rho/\rho_0$, ρ_0 is density of the solid at standard conditions and $\rho > \rho_0$. This function is extrapolated for $\rho < \rho_0$ using a soft-sphere function [11, 42].

$$E_\mathrm{C}\left(\rho, T=0\right) = A\rho^{f_1} - B\rho^{f_2} + E_\mathrm{B} \tag{5.3}$$

$$P_\mathrm{C}\left(\rho, T=0\right) = -\frac{\partial E_\mathrm{C}}{\partial \rho} \tag{5.4}$$

where $f_1 = 2.0$, $f_2 = 0.5$ and the binding energy of Al $E_\mathrm{B} = 1.2 \times 10^7$ J/kg [42].

Constants A and B are obtained by making energy and pressure equal to the energy and pressure calculated by equations 5.1 and 5.2 respectively at normal density (ρ_0). Above 1000 GPa, we extrapolate the cold-curve using the Thomas-Fermi-Dirac (TFD) analytic formula [11]. This high-density formula is based upon the TFD statistical model of atom which is believed to be accurate at pressures above 10^3 GPa [11].

5.2.2 Ion-Thermal contributions

The ion thermal contribution of EOS describes the pressure and energy associated with ion or nuclear motion. For calculating ion EOS, we have used the modified Cowan model [42]. This yields the pressure, energy, entropy and free energy, taking into account density-dependent melting temperature, Debye temperature and Grüneisen parameter for any material. Details of the Cowan model are described in [10] and modifications are given in [42]. The advantage of using this model is that it provides adjustable parameters for calculating Grüneisen parameter in expanded states. These parameters can be tuned in such a way that the calculated three-term EOS matches with the QMD simulation results. Important relations for obtaining ion thermal energy and pressure are described in the chapter 4.

5.2.3 Electron-Thermal contributions

For calculating electron equation of state, we use Thomas-Fermi statistical model of atom. In Thomas-Fermi statistical theory, the electrons are treated as a charged fluid surrounding the nucleus; properties of this electron gas are obtained from finite temperature Fermi Dirac statistics. Equations for calculating thermodynamic properties using this model are described in [9, 10].

5.3 Results and Discussion

5.3.1 Cold-curve

The cold curve calculated by FP-LAPW method using WIEN-2K code is shown in fig. 5.1. Now, it is known that pressure-induced FCC-HCP and HCP-BCC structural transformations occur in Al at high pressures. However, differences in the energies of FCC and HCP structures and HCP and BCC structures are so small that these structures coexist over a wide range of pressures, as discussed in Chapter 3. Hence, for purposes of EOS calculations in this chapter, we have assumed Al to exist in an FCC structure at all pressures. This is also supported by recent results from Pickard [100] that find that Al remains in closed packed structures (FCC, HCP or BCC) up to 3.2 Terapascals (TPa) and no other structural transformation takes place upto this pressure.

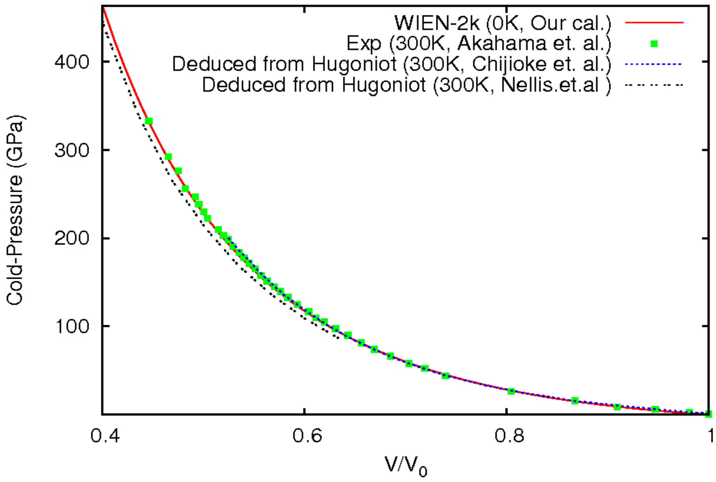

Figure 5.1: Comparison of theoretically calculated Cold-curve (zero-temperature isotherm) of Al with experimental 300 K isotherm.

Figure 5.1 compares our computed values with experimentally-measured T=300 K data obtained by powder x-ray diffraction experiments [62], and with the cold curve deduced from shock experiments [77] and nellis et. al. [75]. There is good agreement with the Akahama and Chijioke's data, but our values tend to be higher than those deduced from Nellis' results.

Table 5.1: The coefficients of eq. 5.1, in Megabar

a_1	a_2	a_3	a_4	a_5	a_6
27.92	-104.8	151.7	-108.8	39.78	-5.815

Calculated ρ vs. P data is fitted to eq. 5.1 and density dependent energy can be calculated by using eq. 5.2. Fitted values of parameters a_i, $i = 1, 6$ are given in table 5.1. The cold-curve so generated is extrapolated to expanded states using eq. 5.3 and eq. 5.4.

In fig. 5.2 we have shown a density vs energy plot for compression as well as rarefaction. It can be seen that energy approaches to cohesive energy for ρ tending to zero and exhibits minimum for $\rho = \rho_0$.

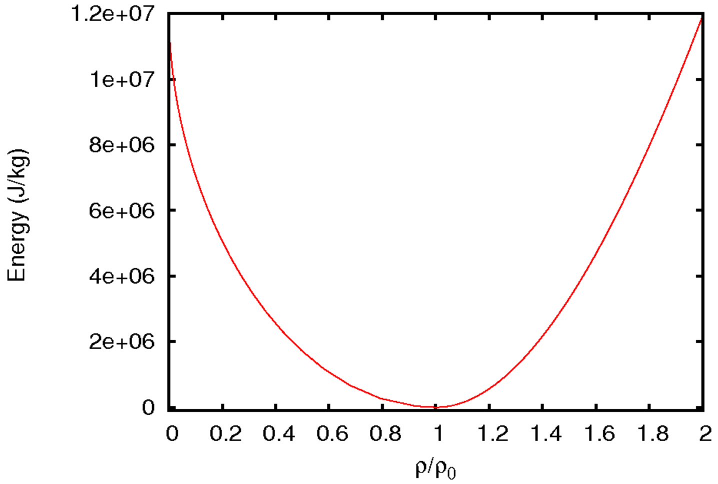

Figure 5.2: Energy as a function of density; for $\rho/\rho_0 > 1$, it is calculated using FPLAPW method and for $\rho/\rho_0 < 1$, it is calculated using a soft sphere function.

5.3.2 Comparison of derived $P-\rho$ and $U_\mathrm{s}-U_\mathrm{p}$ Hugoniots with experimental Hugoniots for compressed Al

To validate the EOS data generated in this work we have derived $P-\rho$ and $U_\mathrm{s}-U_\mathrm{p}$ Hugoniots and compared them with experimental Hugoniots. The generated EOS is combined with the three Hugoniot equations viz., $\rho_0 U_\mathrm{s} = \rho_1\left(U_\mathrm{s}-U_\mathrm{p}\right)$, $P_1-P_0 = \rho_0 U_\mathrm{s} U_\mathrm{p}$ and $E_1-E_0 = \frac{1}{2}\left(P_1+P_0\right)\left(V_0-V_1\right)$ to derive the $P-\rho$ and $U_\mathrm{s}-U_\mathrm{p}$ Hugoniots [9]. In these equations, ρ, E, and P are density, energy and pressure respectively. $V = 1/\rho$, U_s and U_p are shock and particle velocities respectively. The suffixes 1 and 0 represent the quantities in the shocked and the un-shocked regions. The calculated $U_\mathrm{s}-U_\mathrm{p}$ and $P-\rho$ Hugoniots are plotted in fig. 5.3 and fig. 5.4 respectively. For comparison, experimental shock compression data [30,41,102] are also shown. Good agreement with the experimental Hugoniot can be seen up to large compression.

It may be noted that at intermediate pressures (500 - 10000 GPa), the TF model does not give the correct Hugoniot, since pressure ionization leads to a slightly oscillatory behaviour of the hugoniot [30,101]. At these densities, the Hugoniot can be corrected by making use of an average atom model for the electron-thermal term, which is based on the quantum mechanical structure of the atom [30].

5.3.3 Expanded States

In expanded states, the three term EOS model is represented by following equation

$$P_\mathrm{TOT}\left(\rho,\ T\right) = P_\mathrm{C} + \frac{\rho k T}{A M_\mathrm{P}}\left(1 + \left[3\left(b_1 + b_2\rho/\rho_0\right) - 1\right] w^{\frac{1}{3}}\right) + P_\mathrm{ET} \tag{5.5}$$

Here the first term is the cold term P_C which is calculated using Eq. 5.4 [11,42], the second term is ion-thermal term P_IT [10,42] (see the appendix) and third is

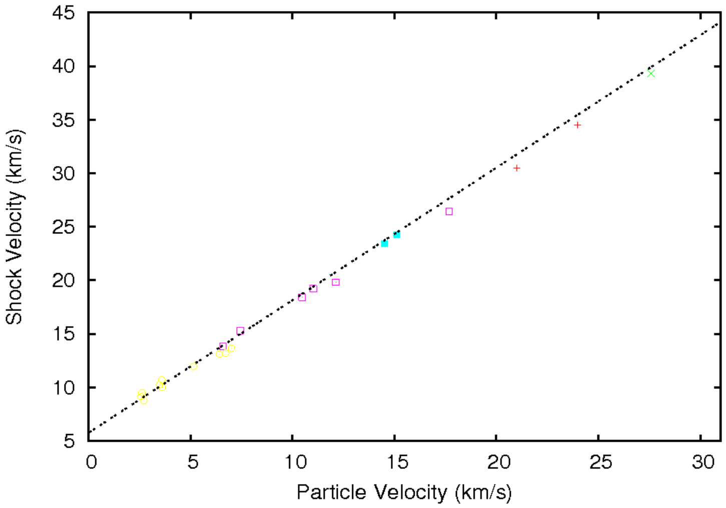

Figure 5.3: $U_\mathrm{s} - U_\mathrm{p}$ Hugoniot. Solid line represents our results and points represent experimental results [41, 102]

the electron thermal term P_ET which is calculated using the TF model [9, 10, 42]. $w = T_\mathrm{m}(\rho)/T$, where T_m is the melting temperature, $b_1 + b_2\rho/\rho_0 = \gamma_\mathrm{s}$ is the Grüneisen parameter.

In the present work, the adjustable parameters b_1 and b_2 have been tuned in such a way that the function $P_\mathrm{TOT}(\rho,\ T)$ matches reasonably well with our QMD results. The values of b_1 and b_2, along with the calculated value of Grüneisen parameter for $\rho/\rho_0 = 1$ and its experimental value, are given in Table 5.2. These values do not depend on temperature.

Table 5.2: Values of b_1, b_2 and Grüneisen parameter

b_1	b_2	Cal. $\gamma_\mathrm{s}(\rho/\rho_0 = 1)$	Exp. $\gamma_\mathrm{s}(\rho/\rho_0 = 1)$ [9, 10]
0.333	2.197	2.53	2.17

The value of calculated Grüneisen parameter agrees reasonably well with its experimental value at ambient conditions. Note that this expression for Grüneisen parameter is only used for expanded states, hence it should not be expected to yield the limiting value of 2/3 at high pressures.

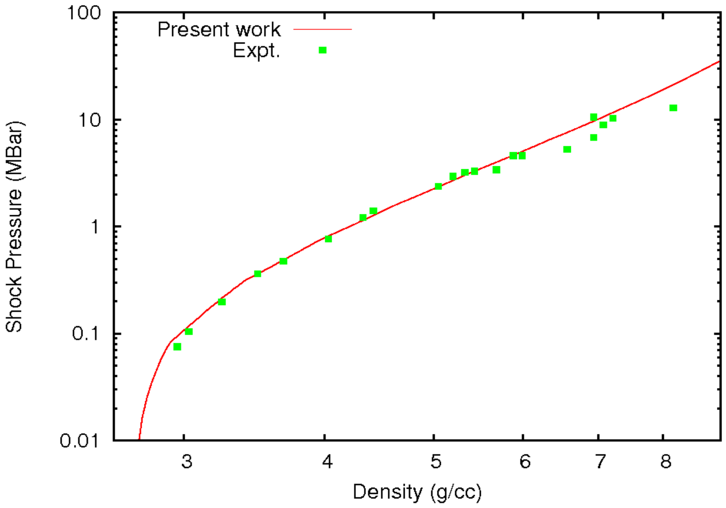

Figure 5.4: P-ρ Hugoniot. Solid line represents our results and points represent experimental results [30, 102]

Isotherms obtained from our improved QEOS model are plotted along with QMD results for the temperatures 10000 K and 15000 K in fig. 5.5. In fig. 5.6 we have shown pressure versus internal energy along five isochores $V/V_0 = 1.93, 2.7, 4.0, 5.4, 9.0$. For comparison, we have also shown experimental results taken from [58]. Our results show reasonably good agreement with experimental results.

5.3.4 Estimation of Critical temperature

Critical temperature of Al in the liquid-vapour regime is predicted inaccurately by More's QEOS model [10]. Young et. al and Ray et. al. have improved QEOS by making empirical corrections in this regime. Since we have improved EOS by incorporating ab-initio results, we would like to check its accuracy by estimating critical temperature using improved EOS. For this purpose, we have shown isotherms for temperatures 7458 K, 7923 K, 8387 K and 8851 K for expanded states of Al in fig. 5.7. We can see that isotherms of temperatures below 8387 K show an oscillatory behaviour (wavelike structure). For example, the 7458 K

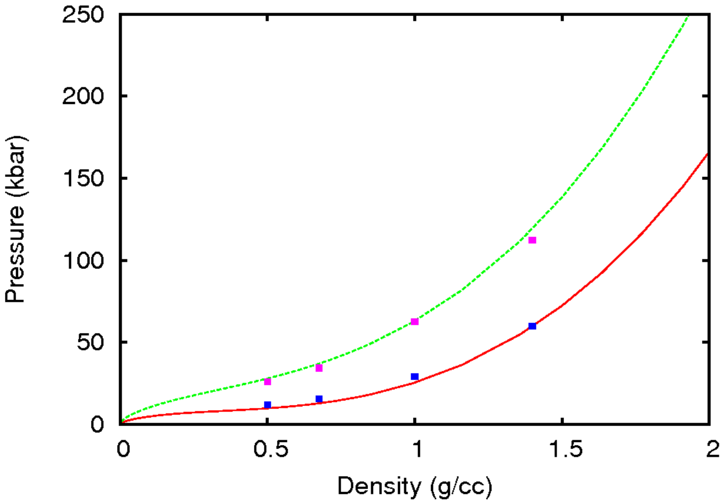

Figure 5.5: Isotherms for temperatures 10000 K and 15000 K. Points represent QMD results and line represents three term EOS fitted to QMD results.

isotherm shows oscillatory behaviour from point b to point f. In this range of the 7458 K isotherm, the oscillating part can be divided in four parts $b-c$, $c-d$, $d-e$ and $e-f$. In the first part $b-c$ of the oscillating isotherm, the pressure first starts increasing from a value of 2.24 kbar at b and reaches a maximum value of 2.89 kbar at c. In the second part $c-d$, pressure decreases from this maximum value to 2.24 kbar at point d. In the third part $d-e$ of the oscillating isotherm, pressure starts decreasing below 2.24 kbar and reaches a minimum value 1.7 kbar at e, and in the fourth part $e-f$, pressure starts increasing from the minimum value of third part to the minimum value of the first part i.e. 2.24 kbar. Thus it can be readily seen that, for a certain pressure 2.24 kbar, there are three values of density marked as b, d and f. In the density range below starting point of the first part (from point a to b) and in the density range above the maximum density of the fourth part (from point f to g) the expanded state of Al is stable because in these density ranges $\partial P/\partial \rho > 0$. The state in the second and third parts of the oscillating isotherm is unstable because in these states $\partial P/\partial \rho < 0$. First and fourth part

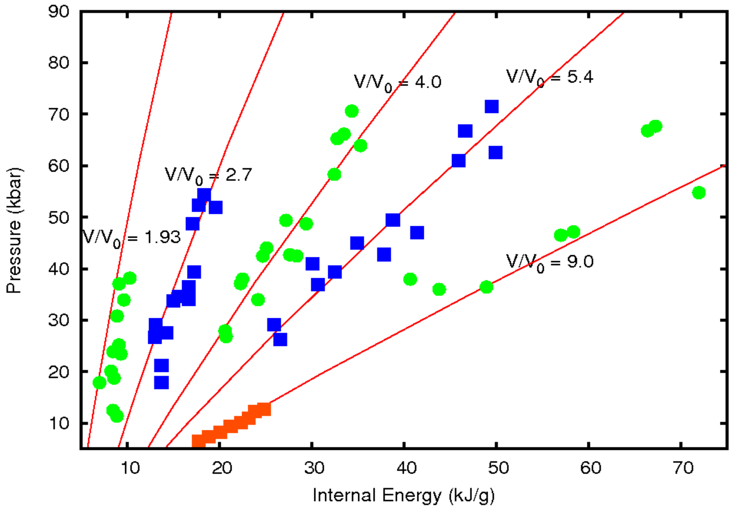

Figure 5.6: Pressure versus internal energy along five isochores ($V/V_0 = 1.93, 2.7, 4.0, 5.4, 9.0$). Symbols represent experimental data taken from [58] and lines represent our calculation.

of the oscillatory isotherm are metastable states. These represent super-saturated vapour and super heated liquid respectively.

We notice that on 7458 K isotherm, for a pressure 2.24 kbar, there are three values of density marked as b, d and f. If the temperature is decreased the isotherms would move down, loops of the wavelike structure of the isotherms would become larger and larger and the points corresponding to b, d and f move farther from one another.

Table 5.3: Critical density, temperature and pressure obtained in this work and reported results

Reference	ρ_c (g/cc)	T_c (K)	P_c (kbar)
This work	0.385	8387	4.45
Ref [122]	0.28	8860	4.68
Ref [123]	0.43	8944	4.726
Ref [124]	0.785	8472	5.094
Ref [125]	0.66	7917	4.67

As the temperature is raised, the isotherms move up, the loops become smaller

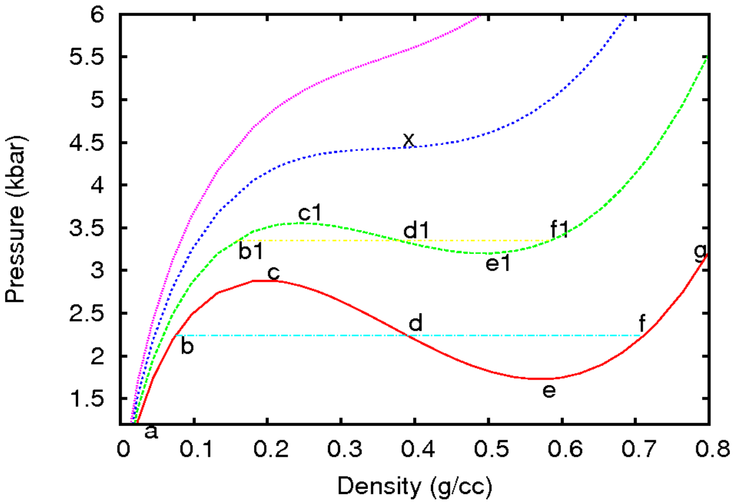

Figure 5.7: Isotherms for temperatures 7459 K, 7923 K 8387 K and 8859 K calculated by three term EOS model which is fitted to QMD simulation results. Straight lines $b - f$ and $b1 - f1$ are the Maxwell constructions.

and the points corresponding to b, d and f get closer to one another. At a certain temperature, the wave-like structure disappears and these three points become identical. The point where these three points merge is shown by the point x. This point is critical point.

The temperature of this particular isotherm at which critical point lies is the critical temperature, and the density and pressure corresponding to this point x, are the critical density and critical pressure. $\partial P/\partial \rho$ and $\partial^2 P/\partial \rho^2$ are equal to zero at this point. In table 5.3, we have given results of estimated critical density, temperature and pressure. For comparison, we have also given results reported in the literature. We can see that our results agree reasonably well with these results. The metallic - nonmetallic transition cannot be obtained in our calculations because we have used the TF model for the electron-thermal term. This transition can be created by implementing quantum mechanical average atom model for electron thermal term [30].

5.4 Conclusion

We have developed an improved version of the QEOS model based on first principle results in both compressed and rarefied states of Al. In compressed states, we used a function for the cold curve which is fitted to our calculated FP-LAPW data. In expanded states, we have used a soft-sphere function. The cold curve shows good agreement with the experimental results. The ion-thermal contribution is determined using a density-dependent Gruneisen parameter that is determined by fitting to QMD results. The electron-thermal contribution is determined from the Thomas-Fermi model.

$U_\mathrm{s} - U_\mathrm{p}$ and $P - \rho$ Hugoniots obtained using this EOS data show reasonably good agreement with the reported experimental Hugoniots. In expanded states, pressure versus internal energy shows reasonably good agreement with the reported experimental results and the estimated critical temperature also shows good agreement with published results. This is a major improvement over the standard QEOS model, which yields unphysical critical temperatures. Better models for electron thermal contribution, such as average atom model, will be used in future to create metal - nonmetal transition in expanded state and to correct Hugoniot at very high density.

6

FP-LAPW Calculation of Equation of State and Elastic Properties of Tungsten Carbide at High Pressures

Abstract: Tungsten carbide is used in high pressure devices. Hence knowledge of its equation of state and its constituent properties such as elastic properties, Gurneisen parameter, Debye temperature and melting temperature and their pressure dependence is of great practical importance. In this chapter, we present and discuss first principles results of equation of state, elastic properties and electronic properties of α and β phases of tungsten carbide at high pressure and compare our results with reported experimental results. Enthalpies of α and β phases of WC have been compared up to 350 GPa to investigate the possibility of structural transformation. The density-dependent Grüneisen parameter has been deduced from $P-V$ isotherm using well known Slater's formula. High pressure elastic constants of α and β phases of WC have been calculated by applying various

distortions to the original crystal structure. The elastic properties such as bulk, shear and Young's moduli have been derived from the calculated elastic constants. Debye temperature and melting temperature have been deduced from the elastic properties. These calculations have been performed using the FP-LAPW method within the framework of density functional theory.

6.1 Introduction

High-pressure studies of practical importance can involve elements as well as compounds. As discussed earlier, pulsed-power experiments such as electromagentically-accelerated liners and exploding foils make use of Aluminium. That was the motivation for studying the EOS and other properties of Al in great detail. Some other high-pressure applications and studies require the use of ceramics. Tungsten carbide (WC) is used as an anvil in multi-anvil high pressure systems and as seats in diamond anvil cells [34]. It is also a promising material for applications in industrial machinery, cutting tools, and other instruments due to its hardness [35]. Hence, in this chapter, we extend the study of EOS and other properties to WC.

The room temperature crystalline form of tungsten carbide is a hexagonal structure which is known as α WC. This is a unique behaviour of WC among transition metal carbides as other carbides are stable in rock-salt structure. In addition to this α phase, WC can also exist in FCC structure at high temperatures, this phase is known as β WC. At room temperature β WC can be synthesized by a rapid quenching process [126] and by a plasma synthesis technique [127].

Experimental investigation of EOS, structural properties and elastic properties of WC at high pressures has been a subject of interest for more than two decades. Day and Ruoff [128] investigated pressure dependence of these properties of WC with 3% Co binder up to 0.2 GPa, Gerlich and Kennedy [129] extended this investigation up to 1 GPa. Recently, Amulele et al. [35] and Litasov et. al. [34] have performed synchrotron x-ray diffraction experiments on polycrystalline powder samples loaded in a diamond anvil cell. Amulele et al. [35] have also performed ultrasonic experiments on hot-pressed ceramics compressed in a multianvil high-pressure apparatus. In these experiments [34,35], pressure versus volume relations and elastic properties of WC have been determined.

On the theoretical side, several first principles calculation results have been reported [78–83]. However, the focus of these theoretical investigations has been on the zero pressure physical, elastic and electronic properties. Despite being a promising material for applications in high pressure devices, elastic properties of tungsten carbide at high pressure have not been reported by any author in any theoretical investigation. In this paper we compare the enthalpies of α and β WC upto 350 GPa, to investigate the possibility of structural transformation in WC at high pressure and discuss the findings of this investigation in terms of density of states. We also present elastic properties of α and β phases of WC up to a pressure of 120 GPa and discuss the stability, ductility/brittility and anisotropic behaviour of these phases. To the best of our knowledge, high pressure elastic properties of α and β WC are not reported in any previous theoretical investigation.

The remainder of the paper is organized as follows. The computational details are described in section 6.2. Important results are described in the section 6.3. In this section we have presented and discussed results related to zero temperature equation of state such as molecular volume, bulk modulus, lattice parameters, $P-V$ isotherm, investigation of structural transformation and Grüneisen coefficient etc. We have also presented and discussed results related to elastic properties at high pressures such as elastic constants, bulk, shear and Young's moduli, Poisson ratio, transverse and shear velocities, Debye temperature and melting temperature in this section. Conclusive remarks are given in section 6.4.

6.2 Computational Details

6.2.1 Total energy calculation using FPLAPW method

FPLAPW calculations within the framework of density functional theory [84, 85] have been performed using WIEN-2k code [26, 92]. The exchange correlation potential within GGA is calculated using the scheme of Perdew - Burke- Ernzerhof [88]. These calculations have been done using constant muffin-tin radius R_{mt} of 1.9 a.u. for tungsten and 1.68 a.u. for carbon. In the FPLAPW method, it is very important to select a good basis set and k mesh size for getting accurate results. We start by taking a low value of $R_{\mathrm{mt}}K_{\mathrm{max}}$ (= 6.0). For the purpose of determining a suitable k -mesh size, we then calculate the total energy as a function of the size of the k -mesh increasing the size by 1000 at each step. We find that 8,000 k-points are sufficient. Having determined a good k-mesh, we now vary $R_{\mathrm{mt}}K_{\mathrm{max}}$ from 7 to 12, and find that 9 is a good choice. We have selected an energy cut-off of -6.0 Ry to separate the core from the valence states. The convergence criteria for energy was taken as 10^{-5} Ry.

6.2.2 Independent elastic constants of α and β WC.

From Hooke's law of stress - strain relationship, It has been shown that total number of elastic constants are 81 and elasticity can be represented by a fourth rank tensor. A further general argument reduces their number to 36. Using Voigt's two-suffix notation, the elasticity tensor of 36 independent constants can be represented by following matrix

$$\begin{pmatrix} C_{11} & C_{12} & C_{13} & C_{14} & C_{15} & C_{16} \\ C_{21} & C_{22} & C_{23} & C_{24} & C_{25} & C_{26} \\ C_{31} & C_{32} & C_{33} & C_{34} & C_{35} & C_{36} \\ C_{41} & C_{42} & C_{43} & C_{44} & C_{45} & C_{46} \\ C_{51} & C_{52} & C_{53} & C_{54} & C_{55} & C_{56} \\ C_{61} & C_{62} & C_{63} & C_{64} & C_{65} & C_{66} \end{pmatrix}. \tag{6.1}$$

The number of elastic constants can be reduced still further by exploiting the symmetry of the particular crystal at hand. For example a cubic crystal has only three and a hexagonal crystal has only five independent elastic constants.
First principles calculations based on DFT provide reliable results for these elastic constants of crystalline materials. For calculating elastic constants, the ground state crystal structure is distorted by applying symmetry dependent strains with varying amplitudes. The total energy of the strained crystal E_{tot} can be expressed as :

$$E_{\mathrm{tot}} = {E_{\mathrm{tot}}}^{0} + P\left(V - V_0\right) + \phi_{\mathrm{elast}} \tag{6.2}$$

where ${E_{tot}}^0$ and V_0 are the total energy and the volume of an unstrained crystal. V is the volume of the distorted crystal. According to Hooke's law, elastic energy can be expressed as :

$$\phi_{\mathrm{elast}} = \frac{V}{2}.C_{\mathrm{ij}}\epsilon_{\mathrm{i}}\epsilon_{\mathrm{j}} \tag{6.3}$$

Hence elastic constants can be derived from the second-order derivatives of E_{tot}:

$$C_{\mathrm{ij}} = \frac{1}{V_0}\frac{\partial^2 E_{\mathrm{tot}}}{\partial \epsilon_{\mathrm{i}} \partial \epsilon_{\mathrm{j}}} \tag{6.4}$$

a cubic crystal, for example β phase of WC, has only three independent elastic constants, C_{11}, C_{12} and C_{44}. As a result a set of three equations is needed to determine these constants. This means that three types of strains must be applied to the initial crystal. First type involves calculating the bulk modulus by varying the volume, second type involves performing volume conservative tetragonal strains and third type strain involves rhombohedral distortions. A hexagonal crystal such as α phase of WC, has 7 non zero elastic constants $C_{11}, C_{12}, C_{13}, C_{33}, C_{44}$, C_{55} and C_{66}. Out of these 7 elastic constants only 5 are independent since $C_{55} = C_{44}$ and $C_{66} = \frac{1}{2}(C_{11} - C_{12})$. Hence we need five different strains to determine these elastic constants [131]. First distortion involves changing the size of the basal plane and keeping z axis constant. The symmetry of the resultant lattice remains hexagonal. Second distortion involves increasing the x axis and decreasing the y axis with an equal amount and keeping z axis constant. In this case, the symmetry of the strained lattice is monoclinic. In third distortion z axis is stretched keeping other axes unchanged. In this distortion, hexagonal symmetry remains in the strained crystal. The fourth distortion involves changing the hexagonal crystal in to triclinic crystal. The fifth distortion involves volume changes and calculation of bulk modulus.

The calculated elastic constants can be used to determine anisotropy constants of α and β WC. There are three types of anisotropy constants for α WC, one for compression wave and two for shear waves. These anisotropy constants can be calculated using following relations [132]

$$\Delta P = \frac{C_{33}}{C_{11}},\ \Delta S_1 = \frac{C_{11} + C_{33} - 2C_{13}}{4C_{44}},\ \Delta S_2 = \frac{C_{44}}{C_{66}} \tag{6.5}$$

The anisotropy constant of β WC can be calculated using following relation

$$A = \frac{2C_{44}}{C_{11} - C_{12}} \tag{6.6}$$

6.2.3 Bulk and Shear Moduli

Once the elastic constants are calculated, the bulk modulus and shear modulus can be calculated following the Voigt [133] and Reuss [134] approximations. The approximation relations for cubic and hexagonal crystals are as under:

HCP structure (α) phase

For hexagonal crystal the relations for bulk modulus and shear modulus are

$$B_{\mathrm{V}} = \frac{2}{9}\left(C_{11} + C_{12} + 2C_{13} + \frac{1}{2}C_{33}\right) \tag{6.7}$$

$$B_{\mathrm{R}} = \frac{\left(C_{11} + C_{12}\right)C_{33} - 2{C_{12}}^2}{C_{11} + C_{12} + 2C_{33} - 4C_{13}} \tag{6.8}$$

$$G_{\mathrm{V}} = \frac{1}{30}\left(C_{11} + C_{12} + 2C_{33} - 4C_{13} + 12C_{55} + 12C_{66}\right) \tag{6.9}$$

$$G_{\mathrm{R}} = \frac{5/2\left[\left(C_{11} + C_{12}\right)C_{33} - 2{C_{13}}^2\right]C_{55}C_{66}}{3B_{\mathrm{V}}C_{55}C_{66} + \left[\left(C_{11} + C_{12}\right)C_{33} - 2{C_{13}}^2\right]\left(C_{55} + C_{66}\right)} \tag{6.10}$$

In these equations, suffixes V and R represent Voigt [133] and Reuss [134] approximations respectively.

FCC structure (β) phase

For the cubic symmetry the relations for bulk modulus and shear modulus are

$$B = B_{\mathrm{V}} = B_{\mathrm{R}} = \left(C_{11} + 2C_{12}\right)/3 \tag{6.11}$$

$$G_{\mathrm{V}} = \left(C_{11} - C_{12} + 3C_{44}\right)/5 \tag{6.12}$$

$$G_{\mathrm{R}} = \frac{5C_{44}\left(C_{11} - C_{12}\right)}{3\left(C_{11} - C_{12}\right) + 4C_{44}} \tag{6.13}$$

6.3 Results and Discussion

We first describe the results related to equation of state such as equilibrium molecular volume (or density), pressure dependent lattice parameters and $P-V$ isotherm. We present results of these calculations in sections 6.3.1, 6.3.2 and 6.3.3 respectively. From the calculated equation of state we determine pressure dependent enthalpies of α and β WC and compare them to test the stability of these phases in section 6.3.4. We also discuss the outcomes of this comparison in terms of density of states in the section 6.3.5. We finally deduce Grüneisen coefficient from our $P-V$ isotherm and predict its density dependent nature in section 6.3.7.

6.3.1 Molecular volume of α and β WC at ambient pressure

The calculated total energies of α and β phases of WC for different volumes of the unit cell are fitted to the following Birch - Murnaghan equation of state:

$$E = E_0 + \frac{9}{16}V_0B_0\left[\left(\eta^2-1\right)^3B' + \left(\eta^2-1\right)^2\left(6-4\eta^2\right)\right], \quad \eta = \frac{V}{V_0} \tag{6.14}$$

From the least square fitting of equation 6.14, we obtain the equilibrium volume (V_0), bulk modulus (B_0) and pressure derivative of bulk modulus ($B^{'}$) for both phase of WC. The calculated values of these properties are listed in table 6.1. Available experimental values [35, 126, 127] of these properties for both structures are also given in table 6.1 for the comparison. The equilibrium molecular volume of $\alpha-$WC shows good agreement with the XRD result, our calculations overestimate the molecular volume by only 1.2 %. Calculated bulk modulus is close to the experimental bulk modulus obtained from ultrasonic measurement of [35] and XRD results of [34]. Differences between calculated bulk modulus and its mean values obtained in the XRD and the ultrasonic experiments are only 1.8 % and 1.48 % respectively. Calculated equilibrium volume of $\beta-$ WC also shows reasonably good agreement with reported measured volume.

Table 6.1: Equilibrium volume, bulk modulus and pressure derivative of bulk modulus of tungsten carbide

		$\alpha-$WC			$\beta-$WC	
Method	V (a.u.)	B (GPa)	B_{P}	V (a.u.)	B (GPa)	B_{P}
Exp. [35] (XRD)	20.806 ± 0.02	411.8 ± 12.1	5.45 ± 0.73			
Exp. [35] (ULTRA.)		382.9 ± 0.0	2.61 ± 0.07			
Exp. [34] (XRD)	20.75 ± 0.002	384 ± 4	4.65 ± 0.32			
Exp. [126]				18.91		
Exp. [127]				19.41		
Our Cal.	21.058	389.7	4.04	21.001	371.9	4.20

6.3.2 Lattice parameters of α and β WC at high pressures.

Total energies of α and β phases of tungsten carbide were calculated by varying the volume of the unit cell. β phase is FCC therefore only parameter which changes with volume is âĂŸaâĂŹ but α phase is HCP, therefore c and a both parameters change with the volume. Hence for α WC, c/a ratio at each volume must also be calculated accurately. This is done by determining the c/a ratio that minimizes system energy at a given volume V. To this end, we have calculated the total energy of HCP structure of WC by varying the c/a ratio for all the volumes. The c/a ratio was varied from -6% to 20 % in steps of 2 %, around $c/a = 0.98$. In figure 6.1, we have plotted variation of lattice parameters of $\alpha-$ (a and c) and β (a) phases of WC with the variation of of pressure. We have found that c/a ratio increases on increasing the pressure. We have also plotted experimental a and c of $\alpha-$ WC for the comparison. We can see that our results show a reasonably good agreement with experimental results. The maximum deviation in a and c are 1.06 % and 1.03 % respectively. This deviation is reasonable because of two reasons, firstly the sample of WC used in the experiment may not be 100% perfect and secondly small deviation of GGA results from the experiment is common. The good agreement between our results and experimental results validate the accuracy and reliability of our results at high pressure.

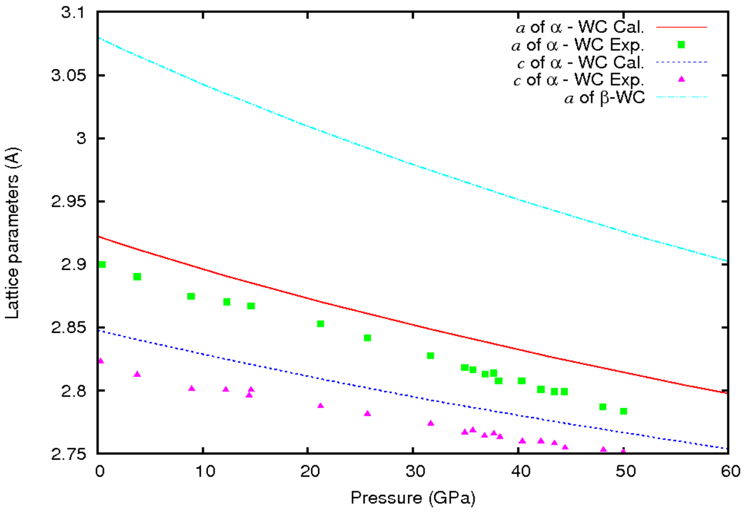

Figure 6.1: Variation of lattice parameters of α and β WC with pressure.

6.3.3 Zero temperature $P - V$ isotherm of α WC.

The relation of pressure and volume at zero kelvin is known as zero temperature isotherm or cold compression or cold - curve. From fitted Birch Murnaghan equation of state $E(V)$, pressure can be easily calculated by using the relation $P = -dE/dV$ which is based on the first law of thermodynamics. To validate our calculations at high pressure using this relation, we have generated zero temperature $P - V$ isotherm for α WC. We have shown our $P - V$ isotherm along with the results of XRD and ultrasonic measurements of Amulele et. al [35] and XRD measurement of Litasov et. al. [34] in the figure 6.2. Our results show small deviation from the results of [35]. Our isotherm lies below XRD results and above ultrasonic measurement results. However, our results are in excellent agreement with the XRD results of [34]. This further validates our calculations at high pressure.

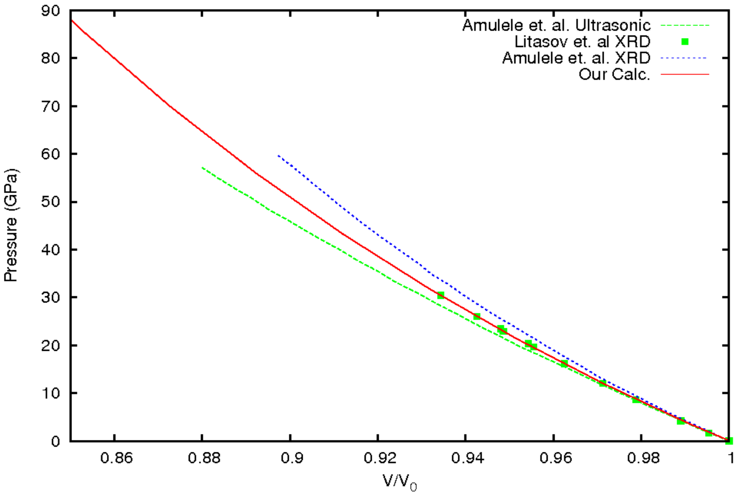

Figure 6.2: Zero temperature isotherm of α WC

6.3.4 Investigation of structural transformation

The structural transformations are investigated by comparing the Gibbs free energy versus pressure curves of different structures. The crossing of these curves of two structures provide information of the transition pressure. In our case temperature is zero kelvin therefore the Gibbs free energy is calculated by the thermodynamic relation $G = E + PV$ which is enthalpy H. The enthalpy variations of α and $\beta-$WC with the variation of pressure from zero to 350 GPa are shown in the figure 6.3. We can see that the enthalpy curve of α WC is lower than that of $\beta-$WC up to the maximum pressure. Hence, we can conclude that tungsten carbide is thermodynamically stable in the $\alpha-$ WC phase and no $\alpha - \beta$ structural transformation takes place up to the pressure of 350 GPa. This can be understood with the help of nature of density of state (DOS) curve near Fermi level. We have discussed this in section 6.3.5.

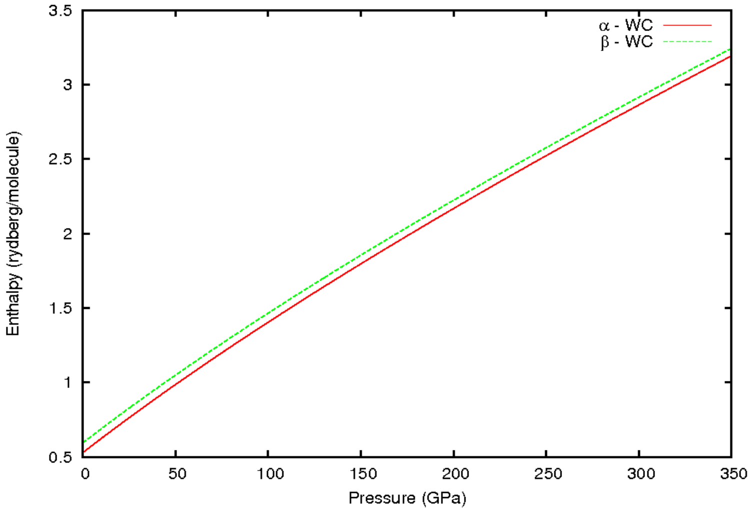

Figure 6.3: Variation of enthalpies of α and β WC with pressure.

6.3.5 Interpretation of stability of α phase in terms of density of states

In figure 6.4, we have shown calculated density of states of α (HCP) and β (FCC) WC at pressures 0, 100 and 200 GPa. Our zero pressure density of state curve of α and β WC are similar to previous calculation results [81] confirming the reliability of our results. The bonding nature of WC in terms of density of states has been discussed in this paper [81] hence we skip that and focus the discussion on the stability of α phase in comparison to β phase at high pressure. We can see that in figure 6.4, α phase has 0.32, 0.24 and 0.21 states/eV/molecule at Fermi level in the DOS curves of 0, 100 and 200 GPa respectively, whereas β WC has 1.14, 0.91 and 0.79 states/eV/molecule. Hence at all pressures DOS of α phase at Fermi level is low as compared to the DOS of β phase. This provides stability to the α phase. We can also see in figure 6.4, that at all pressures DOS of β WC at Fermi level lies in a local maxima whereas DOS at Fermi level of α phase lies in a local minima providing more stability to WC in this phase. Similar nature of DOS at Fermi level has been observed for the FCC phase at ambient condition and for HCP phase at high pressure for Au and Al in [98] and chapter 3 of this thesis respectively. The most interesting thing is that the width of the minima of DOS of α phase at Fermi level increases on increasing pressure, this gives more mechanical stability to this phase at high pressure. Hence from the DOS curves, it is clear that α phase is more stable at high pressure and its stability should increase on increasing the pressure.

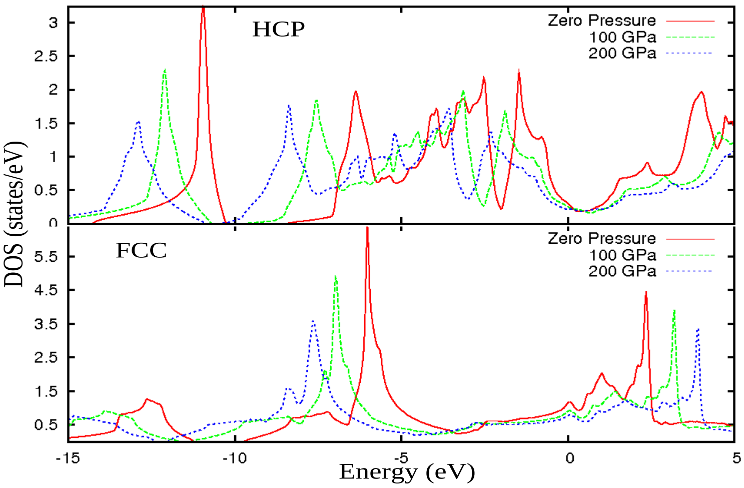

Figure 6.4: Density of states curves of α (HCP) and β (FCC) WC at zero, 100 and 200 GPa

6.3.6 Qualitative discussion on the electrical conductivity of WC

From the calculated density of state of both phases of tungsten carbide, we can attempt to predict its conductive(resistive) behaviour with pressure. For this purpose we use Bloch resistivity formula [142].

$$\rho = \frac{3\pi\hbar Q^6 n^2}{8e^2\epsilon_F D(\epsilon_F)^2 N k_B \theta_D k_F^4}\left(\frac{T}{\theta_D}\right)^5 I_5\left(\frac{\theta_D}{T}\right) \tag{6.15}$$

where ϵ_F is the Fermi energy, $D(\epsilon_F)$ is the density of states (DOS) per unit volume at Fermi energy, θ_D is the Debye temperature, n is the electron density, Q is a phonon wavevector, k_F is the Fermi vector and I_5 is a Debye integral which can be written as

$$I_5(x) = \int_0^x \frac{z^5 e^z}{(e^z - 1)^2} dz \tag{6.16}$$

If we express ϵ_F and k_F in terms of n and $D(\epsilon_F)$, we can rewrite Bloch's formula as

$$\rho = \frac{\pi^2 hbar Q^6 n^2}{4e^2 D(\epsilon_F) k_B \theta_D} \left(\frac{T}{\theta_D}\right)^5 I_5 \left(\frac{\theta_D}{T}\right) \tag{6.17}$$

From equation 6.17, we can see that at a given temperature, the resistivity of a metal correlates inversely with the electronic density of state (DOS) at the Fermi level. From figure 6.4, we can see that the DOS of FCC structure of tungsten carbide at Fermi level is higher than the that of HCP structure at all pressures. Hence we can predict that resistivity of the HCP structure should be larger than that of FCC structure or the electrical conductivity of HCP structure is smaller than electrical conductivity of the FCC structure. Similarly we can also see in figure 6.4, that for both structures the DOS at the Fermi level decreases when pressure is increased. It means that on applying pressure, electrical conductivity of both the structures, decreases.

6.3.7 Grüneisen Coefficient of α and β WC

Grüneisen coefficient Γ is an important parameter of ion - thermal equation of state [9,41]. Grüneisen coefficient is dependent on the density (or on the applied pressure) and is independent of the temperature. It is defined as $\Gamma = \partial \ln \bar{\nu} / \partial \ln V$. $\bar{\nu}$ is the average frequency of the spectrum of the elastic vibrations of the lattice and V is the specific volume. Grüneisen coefficient can be related to the function of cold compression by making an assumption that the average frequency $\bar{\nu}$ is close to the maximum frequency. The magnitude of the maximum frequency $\nu_{\max}$is equal to the ratio of speed of propagation of elastic compression waves c_0 to the minimum wavelength $\lambda_{\min}$. Hence, we can write $\bar{\nu} \sim \nu_{\max} = c_0/\lambda_{\min}$. $\lambda_{\min}$ is of the order of inter-atomic distance ($\lambda_{\min} \sim r_0$). The speed of sound is $c_0 = (-V^2 dp_c/dV)^{1/2}$ and $r_0 = V^{1/3}$. Hence $\bar{\nu} \sim V^{2/3}(-dp_c/dV)^{1/2}$. Logarithmic derivative of this expression gives,

$$\Gamma = \frac{\partial \ln \bar{\nu}}{\partial \ln V} = -\frac{2}{3} - \frac{V}{2}\frac{d^2 p_c/dV^2}{dp_c/dV} \tag{6.18}$$

Equation 6.18 is known as Slater's formula [9]. Using equation 6.18, we have calculated Grüneisen coefficient as a function of cold compression, variation of Grüneisen coefficient with volume is shown in the figure 6.5. Litasov et. al. [34] have reported Grüneisen coefficient at ambient condition, calculated by fitting measured isotherms using three different fitting schemes. The results of their poorly resolved [34] three fittings are 1.44, 1.56 and 1.64 respectively. Our calculated value at zero pressure is $\Gamma_0(cal.) = 1.84$ which is reasonably close to the maximum value of the reported measured value [34]. We tried to fit our calculated Γ as a function of compression (V_0/V) to provide an analytical formula for calculating Grüneisen coefficient for compressed WC. The best - fit which gives similar results as our first principles calculation, can be expressed as $\Gamma = \Gamma_0\,(V/V_0)^{4.3}$.

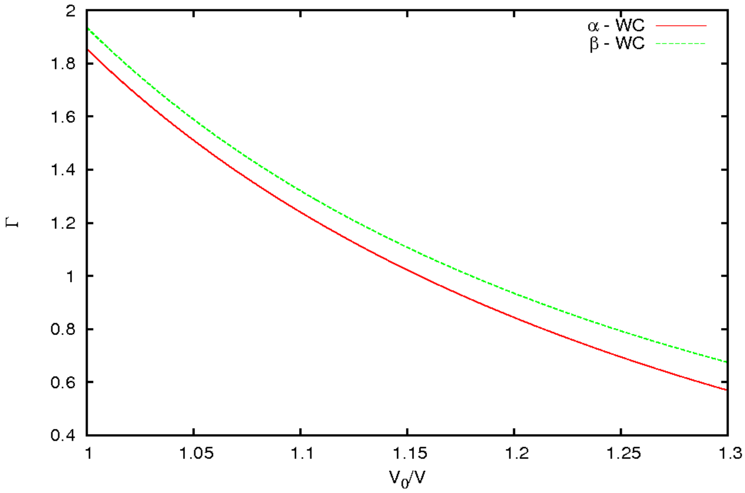

Figure 6.5: Variation of Grüneisen parameter of α and β phases of WC with the variation of the volume.

ELASTIC PROPERTIES

Elastic properties of a material provide information about hardness, brittle/ductile character, anisotropic behaviour and bonding nature of the material. Now we describe the results of the elastic properties and discuss these characters of tungsten carbide. We present the results of pressure dependent elastic constants and discuss anisotropic behaviour of α and β WC in section 6.3.7. In section 6.3.8, we first present the results of elastic moduli and Poisson's ratio and then discuss the brittle/ductile character of tungsten carbide on the basis of these results. Finally we deduce pressure dependent longitudinal and shear velocities, Debye temperature and melting temperature from the calculated elastic properties and present the results in section 6.3.9.

Elastic constants of α and β WC

Table 6.2: The calculated elastic constants of α and β WC; P and C_{ij} are in GPa.

	$\alpha-$WC					$\beta-$WC		
P	C_{11}	C_{12}	C_{13}	C_{33}	C_{55}	C_{11}	C_{12}	C_{44}
Experimental results [130]								
0.0	720.0	254.0	267.0	972.0	328.0			
Our results								
0.0	719.2	215.7	165.8	960.4	315.3	894.3	115.7	124.5
12.1	797.9	250.3	196.2	1067.8	355.2	988.1	138.2	135.2
31.8	920.9	315.8	268.6	1233.2	417.6	1149.5	168.3	149.2
55.9	1026.5	402.3	326.0	1395.0	467.5	1362.1	207.1	165.6
85.5	1145.2	514.1	409.6	1583.2	532.0	1613.4	255.5	182.3
122.1	1295.9	656.9	510.0	1804.9	596.3	1909.2	311.0	202.3

In table 6.2 we have displayed calculated pressure dependent elastic constants C_{ij} of α and β WC phases. We have also given the experimental values [130] of elastic constants of $\alpha-$ WC measured at ambient conditions in table 6.2 for the comparison. These experimental values were determined using high frequency pulse-echo measurements. Elastic constants C_{11},C_{12},C_{33} and C_{55} are in reasonably good agreement with the experimental results for $\alpha-$ WC, only C_{13} shows some discrepancy. It is easy to observe from table 6.2 that elastic constants C_{ij} of both phases increase almost linearly when the pressure is increased.

The Born mechanical stability criteria of hexagonal phase are $C_{11} > 0$, $C_{11} - C_{12} > 0$, $C_{55} > 0$ and $(C_{11} + C_{12})\,C_{33} - 2{C_{12}}^2 > 0$. The calculated independent elastic constants C_{11}, C_{12}, C_{13}, C_{33} and C_{55} of α WC satisfy these stability criteria at all pressures implying that α phase is a mechanically stable phase for tungsten carbide in the pressure range considered here. Similarly, the mechanical stability criteria of cubic phase are: $C_{11} - C_{12} > 0$, $C_{11} + 2C_{12} > 0$ and $C_{44} > 0$. We can see in table 6.2 that all independent elastic constants of β WC are positive and satisfy these criteria implying the mechanical stability of β phase. Hence, α and β both phases are mechanically stable for tungsten carbide.

Now we discuss the anisotropic behaviour of α and β WC. There are three types of anisotropy constants for a hexagonal crystal ΔP, $S1$ and S_2. ΔP corresponds to the anisotropy with respect to compression wave and $S1$ and S_2 correspond to the anisotropy with respect to two shear waves. First shear wave is the wave polarized perpendicular to the basal plane and second is the wave polarized in the basal plane [132]. Anisotropic behaviour of cubic phase is described by the anisotropy constant A. The calculated anisotropy constants of α and β WC are given in the table 6.3. We observe from table 6.3 that for β WC, the anisotropy constant A at zero pressure is much smaller than unity implying highly anisotropic behaviour of β WC. It further decreases on increasing the pressure. We can also observe from table 6.3 that for $\alpha-$WC, the anisotropy constants ΔP and ΔS_2 are larger than unity whereas ΔS_1 is close to unity at zero pressure. This implies that $\alpha-$WC is anisotropic for the compression wave and the shear wave polarized in the basal plane whereas it is isotropic for the shear wave polarized perpendicular to the basal plane at zero pressure. ΔP and ΔS_2 increase on increasing the pressure whereas

ΔS_1 decreases on increasing pressure.

Once the elastic constants at high pressure are determined we would like to compare our results with experiments. Unfortunately comparisons of elastic constants of α and β phases of WC with measured values at high pressure are not possible because there is no measurement of the independent elastic constants C_{ij} of α and β phases of WC at high pressure. However, we can derive elastic properties such as bulk, shear and Young's modulus from the calculated elastic constants and compare them with the available measured values at high pressure. In the following section, we present the results of calculated elastic moduli and their comparison with experimental results.

Table 6.3: The calculated pressure dependent anisotropy constants of tungsten carbide

Pressure (GPa)	ΔP	ΔS_1	ΔS_2	A
0.000	1.335	1.069	1.252	0.319
12.12	1.338	1.037	1.297	0.318
31.79	1.340	0.967	1.383	0.304
55.88	1.359	0.948	1.495	0.286
85.50	1.383	0.897	1.686	0.268
122.90	1.393	0.872	1.866	0.253

6.3.8 Bulk modulus, Shear Modulus and Young's modulus

Direct first principles calculations of bulk, shear and Young's moduli are complicated by the complex nature of the stresses and strains across the grain boundaries separating differently oriented elastically anisotropic crystallites. However, these elastic properties of the polycrystalline aggregate containing randomly oriented crystallites can be deduced from the single crystal elastic constants using Voigt and Reuss approximations. The relations for calculating bulk and shear modulus using Voigt (B_{V} and G_{V}) and Reuss (B_{R} and G_{R}) approximations are given in the section 6.2.3. Bulk modulus B and shear modulus G are calculated by averaging of B_{V} and B_{R}, and G_{V} and G_{R} respectively. The Young's modulus E and Poisson's ratio ν are calculated from the following standard relations:

$$E = \frac{9BG}{3B+G} \quad \text{and} \quad \nu = \frac{3B-2G}{2\,(3B+2G)} \tag{6.19}$$

The calculated B, G, E and ν of both phases of tungsten carbide at different pressures are given in table 6.4. From tables "6.1 of previous chapter" and 6.4 we can see that the bulk modulus B_0 calculated from the elastic constants has nearly same value as the one obtained from the EOS fitting. This might be an estimate of the reliability and accuracy of our calculated elastic constants for α and β tungsten carbide.

Table 6.4: The calculated elastic moduli and Poisson's ratio of α and β WC; P, B, G, and E are in GPa.

	$\alpha-$WC				$\beta-$WC			
P	B	G	E	ν	B	G	E	ν
0.00	377.6	324.9	757.5	0.166	375.2	228.5	569.8	0.246
12.1	426.5	359.1	841.1	0.171	421.5	252.6	631.6	0.250
31.8	517.5	406.8	967.1	0.189	495.4	287.5	722.7	0.256
55.9	595.1	438.1	1055.2	0.204	592.1	330.9	836.9	0.264
85.5	692.6	470.2	1150.3	0.223	708.1	379.7	966.5	0.272
122.1	808.4	501.9	1247.5	0.243	843.7	436.8	1117.5	0.279

To our knowledge no experimental or theoretical data of the bulk modulus and shear modulus of any phase of tungsten carbide have been reported up to the pressure range considered in our calculation. Amulele et. al. [35] have given fitted $B(P)$ and $G(P)$ relations for calculating bulk modulus and shear modulus of $\alpha-$ WC using their experimental data up to 14 GPa. These experimental results were determined from the ultrasonic measurements in the multi anvil high pressure apparatus. The fitted relations for bulk and shear modulus are $B = 2.3865P + 382.92$ and $G = 1.8652P + 301.55$ respectively [35]. Here B, G and P are in GPa and have their usual meanings. Although these relations have been given using very small range of pressure but we have extrapolated them up to 120 GPa to compare the variation of bulk and shear modulus with pressure obtained in our calculation. In figure 6.6 we have plotted our results along with the extrapolated experimental results and we find reasonably good agreement in calculated and experimental shear modulus. In the pressure range of 0-14 GPa calculated bulk modulus also shows reasonably good agreement with the experimental bulk modulus. Above this pressure calculated bulk modulus shows a deviation, maximum deviation is up to 20 %. The deviation is reasonable as this relation has been fitted using B(P) data upto P = 14 GPa only [35] whereas we are making comparison upto 120 GPA. Hence our calculations predict that at very high pressure ($P > 14$ GPa) the variation of bulk modulus with pressure will not behave as described by this relation [35].

In figure 6.7, we have plotted the variation of the ratio G/B with the variation of the pressure. From this figure we can see that ratio of shear to bulk modulus (G/B) of both phases of WC are smaller than 1.0, it means that resistance to bond - length change exceeds to resistance to bond angle change in WC. G/B value of a material is also associated with the brittle or ductile character of the material. Low value is associated with ductility, the materials having G/B value smaller than 0.57 are ductile and materials with G/B value larger than 0.57 are brittle [135]. At zero pressure, The G/B value of α and β WC are 0.86 and 0.61 respectively, implying that WC is a brittle material in both phases. β WC is less brittle and becomes ductile at 46 GPa. On increasing the pressure, the G/B value of α phase

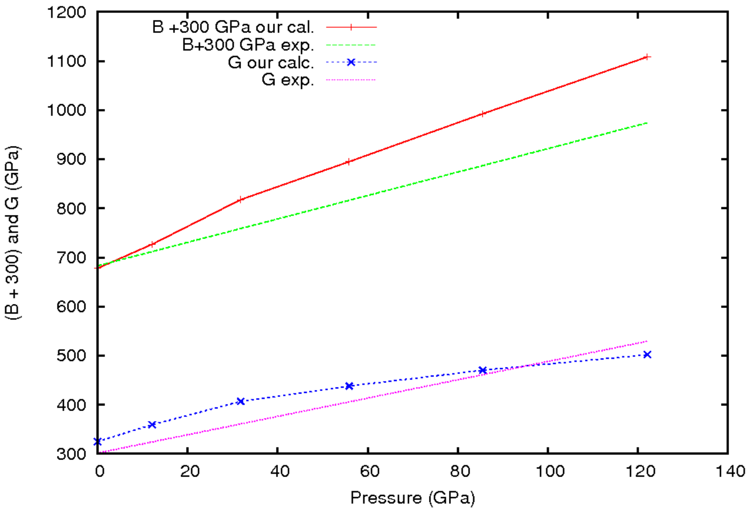

Figure 6.6: Bulk modulus and Shear modulus of WC. To allow plotting in the same figure curve of bulk modulus has been shifted up by 300 GPa. The experimental values have been extrapolated using the linear fits given in [35].

also decrease but it remains above the critical value of 0.57 implying that WC shows tendency towards ductility on increasing the pressure but remains brittle up to 120 GPa. Brittle character of WC is also confirmed by its low value of Poisson ratio. It is believed that the materials with low Poisson's ratio are brittle [136] for example brittle metals with BCC structure have low value of Poisson's ratio whereas ductile FCC metals have high Poisson's ratio [137]. The critical value of Poisson's ratio for separating brittle materials from ductile materials is $1/3$, the brittle materials have Poisson's ratio smaller than this value. Young's modulus, also known as the tensile modulus, is defined as the ratio of uniaxial stress and uniaxial strain. It is a measure of the stiffness of the solid [138]. The large value of the Young's modulus of WC shows that it is a very stiff material.

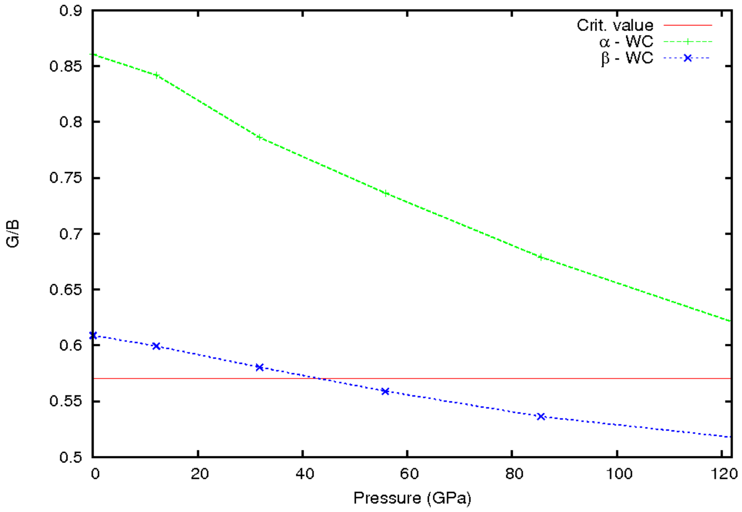

Figure 6.7: Variation of ratio of shear to bulk modulus (G/B) of α and β WC with pressure (P).

6.3.9 Debye Temperature

The Debye temperature is an important parameter of a solid for calculating the lattice contribution to the equation of state due to thermal excitations [9, 41]. Debye temperature depends on the sound speed in the solid and can be calculated by using following formula [139]:

$$\Theta = \frac{h}{k}\left[\frac{3q}{4\pi}\frac{N\rho}{M}\right]^{\frac{1}{3}} v_{\mathrm{m}} \tag{6.20}$$

where h is plank constant, k is Boltzmann's constant, N is Avogadro number, M is the molecular weight of WC, q is the number of atoms in the formula of the solid compound i. e. 2 in this case. Here v_{m} is the sound speed which can be calculated using following relation:

$$v_{\mathrm{m}} = \left[\frac{1}{3}\left(\frac{2}{{v_{\mathrm{s}}}^{3}} + \frac{1}{{v_{\mathrm{l}}}^{3}}\right)\right]^{\frac{-1}{3}} \tag{6.21}$$

where v_s and v_l are shear and longitudinal sound velocities. The probable values of these velocities can be calculated using following relations:

$$v_\mathrm{s} = \surd(G/\rho) \quad v_\mathrm{l} = \surd(B + 4/3G)\,/\rho \tag{6.22}$$

these velocities can be easily determined using the calculated values of bulk modulus and shear modulus. Amulele et. al. [35] have given the fitted relations for longitudinal and transverse sound velocities as a function of pressure. These relations are also fitted using the experimental data in the pressure range of 0-14 GPa as done for bulk and shear modulus. The fitted relations for longitudinal and transverse velocities are $V_\mathrm{p} = 0.0122P + 7.0993$ and $V_\mathrm{s} = 0.075P + 4.4002$ respectively. Here velocities are in km/s and P is in GPa. We have extrapolated longitudinal and transverse velocities up to 120 GPa in the similar way as we have done for the bulk modulus and the shear modulus and compared calculated results with these extrapolated experimental results. The comparison is shown in the figure 6.8. We find reasonably good agreement between calculated velocities and extrapolated experimental velocities.

Melting temperature can be calculated using Lindemann's melting law [23]. This law relates the melting temperature $T_\mathrm{m}(V)$ to the Debye temperature $\Theta(V)$, which characterizes the quantum effects in low temperature lattice vibration:

$$T_\mathrm{m} = \delta \times V^{2/3}\Theta^2(V) \tag{6.23}$$

The constant δ depends upon the material and can be assumed independent of density and temperature. Hence this constant can be estimated by using the experimental melting temperature of WC at atmospheric pressure. Density dependent melting temperature of Al have been calculated in similar way [51]. For

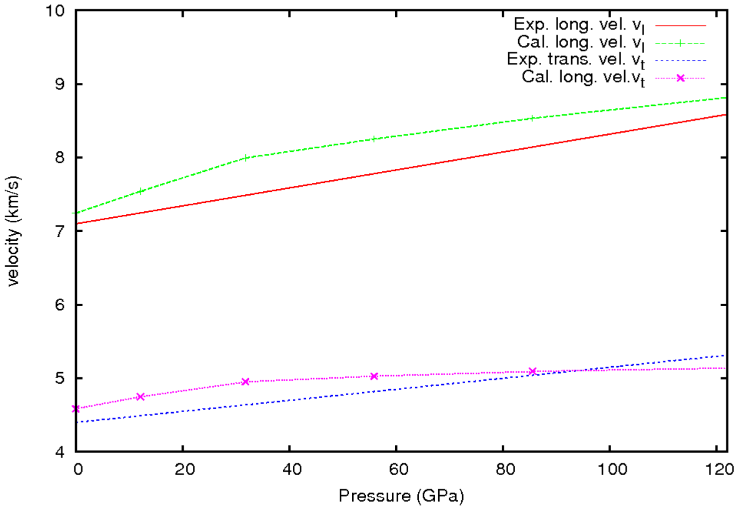

Figure 6.8: Variation of longitudinal and shear velocities with the variation of pressure for α WC. The experimental values have been extrapolated using the linear fits given in the [35]

calculating δ of both phases we have used experimental melting temperature of α−WC (T_m = 2800K [140]).

Table 6.5: Calculated Debye temperature and Melting temperature of α and β WC

	$\alpha - WC$		$\beta - WC$	
P(GPa)	Θ(K)	T_m(K)	Θ(K)	T_m(K)
0.00	686	2800	580	2800
12.1	718	3008	607	3003
31.8	760	3282	643	3284
55.9	784	3396	686	3621
85.5	808	3499	730	3979
122.1	830	3578	777	4371

We have displayed the variation of Debye temperature and melting temperature of α and β WC with the variation of pressure in the table 6.5. Experimental value of Debye temperature at ambient condition is 665 K [141] which is in good agreement with the value (687 K) obtained in our calculation for zero temperature and pressure. The Debye temperatures of both phases of WC increase monotonically on increasing the pressure. To our knowledge experimental or theoretical data of Debye temperature and melting temperature at high pressure are not reported in the literature. Hence comparison of our results with experiments is not possible.

6.4 Conclusion

We presented results of first principles calculations of equation of state, lattice parameters and elastic properties of α and β WC at high pressure. Calculated volume, bulk modulus and pressure derivative of bulk modulus at zero pressure are in good agreement with the reported experimental values. Calculated pressure dependent lattice parameters of α WC are in reasonably good agreement with reported experimental results. Calculated $P - V$ isotherm at zero temperature shows good agreement with reported experimental isotherm. High pressure structural transformation have been investigated and have been found that α phase remains stable up to a pressure of 350 GPa. The stability of α phase over β phase has been discussed in terms of density of states. From the nature of DOS at Fermi level it has been found that the stability of α phase increases with respect to the stability of β phase on increasing pressure. Grüneisen coefficient deduced from the $P - V$ isotherm at zero pressure shows reasonably good agreement with the reported experimental value. Density dependent Grüneisen coefficient of α and β WC has also been calculated and a fitted relation for $\Gamma(V)$ has been provided. Elastic properties of α and β WC at high pressure have been calculated. The mechanical stability and the anisotropic behaviour of α and β WC have been discussed in terms of the calculated elastic constants. Pressure dependent shear modulus and sound velocities (shear and longitudinal) of α WC are in reasonably good agreement with the reported experimental results. Bulk modulus shows deviation from the extrapolated experimental results at high pressure. Brittle nature of WC has been discussed using G/B and Poisson ratio.

7

Conclusions

In this thesis, we have presented our work dealing with the calculation of the Equation of State and structural properties of two different materials. The first is the metallic element Aluminium (Al) and the second is the ceramic compound tungsten carbide (WC). Aluminium is of importance in pulsed-power experiments, such as electromagnetic liner acceleration and electrically-exploded foils. For Al, using a variety of theoretical techniques, we have generated EOS data valid over several orders of magnitude in density and temperature. We have also studied structural phase transformations occurring at high pressures.

Tungsten carbide is important because of its applications in industrial machinery and high-pressure systems. We present, for the first time, theoretical calculations of EOS and elastic properties of tungsten carbide at high pressures.

For aluminium, we have also computed the electrical conductivity as a function of temperature & density.

7.1 Structural phase transformations in Al

1. **Structural properties at ambient condition**

   To determine which option for the exchange-correlation functional is the most suitable for our purposes, we compared certain zero pressure properties viz., the lattice constants and the bulk modulus calculated by using GGA and LDA with their experimental values. The ground-state properties of the three phases of Al were obtained using the calculations of the total energy (E) as a function of volume (V) at lower pressures. E versus V data was then fitted to the Birch-Murnaghan equation of state to obtain lattice parameters and bulk modulus at zero pressure. Calculated GGA and LDA lattice parameters and bulk modulus were compared with experimental values and it was found that GGA results are more accurate. Hence in our subsequent calculations, we used GGA E versus V results.

2. **c/a ratio for HCP structure**

   We are interested in structural transformations in FCC, HCP and BCC structures of Al at high pressures. For FCC and BCC, the only adjustable parameter is a. For HCP, however, the ratio c/a must also be specified. Hence it is first necessary to determine the c/a ratio that minimizes system energy at a given volume V/V_0. Hence the c/a ratio was varied from 1.45 to 1.8 over a range of densities. We have found that for densities near normal, the energy is minimum for a c/a ratio that deviates by 2% from the experimental value of 1.6139. Near the FCC-HCP transition and at higher densities, the energy was minimum for c/a = 1.623.

3. **Lattice constants at high pressure**

   We have also calculated lattice constants at higher pressures and compared the results with those obtained in recently reported X-ray powder diffraction experiments [62]. Our calculations show good agreement with experimental values, the percentage errors lying within 0.5% in the calculated results for ‘a’ (FCC and HCP), and within 0.4% for ‘c’ (HCP). Errors do not show any definite trend with the pressure. This is the first theoretical calculation of lattice parameters at high pressures.

4. **Total energy as function of Volume**

   To find the volumes at which structural transformations take place, we have compared the total energy vs. volume curves of FCC, HCP and BCC structures. The differences (Δ) between the energies of FCC-HCP, FCC-BCC, and HCP-BCC were calculated and plotted as a function of the volume to determine the transition volume. From this plot we observe that the FCC-HCP transition occurs at $0.53V_0$. Experimentally, however, this transition has been found to lie at $0.509V_0$. The reason for this difference could be that $\Delta_{FCC-HCP}$ is negligibly small (of the order of 10^{-4} Ry) over the range V/V_0 = 0.51-0.53. It becomes significant $\sim$0.9 mRy at $V/V_0 = 0.5089$ and becomes 1 mRy when V/V_0 reaches 0.50. Such a small difference between the energies of FCC and HCP structures around the phase transition point could be the reason for the co-existence of the FCC and HCP structures over a wide range of densities.

5. **Pressure vs. enthalpy**

   For determining the FCC-HCP and HCP-BCC transition pressures, the differences between the enthalpies of FCC-HCP, FCC-BCC, and HCP-BCC were calculated and plotted as functions of the pressure. We find FCC - HCP transition pressure at 178 GPa whereas the reported experimental value is

217 ± 10 GPa. This difference could be due to two reasons. Firstly, we have not included the energy contribution of zero point vibration. Secondly, there is a negligibly small difference between FCC and HCP enthalpies (1 mRy) in the pressure range of 178 - 217 GPa, hence there is a possibility that in the experiment the structural transformation may not be noticed until the enthalpy difference becomes significant.

6. **Density of states vs. Volume (Pressure)**
   The density of states (DOS) of FCC and HCP structures of Al has been calculated for normal and high pressures. It has been found that the DOS of both structures at normal conditions shows different kind of nature near the Fermi level but become similar over a range of compressed volumes close to the FCC-HCP transition volume ($V/V_0 = 0.53$). At ambient conditions, the DOS of FCC exhibits a a local minimum at the Fermi energy, whereas the DOS for HCP does not exhibit this feature. At high pressures, the DOS of both structures exhibits local minima at the Fermi energy, implying that both structures are stable. This similarity can be one reason for the reported coexistence of FCC-HCP phases over a wide range of compressions near the FCC-HCP phase transition.

Hence, the work reported in this chapter not only gives the cold-curve (zero-temperature isotherm) of the EOS of Al, but also provides information about the possible structural transformations and the underlying physical reasons.

7.2 Ab-initio calculations of EOS and conductivity of Al in expanded states

In this chapter, we present results of ab-initio molecular dynamics simulations of EOS and electrical conductivity of aluminium in rarefied states. We have also given QEOS results in this chapter. We have compared the QEOS cold-curve with the FP-LAPW cold-curve and found good agreement. However, AIMD results do not agree with the QEOS results in the rarefied region. Hence we conclude that QEOS needs to be corrected in this region.

From a plot of DC electrical conductivity σ (T) with temperature, we noticed that there is a change of slope at a certain temperature – for example, the slope decreases above 6000 K at a density of 2.35 g/cc. We have explained this using the Drude theory of electrical conductivity. According to this theory, electrical conductivity depends upon the number density of electrons at Fermi level n, and on the relaxation time τ. Hence, at low temperatures, the conductivity decreases rapidly with increasing temperature. This can be explained as follows - the ions vibrate about their equilibrium positions, which leads to thermal vibration of the crystal lattice. The amplitude of the vibrations increases as temperature is increased. The electrons are scattered by collisions with the lattice ions. Consequently, with the increase in the amplitude of vibration, the collision frequency increases. This leads to decrease in the relaxation time τ, and hence to decrease in the electrical conductivity. At high temperatures ($>$ 6000 K), even though the relaxation time is still decreasing with the temperature leading to decrease in the conductivity, the number density of electrons near the Fermi level also starts increasing, causing a net increase in the conductivity. Both these phenomena, viz., the decrease in the relaxation time and the increase in the number density of electrons near Fermi level jointly lead to less decrease in the electrical conductivity above the temperature 6000 K as compared to below this temperature. Hence, we see a break in the slope near 6000 K. This explanation has been given for the first time. However, further studies should be performed to confirm this explanation.

7.3 Improvement in QEOS model and determination of Al EOS for compressed and expanded states

In Chapter 4, we concluded that AIMD and QEOS results do not agree in the rarefied region. Also, although FP-LAPW and QEOS cold-curves show good agreement, QEOS uses a cold curve which is obtained by applying a semi-empirical binding correction to the zero temperature Thomas-Fermi model, which is a crude way of calculating the cold-curve. In this work, we have developed an improved version of the QEOS algorithm, with the incorporation of DFT results, FP-LAPW as well as AIMD.

In the improved version of QEOS, we have replaced the QEOS cold curve by the FP-LAPW cold curve for compressed Al. In rarefied states, we have replaced the cold curve by a soft-sphere function, adjusting the parameters such that the isotherms yielded by the improved QEOS show good agreement with AIMD isotherms in the rarefied region. This improved QEOS model is validated in compressed states by deriving $P-\rho$ and U_s-U_p hugoniots and comparing them with available experimental results. Good agreement has been found. In expanded states, this EOS model is validated by comparing P(E) along the isochores with the reported experimental curves and thermodynamic properties at the critical point with their published values. Good agreement is found.

7.4 Ab-initio calculation of EOS and elastic properties of WC at high pressures

In this chapter, we have studied structural properties, EOS, and elastic properties of HCP (α phase) and FCC (β phase) structures of tungsten carbide. Important results are summarized below.

1. *Structural properties, P-V isotherm and Gruneisen parameter:*

   Calculated volume dependent total energy data of Îś and Îš tungsten carbide have been fitted to the Birch-Murnaghan EOS to obtain molecular volume (V_0), bulk modulus (B) and its pressure derivative (B_P). The calculated values are in good agreement with reported XRD and ultrasonic experimental values. The calculated $P-V$ isotherm at zero pressure is also in good agreement with reported experimental isotherms. As α tungsten carbide is hexagonal, its c/a value has been optimized at each volume, as was done in the case of Al. The c/a ratio of α-WC increases with increasing pressure. The calculated lattice parameters at high pressures have been compared with experimental values and reasonably good agreement has been found. The density dependent Gruneisen parameter has been deduced from the $P-V$ isotherm using Slater's formula.

2. *Elastic properties and Mechanical stability:*

   The α-phase, being an HCP structure, has five independent elastic constants, whereas the β phase, being an FCC structure, has only three independent elastic constants. We have calculated these constants by creating strains in the crystals by distorting them from their original shape. Experimental results are available only for the α phase, and that too for zero pressure. Our results show reasonably good agreement with reported experimental results. We have observed that elastic constants C_{ij} of both phases increase almost linearly when the pressure is increased.

The Born mechanical stability criteria of hexagonal phase are $C_{11} > 0$, $C_{11} - C_{12} > 0$, $C_{55} > 0$ and $(C_{11} + C_{12})\, C_{33} - 2{C_{12}}^2 > 0$. The calculated independent elastic constants C_{11}, C_{12}, C_{13}, C_{33} and C_{55} of α WC satisfy these stability criteria at all pressures implying that α phase is a mechanically stable phase for tungsten carbide in the pressure range considered here. Similarly, the mechanical stability criteria of cubic phase are: $C_{11} - C_{12} > 0$, $C_{11} + 2C_{12} > 0$ and $C_{44} > 0$. We have found that all independent elastic constants of β WC are positive and satisfy these criteria implying the mechanical stability of β phase. Hence, both α and β phases are mechanically stable for tungsten carbide.

3. *Brittle vs. ductile character:*

   Elastic properties such as bulk, shear and Young's modulus have been calculated upto a pressure of 120 GPa. The reported experimental data is available up to only 14 GPa. Our results are in good agreement with reported experimental data. We have found that the ratio of shear to bulk modulus (G/B) of both phases of WC is smaller than 1.0. This means that resistance to bond-length change exceeds the resistance to bond angle change in WC. The G/B value of a material is also associated with the brittle or ductile character of the material, a low value (<0.57) being a criterion with ductility. At zero pressure, the G/B values of α and β WC are 0.86 and 0.61 respectively, implying that WC is a brittle material in both phases. β WC is relatively less brittle and becomes ductile at 46 GPa. On increasing the pressure, the G/B value of the α phase also goes down but it remains above the critical value of 0.57, implying that WC shows a tendency towards ductility on increasing the pressure but remains brittle up to 120 GPa. The brittle character of WC is also confirmed by its low value of Poisson ratio.

The pressure-dependent sound velocities (shear and longitudinal) have been calculated from the elastic properties up to 120 GPa. These velocities show good agreement with reported experimental data. Pressure-dependent Debye and melting temperatures have been also deduced from the calculated sound velocities up to 120 GPa.

Bibliography

[1] S. K. Sikka, *National Academy Science Letters* **35**, (2012) 65-70.

[2] W. J. Nellis, *Phys. Rev. B* **82**, (2010) 092101.

[3] G. I. Kanel, W. J. Nellis, A. S. Savinykh, S. V. Razorenov, A. M. Rajendran, *J. Appl. Phys.* **106**, (2009) 043524.

[4] Jamal Uddin and Gustavo E. Scuseria, *Phys. Rev. B* **72** (2006) 035101.

[5] R. Yu, Q. Zhan and X. F. Zhang, *Appl. Phys. Lett.* **88** (2006) 051913.

[6] W. Chen, J. Z. Jiang, *J. Alloys. Compd.* **499** (2010) 243.

[7] WeiHu Li, *J. Alloys Compd.* **537** (2012) 216.

[8] S. K. Sikka, B. K. Godwal and R. Chidambaram, *Equation of State at high pressure Shock Compression of Solids III.* Springer New York (1997) 1-35.

[9] S. Eliezer, A. Ghatak and H. Hora, *An Introduction to Equations of State: Theory and Applications* Cambridge University Press (1986)

[10] R M More, K H Warren, D A Young, and G B Zimmerman 1988 *Phys. of Fluids* **31** 3059

[11] G. I. Kerley, *Sandia National Laboratories Report* **No. SAND88-229175** (1991)

[12] Degnan et. al. *Phys. Rev. Lett.* 1995 **74** 1.

[13] P. V. Subhash, S. Madhavan, N. Sakthivel, P. Pahari, V. Mishra, A. Majalee and S. Chaturvedi, *Plasma Physics and Controlled Fusion* **53** (2011) 085013.

[14] A V Majalee, V Mishra, P Pahari, V R Ikkurthi and S. Chaturvedi Nov. 2008 *Proceedings of Indo Russian Workshop on High Energy Density Physics Dynamics* I2IT Pune India

[15] A. K. Saxena, T. C. Kaushik and Satish C. Gupta, *Rev. Sci. Instr.* **81** (2010) 033508 $(1-9)$.

[16] F.D. Murnaghan, *Proc. Natl. Acad. Sci. USA* **30** (1944) 244.

[17] S. K. Sikka and B. K. Godwal, *Nucl. Phys. and Sol. State Phys.* **24C** (1981) 19.

[18] Charles Kittel *Eighth edition: Introduction of Solid State Physics*

[19] B. Ya. Zeldovich and Yu. P. Raizer *Physics of Shock waves and High Temperature Hydrodynamic Phenomena*, Academic New York (1966).

[20] R. Grover, *J. Chem. Phys.* **55** (1971) 3435.

[21] M. Baus and J. P. Hansen, *Phys. Rep.* **59** (1980) 1.

[22] W. G. Hoover, G. Stell, E. Goldmark and G. Degani, *J. Chem. Phys.* **63** (1975) 5434.

[23] N. F. Mott and N. F. Jones *Theory of the Properties of Metals and Alloys*, Dover, New York (1958).

[24] R. P. Feynman, N. Metropolis and E. Teller, Phys. Rev. **75** (1949) 1561. John Wiley and Sons, United States of America (2005)

[25] Richard M. Martin, *Electronic Structure: Basic Theory and Practical Methods* Cambridge University Press, (2008).

[26] S. Cottenier, *Density functional theory and the family of (L) APWmethods: a step-by-step introduction*, Institute voor Kern- en Stralingsfysica, KU Leuven, Belgium, 2002, ISBN 90-807215-1-4 to be found at http://www.wien2k.at/reg-user/textbooks.

[27] John F. Dobson, Giovanni Vignale and Mukunda P. Das, *Electronic density functional theory : recent progress and new directions*, Plenum Press, New York (1998).

[28] G. P. Das *Introduction to linear band structure methods* in *'Electronic structure of Alloys, Surfaces and Clusters'*, Eds. A. Mookerjee and D.D. Sarma (Taylor & Francis, London and New York 2003), pp. 22-70.

[29] B. K. Godwal, R. S. Rao, A. K. Verma, M. Shukla, H. C. Pant and S. K. Sikka, *Laser and Particle Beams*, **21** (2003) 523-528,

[30] Michel Pénicaud 2009 J. phys. : Cond. Matter **21** 0954091.

[31] W. A. Harrison, *Solid State Theory* (Mc Graw-Hill, New York, 1970)

[32] G. D. Mahan, *Many Particle Physics* (Plenum, New York, 1981)

[33] J. Callaway, *Quantum Theory of Solid State* (Academic, New York, 1974)

[34] Konstantin D. Litasov, Anton Shatskiy, Yingwei Fei, Akio Suzuki, Eiji Ohtani et. al.

[35] George Amulele, Murli H Manghnani, Sekar Marriappan, Xinguo Hong and Fengug Li. *J. Appl. Phys.* **103** (2008) 113522.

[36] A. V. Bushman, I. V. Lomonosov, and V. E. Fortov, *Sov. Tech. Rev. B Therm. Rev.* **5** (1993) 1.

[37] A. V. Bushman, G. I. Kanel, A. L. Ni and V. E. Fortov *Thermophysics and Dynamics of Intense Pulse Loadingis* London: Taylor and Fransis.

[38] V. E. Fortov and I. T. Yakubov, *Physics of Nonideal Plasmas*, London: World Scientific Publishing Co. (1999).

[39] M. Ross, *Rep. Progr. Phys.* **48**, (1985) 1-52.

[40] E. D. Chisolm, S. D. Crockett and D. C. Wallace, *Phys. Rev. B* **68** (2003) 04103-1-04103-12.

[41] I. V. Lomonosov, *Laser and Particle beams* **25** (2007) 567.

[42] David A Young and Ellen M Corey 1995 *J. Appl. Phys.*, **78**, 3748.

[43] A. Ray, M. K. Srivastav, G. Kondayya and S. V. G. Menon *Laser and Part. Beams* **24**, (2006) 437-445.

[44] C. Friedii, N.W. Ashcroft, *Phys. Rev. B* **12** (1975) 5552.

[45] J.C. Duthie, D.G. Pettifor, *Phys. Rev. Lett.* **38** (1977) 564.

[46] J.A. Moriarty, A.K. McMahan, *Phys. Rev. Lett.* **48** (1981) 809.

[47] P.K. Lam, L. Cohen, *Phys. Rev. B* **27** (1983) 5986.

[48] J.C. Boettger, S.B. Trickey, *Phys. Rev. B* **29** (1984) 6434.

[49] J.C. Boettger, S.B. Trickey, *Phys. Rev. B* **51** (1995) 15623.

[50] J.C. Boettger, S.B. Trickey, *Phys. Rev. B* **53** (1996) 3007.

[51] G.V. Sin'ko, N.A. Smirnov, *J. Phys.: Condens. Matter* **14** (2002) 6989.

[52] B. Chimier, V. T. Tikhonchuk and L. Hallo, *Phys. Rev. B* **75** (2007) $195124(1-11)$.

[53] Vanina Recoules and Jean-Paul Crcombett, *Phys. Rev. B* **72** (2005) 10420.

[54] P. Renaudin, C. Blancard, J. Clérouin, G Faussurier, P. Noiret and V. Recoules, *Phys. Rev. Lett.* **91** (2003) 075002$(1-4)$.

[55] S. Mazevet, M. P. Desjarlais, L. A. Collins, J. D. Kress and N. H. Magee, *Phys. Rev. E* **71** (2005) 016409.

[56] M P Desjarlais, J D Kress and L A Collins 2002 *Phys. Rev. E* **66** 025401

[57] V. N. Korobenko and A. D. Rakhel, *Phys. Rev. B* **75** (2007) 064208.

[58] Jean Clérouin, Pierre Noiret, Victor N. Korobenko and Anatoly D. Rakhel, *Phys. Rev. B* **78** (2008) 224203.

[59] P. R. Levashov, G. V. Sin'ko, N. A. Smirnov, D. V. Minakov, O. P. Shemyakin and K. V. Khihchenko, *J. Phys.: Condens. Matter* **22** (2010) 505501.

[60] A. Dewaele, P. Loubeyre and M. Mezouar, *Phys. Rev. B* **70**, (2004) 094112.

[61] R.G. Greene, H. Luo, A.L. Ruoff, *Phys. Rev. Lett.* **73** (1994) 2075.

[62] Y. Akahama, M. Nishimura, K. Kinoshita, H. Kawamura, Y. Oshishi, *Phys. Rev. Lett.* **96** (2006) 045505.

[63] C. E. Ragan, M. G. Silbert, and B. C. Diven, *J. Appl. Phys.* **48**, (1977) 2860.

[64] C. E. Ragan, *Phys. Rev. Ser. A* **29**, (1984) 1391-1402.

[65] L. V. Al'tshuler, A. A. Bakanova, I. P. Dudoladov, E. A. Dynin, R. F. Trunin and B. S. Chekin *J. Appl. Mech. Techn. Phys.* **22**i, (1981) 145-169.

[66] V.A. Bushman, I.K. Krasyuk, P.D. Pashiniy, A.M. Prokhorov, V.Y. Ternovoi, V.E. Fortov, *JETP Lett.* **39** (1984) 411.

[67] Th. Loer, R. Sigel, K. Eidmann, I.B. Foldes, S. Huller, J. Massen,G.D. Tsakiris, S. Witkowski, W. Preuss, H. Nishimura, H. Shiraga, Y. Kato, S. Nakai, T. Endo, *Phys. Rev. Lett.* **72** (1994) 3186.

[68] V.A. Simonenko, N.P. Voloshin, A.S. Vladimirov, A.P. Nagibin, V.N. Nogin, V.A. Popov, V.A. Vasilenko, Yu.A. Shoidin, *Sov. Phys. JETP* **61** (1985) 869.

[69] C. N. Danson, P. A. Brumitt, R. J. Clarke, I. Collier, B. Fell, A. J. Frackiewicz, S. Hawkes, C. Hernandez-Gomez, P. Holligan, M. H. R. Hutchinson, A. Kidd, W. J. Lester, I. O. Musgrave, D. Neville, D. R. Neely, P. A. Norreys, D. A. Pepler, C. Reason, W. Shaikh, T. B. Winstone, R. W. W. WYATT and B. E. Wyborn, Laser Part. Beams **23**, (2005) 23-30.

[70] K. Jungwirth, Laser Part. Beams **23**, (2005) 177-182.

[71] D. H. H. Hoffmann, V. E. Fortov, I. V. Lomonosov, V. Mintsev, N. A. Tahir, D. Varentsov, J. Wieser, Phys. Plasmas **9**, (2002) 3651.

[72] D. H. H. Hoffmann, A. Blazevic, P. Ni, O. Rosmez, M. Roth, N. A. Tahir, A. Tauschwitz, S. Udrea, D. Varentsov, K. Weyrich, and Y. Maronn, Laser Part. Beams **23**, (2005) 47.

[73] T. Sasaki, Y. Yano, M. Nakajima, T. Kawamura and K. Horioka, Laser Part. Beams **24**, (2006) 371-380.

[74] T. Desai, R. Dezulian and D. Batani, Laser Part. Beams **25**, (2007) 23-30.

[75] W.J. Nellis, J.A. Moriarty, A.C. Mitchel, M. Ross, R.G. Dandrea, N.W. Ashcroft, N.C. Holmes, R.G. Gathers, *Phys. Rev. Lett.* **60** (1988) 1414.

[76] A.C. Mitchel, W.J. Nellis, *J. Appl. Phys.* **52** (1981) 3363.

[77] A D Chijioke, W J Nellis, and Isaac F Silvera 2006 *J. Appl. Phy.* **98** 075261

[78] V. P. Zhukov, V. A. Gubanov and T. Jarlborg, *J. Phys. Chem. Solids* **46** (1985) 1111.

[79] V. P. Zhukov and V. A. Gubanov, *Sol. State. Comm.* **56** (1985) 51.

[80] Amy Y. Liu, M. Wentzcovitch, and Marvin L. Cohen, *Phys. Rev. B* **38** (1988) 9483.

[81] David L. Price and Bernard R. Cooper, *Phys. Rev. B* **39** (1988) 4945.

[82] K. Gschneidner et al., *Nat. Mater.* **2** (2003) 587.

[83] D. V. Suetin, I. R. Shein and A. L. Ivanovskii *J. Phys. Chem. Solids* **70** (2009) 64.

[84] W. Kohn and L. J. Sham, *Phys. Rev.* **140**, (1965) A1133.

[85] L. J. Sham and W. Kohn, *Phys. Rev.* **145** (1966) 561.

[86] Parr Robert, G Yang Weitao; *Density-Functional Theory of Atoms and Molecules* Oxford: Oxford University Press (1994) .

[87] J.P. Perdew, J.A. Chevary, S.H. Vosko, K.A. Jackson,

[88] J.P. Perdew, S. Burke, M. Ernzerhof, *Phys. Lett.* **77** (1996) 3865.

[89] J.P. Perdew, P. Ziesche, H. Eschrig (Eds.), *Electronic Structure of Solids* 91, Akademic-Verlag, Berlin, 1991.

[90] J.P. Perdew, *Physica B* **172** (1991) 1.

[91] J.P. Perdew, Y. Wang, *Phys. Rev. B* **45** (1992) 13244.

[92] P. Blaha, K. Schwarz, G.K.H. Madsen, D. Kvasnika, J. Luitz, *WIEN2k, An Augmented Plane Wave Plus Local Orbital Program for Calculating Crystal Poperties*, Karlheinz Schwarz, Technical Universität, Wien, Austria, ISBN 3-9501031-1-2,2001.

[93] X. Gonze, B. Amadon, P.-M. Anglade, J.-M. Beuken, F. Bottin, P. Boulanger, F. Bruneval,' D. Caliste, R. Caracas, M. Cote, T. Deutsch, L. Genovese, Ph. Ghosez, M. Giantomassi, S. Goedecker, D.R. Hamann, P. Hermet, F. Jollet, G. Jomard, S. Leroux, M. Mancini, S. Mazevet, M.J.T. Oliveira, G. Onida, Y. Pouillon, T. Rangel, G.-M. Rignanese, D. Sangalli, R. Shaltaf, M. Torrent, M.J. Verstraete, G. Zerah, J.W. Zwanziger, *Computer Phys. Commun.* 2009, **180**, 2582-2615.

[94] X. Gonze, G.-M. Rignanese, M. Verstraete, J.-M. Beuken, Y. Pouillon, R. Caracas, F. Jollet, M. Torrent, G. Zerah, M. Mikami, Ph. Ghosez, M. Veithen, J.-Y. Raty, V. Olevano, F. Bruneval, L. Reining, R. Godby, G. Onida, D.R. Hamann, and D.C. Allan. Zeit. Kristallogr. 2005, **220**, 558-562.

[95] The ABINIT code is a common project of the UniversitÃľ Catholique de Louvain, Corning Incorporated, and other contributors (URL http://www.abinit.org.

[96] G. Kresse and J. Hafner, *Phys. Rev. B* **47**, (1993) 558.

[97] G. Kresse and J. Furthmuller, *Phys. Rev. B* **54**, (1996) 11169.

[98] Rajeev Ahuja, Sandeep Rekhi, Borje Johansson,

[99] N Troullier and J L Martins 1991 *Phys Rev B* **43** 1993

[100] Chris J. Pickard and R. J. Needs, *Nature Mater.* **9** (2010) 2624.

[101] B. K. Godwal, S. K. Sikka and R. Chidambaram, *Phys. Rev. Lett.*, 47 (1981) 1144-1147

[102] A V Bushman I V Lomonosov and K V Khishchenko *K V Shortwaves Database* http://teos.fisp.ac.ru/rusbank

[103] A. Khein, D.J. Singh, C.J. Umrigar, *Phys. Rev. B* **51** (1995) 4105

[104] H. Arabi, A. Pourghazi, F. Ahmadian, Z. Nourbakhsh, *Physica B* **373** (2006) 16.

[105] R.O. Jones, O. Gunnarsson, *Rev. Mod. Phys.* **61** (1989) 689. M.R. Pederson, D.J. Singh, C. Fiolhhais, *Phys. Rev. B* **46** (1992)6671.

[106] M.Q. Cai, Y.-J. Zhang, Z. Yin, M.-S. Zhang, *Phys. Rev. B* **72** (2005) 075406.

[107] A. Chahed, O. Benhelal, S. Laksari, B. Abbar, B. Bouhafs, N. Amrane, *Physica B* **367** (2005) 142.

[108] S.-R. Sun, Y.H. Dong, *Phys. Rev. B* **72** (2005) 174101.

[109] T. Das, A. Deb, S. Mookerjee, *Physica B* **367** (2005) 6.

[110] F.El.H. Hassan, A. Hijazi, M. Zoaeter, F. Bahsoun, *Physica B* **363** (2005) 82.

[111] V.L. Moruzzi, J.F. Janak, A.R. Williams, *Calculated Electronic Properties of Metals*, Pergamon, New York, 1978.

[112] P.K. Lam, M.L. Kohen, *Phys. Rev. B* **24** (1981) 4224

[113] Y.M. Juan, E. Kaxiras, *Phys. Rev. B* **48** (1994) 14944.

[114] M. Sluiter, G. De Fontaine, X.Q. Guo, R. Podloucky, A.J. Freeman, *Phys. Rev. B* **42** (1990) 10460.

[115] P. Dufek, P. Blaha, K. Schwarz, *Phys. Rev. B* **50** (1994) 7279.

[116] A. Garcia, C. Elsasser, J. Zhu, S.G. Louie, M.L. Cohen, *Phys. Rev. B* **46** (1992) 9829.

[117] Y.M. Juan, E. Kaxiras, R.G. Gordon, *Phys. Rev. B* **51** (1995) 9521.

[118] J. Bok, *Comp. Phys. Commun.* **16** (1978) 113. *Phys. Rev. B* **63** (2001) 212101.

[119] B K Godwal, T C Kaushik and S K Sikka 1997 *Laser and Particle Beams* **15** 353

[120] J. F. Barnes, *Phys. Rev.* **153**, (1967) 269.

[121] Sidney Blairs and M. H. Abbasi, *J. Colloid Interface Sci.* **304** (2006) 549.

[122] A. A. Likalter, *Phys. Rev. B* **53** (1996) 4386.

[123] H. Hess and Z. Metallkd (1998) as given in the review paper V. Morel, A. Bultel and B. G. Cheron *Int. J. Thermophy.* **30** (2009) 1853.

[124] J. K. Singh, J. Adhikari and S. K. Kwak, *Fluid Phase Equilib.* **248** (2006) 1.

[125] D. G. Gordeev, L. F. Gudarenko, M. V. Zhernokletov, V. G. Kudelkin and M. A. Mochalov, *Combust. Expl. Shock Waves* **44** (2008) 177. *J. Appl. Phys.* **108** (2010) 053513.

[126] R. H. Willens and E. Buehler, Appl. Phys. Lett. **7** (1965) 25.

[127] P. Ronsheim, L. E. Toth, A. Mazza, E. Pfender and B. Mitrofanov, J. Mat. Sci. **16** (1981) 2665.

[128] J. Paul Day and Arthur L. Ruoff, *Appl. Phys. Lett.* **44** (1973) 2447.

[129] D. Gerlich and George C. Kennedy, *Appl. Phys. Lett.* **50** (1979) 3331.

[130] M. Lee, R. S. Gilmore, *J. Mat. Sci.* **17** (1982) 2657.

[131] Lars Fast, J. M. Wills, Börje Johnsson and O. Eriksson, *Phys. Rev. B* **51** (1995) 17431.

[132] Gerd Steinle-Neumann and Lars Stixrude, Ronald E. Cohen *Phys. Rev. B* **60** (1999) 791.

[133] W Voigt, Lehrbuchder Kristallphysik, Taubner, Leipzig, (1928).

[134] A. Reuss, Z. Angew. *Math. Mech.* **9** (1929) 55.

[135] S. F. Pugh, *Philos. Mag.* **45** (1954) 823.

[136] J. Schroers and W. L. Johnson, *Phys. Rev. Lett.* **93** (2004) 255506.

[137] S. S. Hecker, D. L. Rohr, and D. F. Stein, *Metall. Trans.* **A9**, 1978 481.

[138] D. C. Wallace, *Thermodynamics of Crystals* Wiley, New York, 1972.

[139] Orson L. Anderson, *Phys. Chem. Solids* **24** (1963) 909.

[140] H. J. Scussel, *Friction and Wear of Cemented Carbides* ASM Handbook, ASM Int. Metals Park OH **18** (1992) 795.

[141] V. G. Bukatov, Dissertation, Institute of Hard Alloys and Refractory Metals, Moskow (1979).

[142] Ziman J M 1967 *Electrons and phonons*, Oxford University Press, Oxford, p 364.